Particle Dispersion in Aluminium and Magnesium Alloys

A thesis submitted for the degree of

Doctor of Philosophy

by

Xinliang Yang

BCAST

Brunel University London

Uxbridge, UB8 3PH

United Kingdom

July 2016

Supervision: Professor Zhongyun Fan

Abstract

High shear mixing offers a promising solution for particle dispersion in a liquid with intensive turbulence and high shear rate, and has been widely used in the chemical, food and pharmaceutical industries. However, a practical high shear mixing process has not yet been adapted to solve the particle agglomeration in metallurgy due to the high service temperature and reactive environment of liquid metal.

In this study, the effect of high shear mixing using the newly designed rotor-stator high shear device have been investigated with both Al and Mg matrix composites reinforced with SiC particles through casting. The microstructural observation of high shear treated Al and Mg composites show improved particle distribution uniformity in the as-cast state. Increased mechanical properties and reduced volume fraction of porosity are also obtained in the composite samples processed with high shear.

With the melt conditioning procedure developed for twin roll casting process, two distinct solutions has been provided for thin gauge Mg strip casting with advanced microstructure and defect control. The melt conditioning treatment activates the MgO as heterogeneous nuclei of α-Mg through dispersion from continuous films to discrete particles. Thus enhanced heterogeneous nucleation in the twin roll casting process not only refines the α-Mg grain size but also eliminates the centre line segregation through equiaxed grain growth and localized solute distribution.

The grain refinement of the α-Mg through SiC addition has also been studied through EBSD and crystallographic approaches. Two reproducible and distinct crystallographic orientation relationships between α-SiC (6H) and α-Mg have been determined: $[10\bar{1}0]_{SiC}//[\bar{2}113]_{Mg}$, $(0006)_{SiC}//(10\bar{1}1)_{Mg}$, $(1\bar{2}1\bar{6})_{SiC}//(\bar{2}20\bar{2})_{Mg}$ and $[01\bar{1}0]_{SiC}//[1\bar{1}00]_{Mg}$, $(0006)_{SiC}//(0002)_{Mg}$, $(\bar{2}110)_{SiC}//(11\bar{2}0)_{Mg}$.

Acknowledgements

I would like to show my sincere thanks and great appreciation to my supervisor, Professor Zhongyun Fan for the opportunity to study as PhD student in BCAST, Brunel University London for four years. Without his support and guidance from the first day of the PhD journey to the completion of research, it is hard for me to achieve such progress in the project.

I wish to show my gratitude to Dr Ian Stone, Dr Shouxun Ji, Dr Yan Huang and Dr Hari Babu Nadendla for their supportive guidance in the research work and thesis preparation with inspiring discussion and constructive suggestions. Dr Chamini Mendis is greatly appreciated for the help in the final stage of thesis revising and correcting.

My colleagues Dr Hu-Tian Li, Dr Jayesh Patel, Dr Nilam Barekar, Dr Sanjeev Das, Dr Kawther Al-Helal, Dr Mingxu Xia, Dr Wenchao Yang, Dr Guosheng Peng, Mr Peter Lloyd and Mr Graham Mitchell are appreciated for their support during the experimental work and technical help. Dr Yun Wang and Dr Bo Jiang are appreciated for their help in the theoretical discussions. Dr Feng Wang is greatly appreciated for the constructive suggestions on the crystallographic study of the a-SiC and Mg orientation relationships and assistance with the electron microscopic techniques to conduct the research.

I would like to thank Dr Lorna Anguilano, Dr Ashley Howkins and Mrs Nita Verma for their kind support during electron microscopic analysis with helpful training and brilliant facility maintenance in the Experimental Techniques Centre (ETC), Brunel University London.

Finally, I offer my deepest gratitude to my parents and my wife who provided me with their unconditional love and support. Especially my wife, Ting Wang, who looked after our family through the whole period of my PhD study and brought us a lovely little Yuchen.

List of Publications

1. W. Yang, **X. Yang**, S. Ji. (2015) Melt superheating on the microstructure and mechanical properties of diecast Al-Mg-Si-Mn alloy. Metals and Materials International, 21:382-390.
2. S. Das, N.S. Barekar, Omer El Fakir, **X. Yang**, J.P. Dear, Z. Fan. (2015) Influence of intensive melt shearing on subsequent hot rolling and the mechanical properties of twin roll cast AZ31 strips. Materials Letters, 144:54-57.
3. **X. Yang**, S. Das, J.B. Patel, I.C. Stone, Z. Fan. (2015) Development of the MC-TRC process for continuous casting of thin gauge Mg alloy strip. Proceedings of the 10th International Conference on Magnesium Alloys and Their Applications. Korea, October 2015.
4. N.S. Barekar, S. Das, **X. Yang**, Y. Huang, Omer El Fakir, A.G. Bhagurkar, L. Zhou, Z. Fan. (2016) The impact of melt conditioning on microstructure, texture and ductility of twin roll cast aluminium alloy strips. Materials Science and Engineering, A650: 365-373.
5. **X. Yang**, Y. Huang, N.S. Barekar, S. Das, I.C. Stone, Z. Fan. (2016) High shear dispersion technology prior to twin roll casting for high performance magnesium/SiC_p metal matrix composite strip fabrication. Composites Part A: Applied Science and Manufacturing, 90: 349-358.
6. **X. Yang**, F. Wang, Z. Fan. Crystallographic study of nucleation in SiC particle reinforced magnesium composite. To be submitted, 2016.

List of Abbreviations

Al-MMC	Aluminium and aluminium alloy based metal matrix composite
BSD	Backscatter diffraction
CD	Casting direction
CSIRO	Commonwealth Scientific and Industrial Research Organisation (Australia)
DC	Direct current
DC casting	Direct chill casting
EBSD	Electron backscattered diffraction
EDS	Energy dispersive X-ray spectroscopy
FFT	Fast Fourier transform
HPDC	High pressure die casting
HS	High shear
IS	Impeller stirring
HRTEM	High resolution transmission electron microscopy
MC	Melt conditioning
MC-TRC	Melt conditioned twin roll casting
Mg-MMC	Magnesium and magnesium alloy based metal matrix composite
MMC	Metal matrix composite
OM	Optical microscopy
OR	Orientation relationship
PIPS	Precision ion polishing system
PM	Powder metallurgy
POSCO	Pohang Iron and Steel Company
PR-MMC	Particle reinforced metal matrix composite
R&D	Research and design
SAD	Select area diffraction
SEM	Scanning electron microscopy
SiC_p	Silicon carbide particles
TEM	Transmission electron microscopy

TD	Transverse direction
TRC	Twin roll casting
XRD	X-ray diffraction

Table of Contents

Chapter 1 Introduction

1.1. Background

Particle reinforced light metal (aluminium and magnesium) matrix composites show a promising combination of cost efficiency, tailorable materials with mechanical property improvement and weight reduction (Miracle 2005). The major particle reinforcements are in the form of ceramic particles (Lloyd 1994). The fabrication methods of particle reinforced light metal matrix composites are extensively studied and commercially available for specific applications (Chawla, Chawla 2006). Particle reinforced light metals and alloys, with their potentials of low fabrication cost, high modulus, high wear resistance, tailored coefficient of thermal expansion and high strength, can be customised for specific servicing condition with affordable manufacturing cost and facility requirement (Surappa 2003).

On the other hand, grain refinement through the trace addition of inoculant has been utilised in Al industry for more than half a century (Easton, StJohn 1999, McCartney 1989) and are extend into the Mg driven by the potential for reduction of green-house gas emission (Agnew 2004, Agnew, Nie 2010). The classic Al solidification theories (Quested, Greer 2004, Greer et al. 2000) suggested that given an inoculant, the nucleation potency of the inoculant is greatly related to the particle size distribution as well as particle number density in the melt. Larger particle size and higher number density provides more potency to activate enhanced heterogeneous nucleation for a refined microstructure.

This highlights the importance of ceramic particle dispersion in liquid metal. In addition to the difference in various industrial applications, the behaviour of rigid particles in liquid medium is an important research area requiring extensive attention (Tomas 2007). The agglomeration of particles in the liquid is one of the major topics. Particle adhesion is caused by surface and field forces (van der Waals, electrostatic and magnetic forces), material bridges between particles surfaces (liquid and solid bridges, flocculants) and mechanical locking (Tomas 2007). Comparing to other scenarios such as particles in molten metal, formation of clusters and agglomerates from rigid ceramic particles in the liquid metal melt is mainly caused by Van der Waals force and/or liquid bridge depending

on the wetting of the particle surface by the liquid melt (Lloyd 1994). The dispersion of particles (mixing of solids into liquid medium) is to break agglomerates to discrete particles and then distribute them throughout the liquid. The entire process of incorporation of solid particles into a liquid involves several stages (wetting, impregnation, rupture and erosion) which may occur with some degree of overlap (Atiemo-Obeng et al. 2004). With an understanding of cohesive bonding of particles in agglomerate, it is clear (Hansen et al. 1998) that sufficient forces are needed to overcome the cohesive forces and to break up the agglomerate into discrete particles in order to achieve a good dispersion of particles in the liquid. Extensive research and design has been conducted development of facilities with capability of mixing and dispersing particles with varying solid-liquid system (Edwards, Baker 1992). As a result, a wide range of mixing facilities are available commercially in the chemical engineering, food and pharmaceutical industries.

Since the dispersion of particles in liquid metal is important for applications like processing of metal matrix composite and grain refinement, an investigation of melt conditioning technology (high shear treatment) (Fan et al. 2011) on these applications is necessary to provide a practical solution for ceramic particle dispersion and understanding of the operating mechanism.

1.2. Research Objectives

The major objectives of this study are:

- To investigate the effect of high shear treatment on the reinforcing particle dispersion during processing of Al and Mg matrix composites on microstructure control and resulting mechanical properties.
- To understand the operating mechanisms responsible for dispersing the reinforcing particles with high shear treatment.
- To modify the melt feeding system of twin roll casting process for Mg alloys and Mg matrix composites.
- To develop the melt conditioning process for twin roll casting of thin gauge Mg alloy strip.
- To investigate the Mg alloy strip produced by melt conditioned twin roll casting process in terms of microstructure evolution and defect control.

1.3. Outline of Thesis

After the introduction of the research background, previous literature is reviewed in Chapter 2 with a detailed overview of study on the particle adhesion and dispersion in liquid, applications of particle dispersion in metallurgy such as reinforcement distribution in metal matrix composites and inoculant dispersion for grain refinement as well as the technology for particle dispersion. The technique of twin roll casting is also reviewed as it is the major casting method used in this study. Chapter 3 describes the experimental procedures and characterization techniques conducted in the study. In Chapter 4, the results and discussion of A356/SiC_p composites with and without high shear treatment are presented with microstructure observation, defects evaluation, and mechanical property measurement of composites with different treatment parameters, reinforcement additions and cooling rates during solidification. In Chapter 5, the results and discussion of AZ31/5SiC_p composites with and without high shear treatment are provided in the form of twin roll casting strip. The grain refinement of AZ31 alloy by SiC particle addition is discussed with varying SiC additions from 0.1wt% to 5.0wt% and crystallographic analysis is also employed to reveal the orientation relationship between SiC and α-Mg matrix. Chapter 6 shows the modification of melt feeding system and development of melt conditioning process for twin roll casting of thin gauge Mg alloy strip. The microstructure and defect observations are presented to investigate the effect of melt conditioning on the Mg alloy strip. The conclusions and suggestions for future work are listed in Chapter 7 and Chapter 8, respectively.

Chapter 2 Literature Review

2.1. Rigid Particle Behaviour in Liquid

2.1.1. Adhesion

The mixing of fine (d<100 μm), ultrafine (d<10 μm) and nano-sized (d<0.1 μm) particles in the liquid medium with varying physical and chemical properties (Tomas 2007) is a continued topic of research in the chemical engineering, and food processing industries. With the development of particle reinforced metal matrix composites (Lloyd 1994) and the fundamental understanding of grain refinement (McCartney 1989), the behaviour of rigid particle in liquid melt became an important research direction with extensive attention in metallurgy (Hashim et al. 2002b). The difference in varying industrial applications aside, the cohesion and adhesion of particles are the two major behaviours in the liquid medium without external interference. Particle adhesion is caused by surface and field forces (van der Waals, electrostatic and magnetic forces), material bridges between particles surfaces (liquid and solid bridges, flocculants) and mechanical locking (**Fig. 2.1**) (Tomas 2007).

For the surface and field forces, van der Waals forces are expected in all dry powders consisting of polar, induced polar and non-polar particles such as minerals, chemicals, plastics, pharmaceuticals and food (Israelachvili, Tabor 1973). In some applications, electrostatic forces may be found in the particle addition of electric conductor and non-conductor (Rumpf 1974). Additionally, the magnetic forces become critical when iron powder is used.

Bridges between particle surfaces form due to the following sources: (a) liquid bridges due to low viscous wetting liquid through capillary pressure and surface tension (moisture on the particles) and/or high viscous bond agents (resins) (Schubert 1979). (b) solid bridges by re-crystallization of liquid bridges which contain solvents, solidification of swelled ultrafine gel particles, freezing reactions with adsorbed surface layers or cement with interstitial pore water, solidification of highly viscous bond agents, contact fusion by sintering and chemical bonds due to solidi-solid reactions (Tomas, Schubert 1982).

Mechanical locking is influenced by the macromolecular and particle shape effects, including chains branches of macromolecules, contacts due to overlapping of surface asperities and hook-like bonds (Rumpf 2012).

In comparison to other scenarios during the metallurgical processing, formation of clusters and agglomerates from rigid ceramic particles in the liquid metal melt is mainly caused by the Van der Waals force and/or liquid bridges depend on the wetting of particle surfaces by the liquid melt (Lloyd 1994).

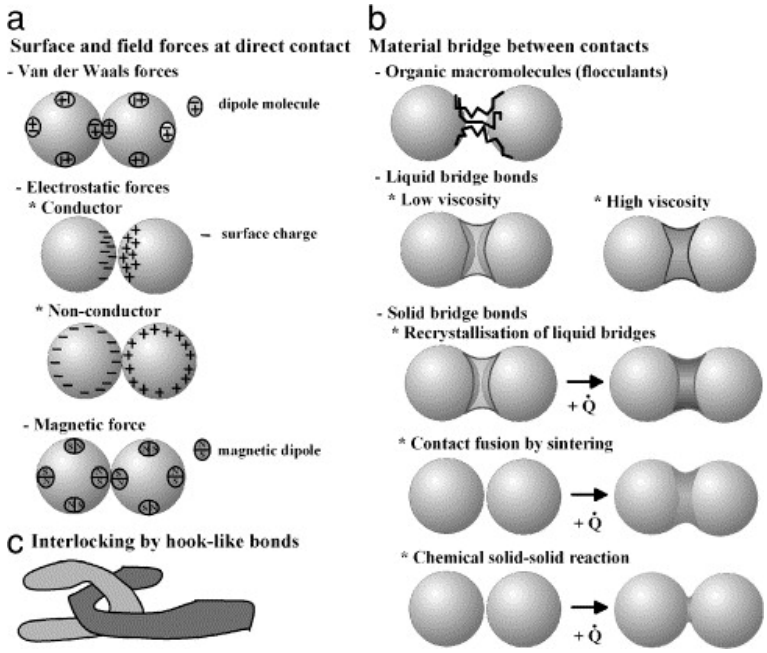

Figure 2.1 Particle adhesion and microprocesses of particle bond effects in contact (Tomas 2007).

2.1.2. Dispersion

Dispersion of solid powder particles in liquid is important for many practical applications. The nature and the quality of dispersion greatly influence the physical, chemical and mechanical properties of the resulting products. The object of a dispersion (mixing of solids into liquid) is to break agglomerates to discrete particles and then distribute them throughout the liquid (Tomas 2007). The entire process of dispersion of a powder into a liquid involves several stages (wetting, impregnation, rupture and erosion) which may occur with some degree of overlap (Hansen et al. 1998).

The fragmentation theory (Cheng, Redner 1990, Redner 1990) is used commonly to refer a broader class of processes involving breakup of solid clusters/agglomerates. There are

two main processes considered in the theory; rupture and erosion (Hansen et al. 1998). Rupture is the breakup of a cluster into several fragments of comparable size, and erosion is the gradual shearing off of small fragments from larger clusters (Cheng, Redner 1990). Breakup due to hydrodynamic forces may be characterized by the Fragmentation number (*Fa*) which is the ratio between the viscous shear stress and the strength of the agglomerate (Rwei et al. 1990),

$$Fa = \frac{\mu\dot{\gamma}}{T} \tag{2.1}$$

where $\dot{\gamma}$ is the magnitude of the rate-of-deformation tensor which equals to $\sqrt{2D:D}$, D equals to $[\nabla_V + (\nabla_V)^T]/2$, where V is the velocity of the flow. The term T denotes the characteristic adhesive strength of the agglomerate and plays a role analogous to the surface tension in the definition of the Capillary number of liquid drops (Stone 1994).

The adhesive strength of agglomerate is a combination of the strength of inter-particle bonds due to van der Waals forces, moisture or electrostatic charges (Israelachvili, Tabor 1973, Rumpf 1974). Several models have been developed to describe the adhesive strength and the simplest model describes two neighbouring particles. Rumpf's model considers the agglomerate as a collection of spherical particles with a radius *a*, occupying a volume fraction φ, bonded to each other via cohesive forces. According to this model (Rumpf 1962), the tensile strength of agglomerate is given as,

$$T = \frac{9}{32}\frac{\varphi}{\pi a^2} n_b F \tag{2.2}$$

where F is the average binding force of a single bond and n_b is the average number of bonds per particle.

Kendall proposed a model assuming that the breakage occurs at a strength limiting flaw, and the expression of the strength of the agglomerate (Kendall 1988) is given as,

$$T = 11.03\frac{\varphi^4 \Gamma_c^{5/6} \Gamma^{1/6}}{\sqrt{l_f a}} \tag{2.3}$$

where Γ_c and Γ are the fracture surface energy and the equilibrium surface energy, respectively, and l_f is the flaw size. The model provided by Rumpf didn't consider the influence of fractal structures in the agglomerate as compared with Kendall's work. Rumpf's model provided several conditions required to be fulfilled for the scenarios in metallurgy including: (a) there are a large number of bonds in the material to be broken, (b) the bonds and particles are randomly distributed throughout the agglomerate, and (c) the mean cohesive force for a bond is homogeneous throughout the agglomerate and particle-liquid system.

The understanding of the adhesive bonding of particles in agglomerate makes it clear that sufficient forces are required to overcome the cohesive forces and break up the agglomerate into discrete particles to achieve a good dispersion of particles in the liquid. The external forces required for a good dispersion in the solid-liquid system is provided by the mechanical energy input into the fluid-solid system. The energy input creates a turbulent flow field in which solid particles are introduced from top/bottom of the vessel and subsequently dispersed and distributed in the liquid. The dispersion of solid particles is achieved by a combination of the drag and lift forces of the moving fluid on the solid particles and the bursts of turbulent flow originating from the bulk flow in the vessel (Atiemo-Obeng et al. 2004).

Extensive research and design was required for the facility development with capability for mixing and dispersing particles with varying solid-liquid system (Zhang et al. 2012). As a result, a wide range of mixing equipment is commercially available in chemical engineering, food and pharmaceutical industries.

The facilities are catalogued according to their distinct design: mechanically agitated vessels, jet mixers, in-line static mixers, in-line dynamic mixers, dispersion mills, valve homogenizers, ultrasonic homogenizers and extruders (Edwards, Baker 1992).

With enormous mixing capacities required in industrial application, the facilities have large variety of mixing equipment and there is no single type mixing machinery can cover over a certain range of capacity efficiently.

2.2.Reinforcing Particle Dispersion in Metal Matrix Composites

2.2.1. Metal Matrix Composites

The metal matrix composites (MMCs), a materials with tailorable advanced properties, is one of the major innovations in materials born in the “Space Race” between the two super-powers as further extension of conventional metals and alloys since the launch of Soviet satellite Sputnik in 1957 (Rawal 2001).

The flexible combination of reinforcements, matrix materials and fabrication methods led to a family of construction/functional composite materials with different physical, chemical and mechanical properties for engineering applications with varying degrees of technical requirements. Although, intensive research is focused on this topic, MMC materials are still in the early stages of development as the limited fundamental scientific understanding and technology is immature for commercial applications (Miracle 2005).

MMC reinforcements are generally catalogued into three major types: continuous fibres, short fibres/whiskers and particles (**Fig. 2.2**). The reinforcement of continuous fibres, for MMCs lighter than monolithic metals and stronger than polymer composites (Chou et al. 1985), includes boron, carbon, alumina ad silicon carbide, and metallic fibres and wires (W, Be, Ti, Mo and Nb) used in super alloy or copper composites (Caulfield, Tien 1989, Tang et al. 2008).

These reinforcements contributed to the improvement of stiffness, strength, ductility, and thermal/electrical conductivities along the fibre direction of MMCs. However, the high cost of synthesis fibre, complexity of MMCs fabrication, property anisotropy and low productivity hinder it from being used widely in the transportation industry (Hooker, Doorbar 2000).

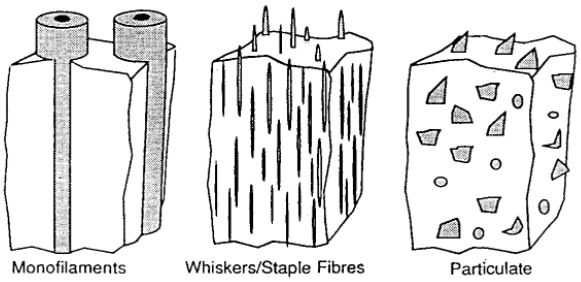

Figure 2.2 The schematic illustration of various types of MMCs reinforcements (Clyne, Withers 1995).

The leading short fibres/whiskers reinforcements are alumina, alumina-silica, silicon carbide and carbon nano tubes (Nardone, Prewo 1986, Bakshi et al. 2010). The short fibre/whisker reinforced MMCs provide properties in between of continuous fibres and particles but with reduced synthesis cost compared with continuous fibre reinforcement (Nair et al. 1985, Wang, Rack 1991).

The particle reinforcement has a wide range choice of ceramic particles including mica, alumina, silicon carbide, zircon, boron carbide and titanium dioxide, and recently graphene, graphite also become popular (Kok 2005, Logsdon, Liaw 1986, Wang et al. 2012).
The particle reinforced MMCs provides a more isotropic properties compared with continuous fibres reinforced MMCs as the reinforcing particles are distributed with a random orientation distribution during the fabrication (Lloyd 1994, Ibrahim et al. 1991).

The most investigated metal matrix systems are aluminium, magnesium, titanium, copper and super alloy systems (Clyne, Withers 1995). Aluminium and magnesium matrix composites forge the major portion of these matrix systems as the varying property requirements of these light metals are more extensive and urgent due to the carbon emission regulations (Dieringa 2011). The titanium and super alloy matrix systems are mainly designed for aerospace, aviation and energy industry applications where weight reduction and high service temperatures are required (Hooker, Doorbar 2000). The copper matrix composites combined with reinforcements provide high electrical and/or thermal conductivities further increase the physical and chemical properties of Cu-MMC materials (Ayers, Fletcher 1998).

In the automobile industry, the cost and productivity are the main concerns for materials selection compared with other industries (Orsato, Wells 2007). Light metal (aluminium and magnesium) matrix composites reinforced with ceramic particles show a promising combination of economy efficiency, easily accessible materials with mechanical property improvement and weight reduction (Goni et al. 2000, Cole, Sherman 1995). The major particle reinforcements are ceramics and the fabrication methods of particle reinforced light metal matrix composites are extensively studied and commercially available in certain applications (Ibrahim et al. 1991).

Particle reinforced light metals and alloys, with potential low fabrication costs, high modulus, high wear resistance, tailored coefficient of thermal expansion and high strength, can be customised for specific service conditions with affordable manufacturing cost and facility requirement.

2.2.2. Fabrication Methods

Powder metallurgy (PM) method

Powder metallurgy was the first method to be developed in the early stage of MMCs research since wetting ceramic particles with molten metal was difficult (Lloyd 1994). The essential features of powder metallurgy processing route are shown in **Figure 2.3**.

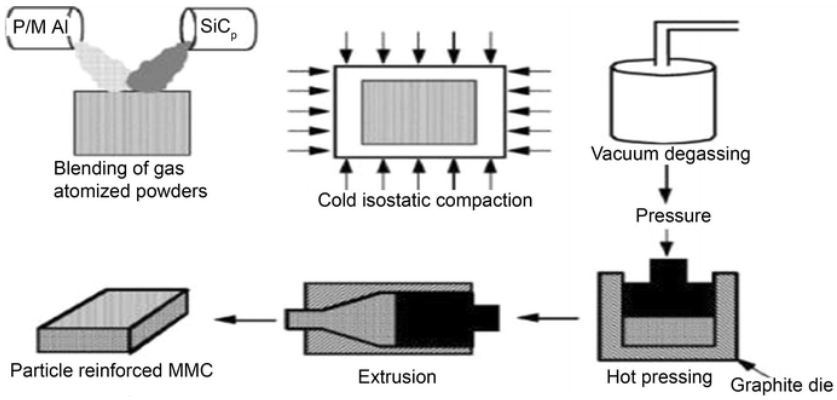

Figure 2.3 The schematic illustration of powder metallurgy processing route for particle reinforced MMC (Borgonovo, Apelian 2011).

During the blending of the reinforcing particles and matrix powder, several techniques were employed to achieve uniform distributions of reinforcing particles. Mechanical alloying by ball milling and tumble mixing are the two of the major methods used to achieve initial homogeneity (Kuhn 2012).

The blended powder mixture is then transferred into a mould for cold isostatic compaction, followed by a vacuum degassing process to remove the moisture associated with the hydrated oxide films on the powder particles. Then hot pressed to further consolidation of the composite block (over 95% dense) and sintered similarly to cold isostatic compaction (Rahimian et al. 2009). The processing temperature is below the solidus of the matrix material, or in the semi-solid state in order to avoiding the disadvantage of interaction between reinforcing particle and matrix in the liquid region. Coarse eutectic and intermetallics can also be avoided by limiting the sintering temperature below the

liquidus of the matrix material. As the alloy powders are generally produced via rapid solidification, this solid/semi-solid state consolidation helps to retain the supersaturated metastable composition of matrix.

The extrusion is used to obtain the final wrought product of MMCs after hot pressing. A high extrusion ratio (>20:1) (Das et al. 2002) was required to disrupt the oxide films between the matrix alloy powders for better metal-metal bonding and to improve the distribution of reinforcing particles by dispersing existing clusters of reinforcement with the plastic flow associated with extrusion.

The advantage of PM method as a processing route is that there is almost no limitation on choice of matrix and reinforcement particles even non-equilibrium alloy powders obtained by rapid solidification. The interactions between matrix and reinforcement and the microstructure coarsening of the matrix can be minimised due to the solid state processing. The high volume fraction (> 40vol. %) and fine particle size (micron and sub-micron) of reinforcements are accessible to maximise the modulus and minimise the coefficient of thermal expansion of the composite through PM method (Lloyd 1994).

On the other hand, highly reactive powders, complex processing routes and limited forms of the starting product hinder this fabrication method from being widely applied to MMCs production (Torralba et al. 2003).

Liquid metal processing

(a) Mixing method:

The mixing method introduces ceramic particles through a vortex created in the melt by rotation of an impeller. The molten metal mixing method is attractive as it allows the conventional metal processing routes to be used with minimised cost (Hashim et al. 1999).

However, some problems in terms of reactivity between the reinforcement and the alloy melt, and particle segregation limits the final properties of particle reinforced metal matrix composites (PR-MMCs) (Shorowordi et al. 2003). The volume fraction of reinforcement is also limited because of the viscosity increase associated with the increased addition of reinforcing particles (Flemings 1991).

(b) Semi-solid casting:

The PR-MMCs fabricated by stirring a semi-solid melt was investigated in the early 1970s (Mehrabian et al. 1974). The partially solidified, non-dendritic microstructure developed has high viscosity which inhibits ceramic particles settling and floating, and can be used to retain particles in the melt (Zhou, Xu 1997). The process is restricted to alloys with a longer freezing range alloys and, other than this, has the same limitations as the mixing methods starting in the liquid phase.

(c) Infiltration:

The infiltration method incorporates a pre-formed porous reinforcement framework and the molten melt fulfils the empty space of the reinforcement framework with and without pressure (Mortensen et al. 1990). After that the master composite can be diluted by liquid metal to further fabricating MMC with low reinforcement volume fraction if necessary. With the additional dilution stage, the same factors come into play as with the direct mixing route like reactivity, particle segregation and high viscosity (Lloyd 1994).

(d) Spray deposition:

The spay deposition involves atomising a melt and collecting the semi-solid droplets on a substrate in the nature of hybrid rapid solidification process (Mathur et al. 1989). This process has the advantage that the contact time between the melt and reinforcement is limited and leads to a suppressed interfacial reaction. Thus a wider range of reinforcements are possible to be used with MMC fabrication. A secondary thermal mechanical process is required to consolidate the billet as the initial billets are typically 95-98% dense (Gupta et al. 1993, White, Willis 1989).

2.2.3. Factors Influencing Reinforcement Dispersion in Liquid Metal

The critical challenge to overcome is the severe agglomeration of the reinforcing particles which deteriorate the composite properties during fabrication of PR-MMCs (Hashim et al. 2002a, Lloyd 1994). In powder metallurgy, ball milling and tumble blending (Lenel 1980) are normally used to mix the reinforcing particles with the matrix powder. In the casting route, mechanical stirring (Hashim et al. 1999) has been a routine method used to mix the reinforcing particles in the molten alloys. The problem with conventional mechanical stirring is that the shear rate applied is inadequate to break up particle agglomerations (Rumpf 1962), particularly when there is a high volume fraction of ultra-

fine (< 10 µm) particles (Barekar et al. 2009). The turbulence generated in the melt surface during mixing by conventional mechanical stirring is a main cause for the gas entrapment (Hashim et al. 2002b) in the melt.

The importance of reinforcing particle distribution and dispersion in the final performance of PR-MMC, resulted in extensive research on understanding the relationship between particle distributions and influencing factors.

Wetting

The oxide films on the melt surface or contaminants on the ceramic particles lead to non-wetting of ceramic particles and the molten liquid (Oh et al. 1989). Elements with greater affinity for oxygen than the melt can concentrate preferentially at the melt/ceramic interface, reducing the surface energy and thereby improving wettability of the ceramic particles in the liquid metal. Mg is known to decrease the surface tension of the melt due to its low surface tension (0.599 N/m) (Sukumaran et al. 1995). With 3 wt% Mg in the Al melt, the surface tension of melt reduced from 0.760 N/m to 0.620 N/m (Rohatgi et al. 1986a). The improved wettability of the ceramic particles helped the liquid metal penetrate into the gaps between neighbouring particles and reduce the tendency of agglomeration.

Interfacial reaction

The topic of interfacial reaction between reinforcement and matrix has been discussed over a long time in the MMC literature. The reactivity of reinforcing particles and matrix can significantly increase the interfacial bonding strength and modify the deformation and fracture mode of the composite (Mortensen 1991). However, interfacial reaction can also result in changes to the composition of alloy matrix through the introduction of new intermetallic phase which influence the basic properties such as the melting point and strength of the matrix (Lloyd, Jin 1988). In silicon free alloys, SiC is thermodynamically unstable above the meting point, reacting to form aluminium carbide (Lloyd 1994),

$$4Al + 3SiC \leftrightarrow Al_4C_3 + 3Si \qquad (2.4)$$

As the reaction 2.4 proceeds in the composite melt, the silicon content increases in the matrix and the melting point of the composite decrease due to the composition change (**Fig 2.4**). The formation of Al_4C_3 can be increased or suppressed by the variation in

silicon level due to the chemical balance of reaction (**Fig 2.5**). Other carbides such as boron carbide and titanium carbide are also thermodynamically unstable in molten aluminium, but often react in a more complex manner.

Mg is chemically inert to carbon, so ceramic carbides are stable in pure Mg melt (StJohn et al. 2013). However, many of the Mg alloys contain alloying elements that may form carbides when the level of elements is relatively high and contact times are sufficiently long.

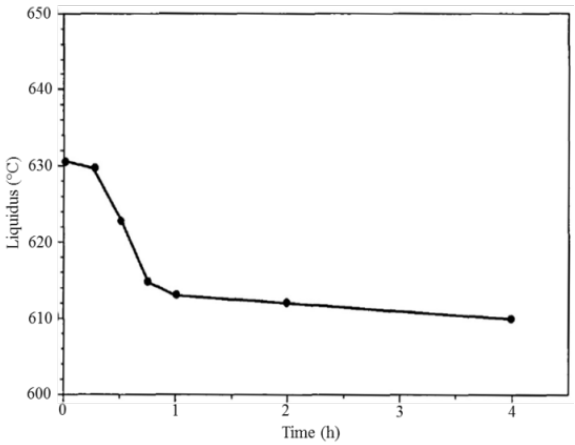

Figure 2.4 Decrease of melting point with time at 675°C for 7075/15vol%SiC_p composite (Lloyd, Dewing 1988).

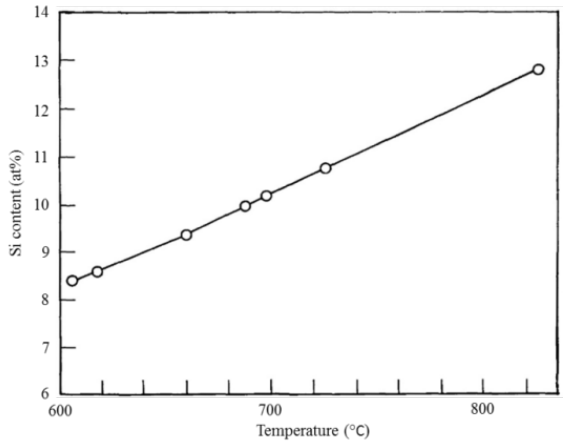

Figure 2.5 Silicon level required in the Al alloys at different temperature to prevent aluminium carbide reaction (Lloyd 1989).

Solidification behaviour

The reinforcing particle distribution in the composites by liquid metal method is influenced during the three stages of whole procedure from incorporating reinforcing particles in the liquid metal to integrated composites ingot (Lloyd 1994).

First stage is in the liquid state, the distribution of reinforcing particles depends on the effect of mixing process. It is important to produce as uniform distribution as possible with the de-agglomerated reinforcing particles and remove gas entrapped in the composite slurry. The impeller stirring above and below melt liquidus, ultrasound mixing (Babu et al. 2013) and high shear treatment (Tzamtzis et al. 2009) are the main mixing procedures employed for MMC application.

During the second stage, after mixing but before solidification of composite slurry, the distribution of reinforcement is influenced by the settling of particles due to gravity. The settling rate of reinforcement is a function of the particle density, size and concentration (Atiemo-Obeng et al. 2004, Hashim et al. 2002b). Higher the concentration of reinforcement and shorter the holding time of the slurry before casting will give rise to slower rates of settling. Particle settling has a lower effect on the distribution of reinforcements.

The last stage is solidification. The distribution of reinforcing particles will change as a result of the development of solidification microstructure. The majority of reinforcing particles face the rejection at the solid/liquid interface during the solidification and only limited amount of particles will remain inside the primary phase as potent sites for the heterogeneous nucleation (Lloyd 1989).

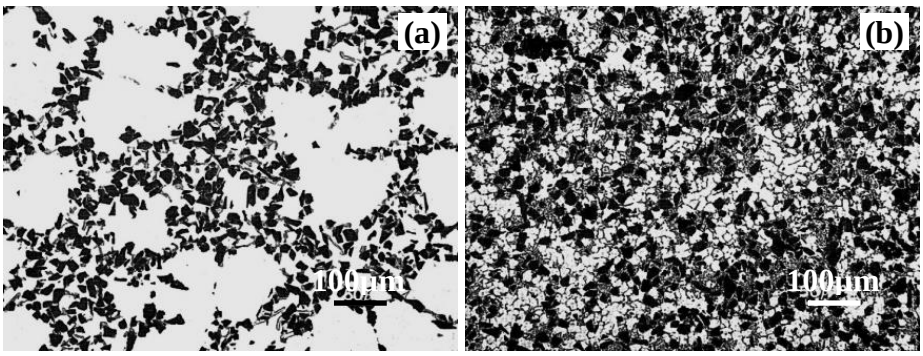

Figure 2.6 The influence of solidification conditions on the reinforcing particle distribution, (a) investment casting with a slow cooling rate, and (b) high pressure die casting with a high cooling rate (Lloyd 1994).

Particle entrapment or rejection is extensively studied since beginning of MMCs research. The entrapment models are generally applicable to planar front solidification of single phase systems (Juretzko et al. 1998), while dendritic solidification of multiphase systems is of more interest. In commercial systems, the reinforcement distribution is influenced

by the solidification rate as the network of inter-dendritic area will host the reinforcing particles and determine the final distribution of particles (Lloyd 1989). The difference in reinforcement distribution is shown in **Figure 2.6** for A356/15vol%SiC_p composite with different cooling rates. A finer inter-dendritic network results in an improved reinforcement distribution.

2.3.Grain Refiners in Light Alloys

The grain refinement of light metals with inoculant is utilised in the Al industry with TiB_2 particles in the form of Al-5Ti-1B and Al-3Ti-1B master alloys (McCartney 1989) and Mg industry with Zr clusters for aluminium free alloys (StJohn et al. 2013).

In the last two decades, the mechanism of grain refinement by inoculant particles has been investigated systematically. Greer first introduced the free growth model (Greer et al. 2000) presenting that with the same inoculant in the melt, the larger particles have more potency to be activated as heterogeneous nucleation sites, then Ming-Xin Zhang presented an edge-to-edge matching (E2EM) model (Zhang, Kelly 2005) illustrating the crystallographic orientation relationship between the inoculant and the matrix alloy that nucleate and grow on the inoculant. From the model, certain crystal directions and planes of substrate and matrix could be matched to have small misfit.

Based on the continued extensive research on the grain refiner for Al production, Fan proposed an epitaxial model (Fan 2013), which shows the potency of inoculant as heterogeneous nucleation sites increases with the interlayer or interlayers to adjust the lattice misfit to an acceptable value to initiate the nucleation. Experimental evidence presented supports this theory (Fan et al. 2015), and then the single atomic layer of Al-Ti interlayer was found between TiB_2 and α-Al crystal lattice arrangement.

The previous research (Maxwell, Hellawell 1975, Quested, Greer 2004), show that the efficiency of grain refining by inoculant particles is related to the dispersion of the inoculant. When nucleation activated on one inoculant, the heat released would interrupt the undercooling required for the nucleation of neighbouring inoculants in the surrounding area and they become ineffective.

2.3.1. Particle Dispersion of Grain Refiner for Al Alloy

In the past century, grain refinement by inoculation has delivered significant benefit to the aluminium industry with improved mechanical and metallurgical properties as well as reduced cast defects, such as porosity, ingot cracking, hot tearing and chemical segregation (McCartney 1989). As a typical and classic system, Al-Ti-B master alloy containing TiB_2 effective inoculant (Easton, StJohn 1999) is the most widely used grain refiner for Al wrought alloys which consist of a large portion of the final product market.

However, the manufacture of Al-Ti-B master alloy involves a chemical reaction between potassium hexafluorotitanate (K_2TiF_6) and potassium tetrafluoroborite (KBF_4) to form *in-situ* TiB_2 particles, and consumption of large amount of K_2TiF_6 and KBF_4 and the expensive treatment of harmful fluoride emission during reaction have given rise to concerns that the fabrication method is expensive and environmental unfriendly (Birol 2007). Extensive research focus on the development of a new grain refiner and modification of the existing Al-Ti-B grain refiner through chemical addition and external force dispersion.

Many master alloy systems are capable of refining the microstructure of Al alloys, e.g. Al-Ti-C, Al-Sc, Al-Zr, Al-Cr etc. (McCartney 1989). The Al-Ti-C system is the most commonly used grain refiner other than the Al-Ti-B master alloy, which contains TiC and Al_3Ti particles as the titanium level is typically present in excess of stoichiometric ratio of TiC (Banerji, Reif 1986). Several studies (Mohanty, Gruzleski 1994, Zhang et al. 2005) reported that TiC inoculants are responsible for the refinement due to the simple cube-cube orientation relationship with α-Al matrix. The advantages of TiC particles comparing to TiB_2 are lower agglomeration tendency and is not susceptible to Zr and Cr poisoning, but performance of TiC is affected by the Si and Mn level due to the chemical stability in such circumstance (Schneider et al. 1998). The thermodynamic stability of TiC is limited in most Al melts and converts into Al_4C_3 during long holding time (Tronche et al. 2002). Therefore, the parameters for Al-Ti-C master alloy addition and casting need to be strictly controlled. For those master alloys with binary element system, the intermetallic phases (Wang et al. 2013, Norman et al. 1998) with similar cubic structure normally act as the nucleation substrate for α-Al matrix, e.g. Al_3Sc, Al_3Zr and etc.

The purpose of dispersion of TiB_2 inoculant through the use of external forces is to modify the particle size distribution into a narrow range and achieve a uniform spatial distribution in the master alloy (Quested, Greer 2004). This increases the potency and efficiency of inoculant particles in the Al melt, reduces the amount of master alloy addition for similar grain refinement, and eliminates the existence of redundant inoculants in primary ingot which affect the thermal mechanical processing of the thin sheet and foil products (Murty et al. 2013). Ultrasound treatment was reported to increase the efficiency of Al-Ti-B master alloy by an improved TiB_2 particle distribution (Han et al. 2005). High shear technology (Fan et al. 2011), a newly developed melt conditioning method, is also capable of enhancing the inoculant dispersion by intensive shearing of melt with high turbulence and high shear rate.

2.3.2. Particle Dispersion of Grain Refiner for Mg Alloy

The developments of grain refining technologies for Al alloy and Mg alloy are initially started from 1930's, when the earliest reports published (Farbenindustrie 1931). In early 1950s, the Al-5Ti-B master alloy was developed for most Al alloys (Easton, StJohn 1999, McCartney 1989). However, for Mg alloys there is no equivalent solution that provides a reliable, repeatable as-cast grain size in a cost effective way. Zr grain refinement by the addition of Mg-Zr master alloy is recognized as one of the attractive grain refiners for Al-free Mg alloys (StJohn et al. 2005). Its performance is related to the Zr particle number density and particle size (the larger particles settle out during alloying).

Although the Mg-Zr master alloy is successfully commercialized for Mg-Zn and Mg-RE alloys, there is a need to develop a commercially viable grain refiner for Mg-Al alloy, which is the basis of Mg alloy casting, as the affinity of Al for Zr leads to the formation of Al_3Zr and reduces the efficiency of Zr for grain refinement (StJohn et al. 2005).

There are extensive investigations on grain refining technology for Mg-Al alloy by both research institutes and companies. Prior to the end of World War II, superheating was used for the grain refinement of Mg-Al alloys (StJohn et al. 2013). Basis of this method, the idea relies on grain refinement through Fe existence. There is debate on the Fe as a grain refiner of Mg-Al due to the results obtained with the inadequate experimental control and analysis lacks accuracy. On the other hand, several experimental results suggested that for high purity Mg-Al alloy has finer grain size <0.001% Fe when

compared with an alloy with 0.02% Fe (Nelson 1948). Further with the presence of Al, C and O containing particles within the central region of Mg grains, the grain refinement of Mg-Al through impurity control is attributed to the presence of Al_4C_3 or Al-C-O particles (Tamura et al. 2000, Tamura et al. 2002).

The carbon based grain refining process was discovered in the campaign to find an alternative process to superheating, as it requires high operating temperatures and only applicable for a small melt. Generally any materials containing carbon can be used as inoculating additives, and achieve a grain refining with appropriate level of addition. These additives are of two main types (StJohn et al. 2013): (a) Carbonaceous gases: carbon monoxide, carbon dioxide, acetylene, methane and natural gas; (b) Solid carbon additives: carbon powder, lampblack, magnesite, calcium carbide, calcium cyanimide, paraffin wax and silicon carbide.

Since the 2000's, the interest in external fields which may assist the nucleation of grains has increased. Melt conditioning, ultrasound treatment and electromagnetic stirring have shown to be efficient in grain refining of light metals (Babu et al. 2013, Liu et al. 2008). Fan et al. presented a melt conditioning method to break-up the oxide skins of Mg alloy and disperse it into individual MgO particles as well as dispersing Al_8Mn_5 intermetallics in AZ series alloys (Fan et al. 2009). The experimental research on melt conditioned Mg-Al alloy contained a refined microstructure compared with non-treated sample in mould casting, direct chill casting and twin roll casting (Jiang 2013, Bayandorian et al. 2012). This suggests that the dispersed MgO could result in the refinement of α-Mg grain in AZ91 alloy. The crystallographic studies of the interface between MgO and matrix α-Mg suggests that a good orientation relationship $\langle 01\bar{1}\rangle_{\mathrm{MgO}}$ and $\langle 1\bar{2}10\rangle_{\mathrm{Mg}}$ can be found with limited crystal lattice misfit of 5.46% (Fan et al. 2009) and led to the confirmation of MgO as a nucleation substrate for Mg based on the experimental undercooling analysis and free growth model calculation (Men et al. 2010).

The discovery that MgO particles as a potent nuclei of α-Mg matrix provides a significant progress in finding a grain refiner of Mg-Al alloy from adding inoculant in the melt to the activating the *in-situ* particles for grain refinement. This requires external field with high energy intensity to dispersing MgO from continuous skin to significantly increase number density of particles for heterogeneous nucleation of α-Mg in Mg-Al alloys.

2.4. New Technological Developments for Particle Dispersion in Liquid Metal

The melt conditioning (MC) technology by intensive shearing was firstly developed and applied to achieve a fine and uniform grain structure for Mg alloy by Fan and co-workers (Fan et al. 2011). The MC technology can be combined with many casting process, such as direct chill (DC) casting, twin roll casting (TRC) and high pressure die casting (HPDC), for liquid metal conditioning prior to solidification process. During the MC process, the high turbulence created by high shear device subject melt to intensive shearing at a high shear rate (Utomo et al. 2009). Significant improvement in microstructure and reduction in macro-segregation was observed in Al and Mg alloy caused by enhanced heterogeneous nucleation (Patel et al. 2013).

With the good performance of high shear device at high service temperature, the intensive shearing of MC technology is also suitable for particle dispersion in the metallurgical applications of reinforcement and inoculant in light metals as the high turbulence and high shear rate enhance the breakup of solid particle clusters in liquid medium. Two types of high shear devices have been developed in-house: a twin-screw device and a rotor-stator mixer. Both of equipment has been tested to provide intensive shearing on the liquid metal prior to the final casting process.

2.4.1. Rotor-stator Mixer

High shear mixers, also known as high shear reactors, rotor-stator mixers, and high shear homogenizers have been widely used in chemical, pharmaceutical and food industries for emulsification, suspension and chemical reaction purpose (Atiemo-Obeng, Calabrese 2004). They are characterised by high rotor tip speeds (10-50 m/s), high shear rate (10^4-10^5 s^{-1}) and highly localized energy dissipation rates near the mixing head comparing to conventional mechanically stirred vessels (Zhang et al. 2012).

Due to the high service temperature and severe chemical reaction between the liquid metal and corresponding device components, high shear device was hindered from application in metallurgy industry. Fan and co-workers developed a new system of high shear mixer (Fan et al. 2011) with different material selection for MC process suitable for various liquid metal treatments. It provides intense melt shearing and high intensity turbulence to

liquid Mg alloy treatments and gaining a refined microstructure, uniform chemical composition and well dispersed intermetallics.

The typical geometrical designs of rotor-stator mixers are shown in **Figure 2.7**. The melt is sucked into the mixing chamber once the rotor starts to rotating at high speed (10^3~10^4 rpm), and pushes the melt into apertures on the stator by the centrifugal forces of rotor blade and jets out at an increased velocity compared with the input flow at the bottom of mixer. With the velocity difference, a negative pressure is build up to suck alloy melt into the high shear chamber. This leads to a continuous flow circulation (**Fig. 2.8**) created in the melt container. The high shear effect continuously applied on the melt in the gap between rotor and stator and also the apertures passing by.

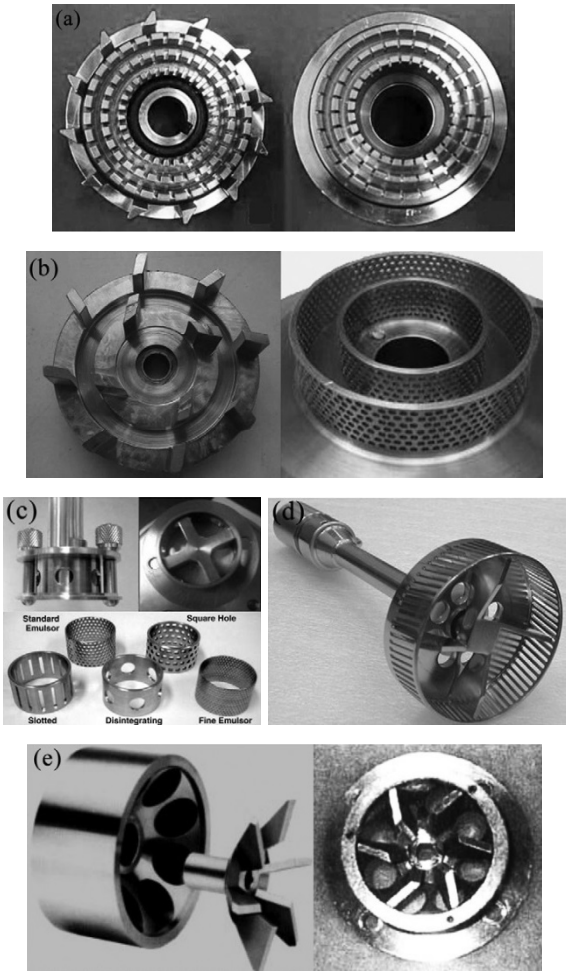

Figure 2.7 The typical geometrical design of rotor-stator mixer for high shear treatment, (a) the teethed in-line unit, (b) the blade-screen in-line unit, (c and d) the radial-discharged units and (e) the axial-discharged unit (Zhang et al. 2012).

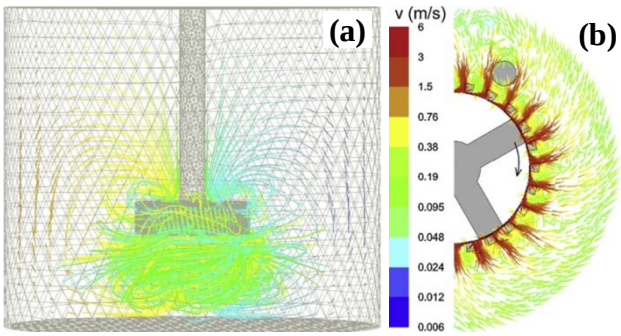

Figure 2.8 The simulation of flow pattern of liquid with rotor-stator mixer processing, (a) global view of flow field (Barailler et al. 2006) and (b) detailed section of mixing head (Utomo et al. 2009).

2.4.2. Twin-screw Device

Twin-screw mixer is popular in the plastics industry to obtain good mixing of polymer powder/granular with additives such as stabilizers, plasticizers, colouring pigments, etc. (Edwards, Baker 1992). The main advantages of the twin-screw device are the excellent dispersive mixing of materials with high viscosity, continuous processing and multistage capability (Jiang 2013). Traditionally, application of twin-screw device to liquid metals rarely has been reported due to the high service temperature and severe chemical reactions between the liquid metal and corresponding components of twin screw device.

In 2000, a new twin-screw device for application to liquid metal was developed by Fan and co-workers for melt conditioning of various melts (Tang et al. 2003, Tang et al. 2004). The device is constructed with five main sub-systems (Fan, Xia et al. 2009), (a) a driving motor as power system to rotate twin-screws, (b) the feeder and treatment barrel as melt flow system, (c) the C shape heating elements embracing treatment barrel and thermal couple as temperature maintain system to keep the melt treated alloy at a certain temperature, (d) a pair of co-rotating and intermeshing screws apply high shear on the alloy melt, and (e) a control valve is used as the melt releasing system to output treated melt to down-stream process when treatment completed (**Fig. 2.9**).

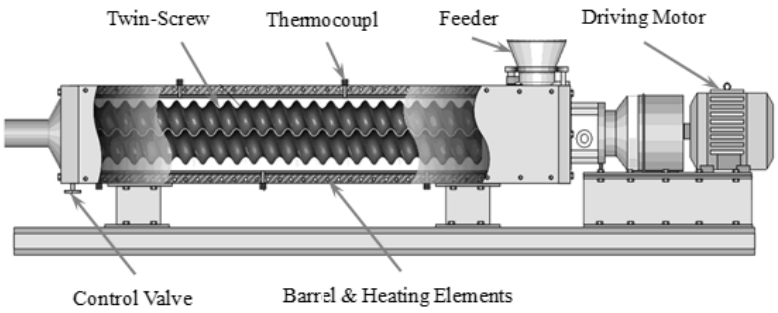

Figure 2.9 Schematic illustration of the twin-screw device for high shear treatment (Tang et al. 2003).

The process starts with the liquid metal fed into the treatment chamber with pre-set temperature, and then the twin-screws rotate at speed up to 1000 rpm using driving force from motor (Fan et al. 2009). The control valve releases the treated melt after twin-screw high shear at an accurate temperature and a given time (Jiang 2013). From the schematics of the twin-screw device, it shows that the high shear applied on the melt where the screws are in contacted with each other and screw tip close to the barrel wall (**Fig. 2.10**).

With the distinct advantage for viscous liquid applications, the twin-screw device is capable of being operated at temperatures above or below the liquidus of the liquid feed to provide conditioned liquid metal or highly sheared semi-solid slurry (Babu et al. 2013). Previous research show that conditioned Mg alloy melt treated by twin-screw device has a refined microstructure, uniform distribution of solute and well dispersed distribution of inclusion particles (Fan et al. 2009). Moreover, the process of twin-screw device connected to HPDC which operated at semi-solid range successfully produced Al/SiC and Al/graphite composites with excellent distribution of reinforcing particles dispersion (Tzamtzis et al. 2009, Barekar et al. 2009).

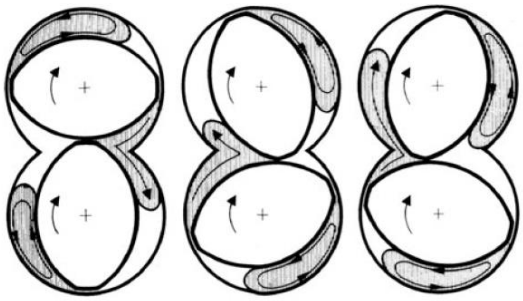

Figure 2.10 Section view of the flow pattern of liquid with twin-screw device processing (Manas-Zloczower 2012).

2.5.Twin Roll Casting of Magnesium Alloy and its Composites

Twin roll casting (TRC) process, is one of the direct strip casting methods, produces metallic sheet directly from the molten metal with minimised subsequent secondary processing. The process has come a long way since Sir Henry Bessemer's attempt of twin roll casting of lead and tin strip in 1865 (**Fig. 2.11**) and now it is used by a large range of ferrous and non-ferrous alloys with both thick and thin gauge strip/sheet/plate (Barekar, Dhindaw 2014).

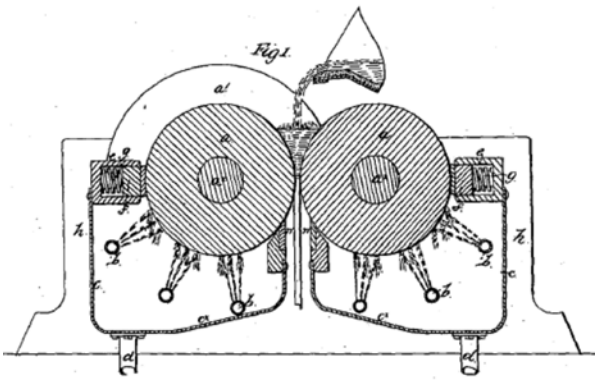

Figure 2.11 Schematic illustration of Bessemer's twin roll caster (Ferry 2006).

The advantage of this near-net-shape casting route is the avoidance of large amount of down-stream processing before the casting sheet/strip used for final shape forming. Therefore, the potential for large savings in the capital and operational cost make the direct strip casting process become popular over ingot casting in the 1950s and currently TRC process is accepted globally as a cost-effective method for producing Al product and commercialized in the steel industry (Ferry 2006).

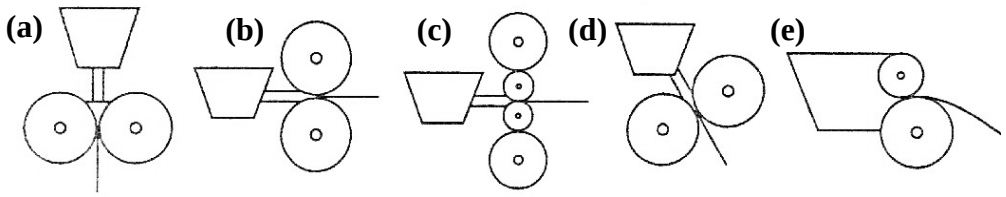

Figure 2.12 Schematic illustration of the design of different variety for twin roll caster, (a) vertical, (b) horizontal (2-High), (c) horizontal (4-High), (d) inclined, and (e) twin roll asymmetric configuration (Hendricks 1994).

The development of TRC equipment is also increasing for a range of different purposes (**Fig. 2.12**). The selection of twin roll caster highly depends on the alloys to be cast, the melt feeding system design, the specific strip quality control. Generally, TRC of steel is mainly focused on the vertical TRC technology, however Al industry is interested in horizontal technology (Ferry 2006). For the strip quality control, some specialized modification was applied on the basic model of TRC technology. The 4 High horizontal designs (**Fig. 2.12**(c)) of TRC is utilised in thin gauge Al strip casting as the process requires high casting speeds and high rolling loads. The two backup rolls on the 4 High horizontal TRC reduce the buckling defects in the strip and accurately control the strip thickness with economical setups (Thomas 2003). The asymmetrical arrangement of two rolls in **Figure 2.12**(e) is to tilt the basal texture evolution. This concept was first introduced in the hot rolling process to imposing shear texture in Al rolling sheet with

shear deformation due to different circumferential velocities of two working rolls (Lee, Lee 2008). With the magnesium market expansion, this technology is employed to reduce the severe basal texture of rolling Mg sheet by a rotation from the normal direction to the rolling plane (Zhao et al. 2012).

2.5.1. State of Art

For the TRC of Mg alloys, the first attempt was made by Dow Chemical Company in the early 1980s (Ferry 2006). In the 2000's, research groups in Korea, Australia, Germany, Japan, Turkey and China were involved in TRC process development for Mg alloy in laboratory and pilot plant scale (Liang, Cowley 2004). Such large investment by many research institutes and companies in the strip casting of Mg alloy is driven by the limited production around 1000 tonnes per annum (Liang, Cowley 2004) due to the high production costs of the conventional process. Compared with Al alloy strip casting, TRC of Mg alloy has more challenges in physical and chemical properties of Mg alloys and engineering design (**Table 2.1**).

Table 2.1 Challenges related with TRC of Mg alloys (Ferry 2006, Liang, Cowley 2004).

Challenge	Features	Potential solution
Oxidation	Molten Mg readily oxidizes and ignites without good gas protection system and control	Development of safe protection for both molten Mg and containment materials
Solidification rate	Lower specific heat and latent heat of fusion cause molten Mg to freeze faster than wrought Al alloys	Control the interfacial heat transfer of TRC process
Freezing range	Larger freezing range of Mg alloys can lead to the formation of cracks and segregation defects in the as-cast strip	New Mg alloy system development
Formability	The formability of TRC Mg alloy sheet need to advance the material properties in making complex and difficult-to-form components	Reducing the deformation aspect in order to modify the dominant basal texture
Cost and performance	Reduction of operational cost is a continuous requirement from industry. TRC strip must be able to compete with other materials	Compared with conventionally produced Mg sheet, TRC is the most cost-effective process.

With extensive research and design investments, numerous organizations worldwide compete to develop TRC technologies for Mg alloy sheet production. The current R&D status of Mg TRC technologies is summarized in **Table 2.2**. Commercial Mg alloy sheets by these suppliers are already available with strip width from 250 mm to 1500 mm in the thickness selection of 2-8 mm. However, the major products are limited to the AZ31B, AZ61 and AZ80 alloys, some supplier are able to produce AM series Mg alloy but in small sheet scale. The high strength ZK series Mg sheet by TRC process is rarely reported. The research of TRC on different alloy system in pilot plant scale is still extensive investment direction.

In addition to Mg alloy sheet, the advantage of TRC process as cost effective fabrication method is also expected to benefit Mg matrix composites. The current reports on the Mg matrix composite strip are mainly from Haga and co-workers focusing on the continuous fibre reinforced Mg matrix composites and development of multi-alloy laminar composites fabrication methods (Haga, Takahashi 2004, Haga et al. 2007, Haga, Suzuki 2003). For the metal matrix composites reinforced with discontinuous reinforcement has been rarely reported (Karnezis et al. 1995, Li, Huang 2014) .

Table 2.2 The current R&D status of Mg TRC (Park et al. 2009).

Country	Organization	Dimensions of cast strip (Width × Thickness, mm)
Korea	POSCO	600 × 4.5
Japan	Mitsubishi Aluminium	250 × 5
	Gonda Metal	400 × 2-6
China	Luoyang Copper	600 × 7
	Yinguang Magnesium	600 × 2-8
Australia	CSIRO	600 × 2.3-5
Germany	MgF	700 × 4-7
	Magontec	700 × 4.5
Turkey	Tubitak	1500 × 4.5-6.5

2.5.2. The Influence of Processing Parameters on Twin Roll Casting Process

Molten metal is transferred from a holding furnace or crucible into the feeding system, then the melt enter the moving mould and comes into contact with twin roll surface from the tip of nozzle (Ferry 2006). Thus melt temperature at nozzle tip determines the superheat of melt flow during the casting process. So the tip is critical in TRC process, as

it controls the melt flow at a constant level to maintain the integrity of the solidified strip, keeps the melt temperature stable to build up uniform thermal field and distributes the melt to the required strip width with equal supply (Merchant et al. 1989).

Figure 2.13 is a schematic illustration showing the geometry of nozzle and twin roll location with the liquid and solid zone of melt in the roll gap. Once the melt contacts with the roll surface, solidification begins at the meniscus point (A) where the first contact area of melt onto roll surface. After that, the two shells of solid continuously grow with the melt flow forward through the melt pool (B). The distance from meniscus point to the complete solid point at B is named sump area (indicated with β) (Ferry 2006, Bayandorian, Huang et al. 2011). The semi-solid area in between liquid and solid is referred as mushy zone. The setback is defined as the distance between nozzle tip and kissing point (where the roll gap is at a minimum) as indicated in **Figure 2.13** with symbol α. The tip setback depends on the fitness of nozzle tip design to roll surface. With the same geometric design, the setback increases or decreases with an increasing or decreasing diameter of rolls, respectively. As the TRC process is the combination of casting and hot rolling, the point where solidified metal has reached adequate strength to maintain a load is the deformation starting point (Bradbury 1994, Ferry 2006).

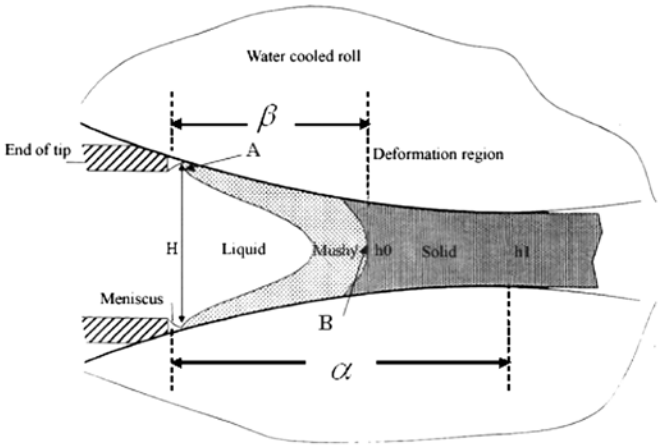

Figure 2.13 Schematic illustration of geometry of nozzle, twin roll location and regions of metal from liquid state to the solidified strip (Bradbury 1994).

Westengen and Nes proposed the following formula (Westengen, Nes 1984) to relate the processing parameters in the view of geometrical calculation,

$$\beta = \frac{H}{2}\left\{\frac{\left[\frac{2(\alpha-\beta)^2}{D}\right]+h_1}{h_1}\right\}^2 \tan\phi_0 \qquad (2.4)$$

where β is the length of the sump depth, α is the distance of the tip setback, D is the roll diameter, h_1 is the final strip thickness and $\phi_0$is the average angle between deformed grains and casting direction. The deformation of hot rolling during casting is also defined by Westengen and Nes (Westengen, Nes 1984),

$$\varepsilon(\%) = \frac{(h_0 - h_1)}{h_0} \approx \frac{(\alpha-\beta)^2}{(\alpha-\beta)^2 + h_0 D} \times 100 \qquad (2.5)$$

where h_0 is the initial thickness of the solidified strip. According to Berg's work, the deformation of as-cast strip by conventional caster is around 30-60% (Berg, Hansen et al. 1995) depending on the roll diameter D and setback α.

Casting parameters, such as casting speed, roll gap, tip setback and casting superheat, are critical to obtaining TRC strip with improved quality and eliminated surface and internal defects by influencing the solidification and deformation behaviour of the melt during TRC process. With the experimental observations and numerical simulations, the influence of these casting parameters may be revealed.

Pouring temperature

As with all casting methods, TRC process is also highly influenced by the pouring temperature. The experimental results on AZ91 alloy produced by TRC process shows that the non-uniformity of microstructure increased with increasing pouring temperature and finer dendritic structure of α-Mg grain is observed with lower pouring temperature (Bayandorian 2010).

Casting speed

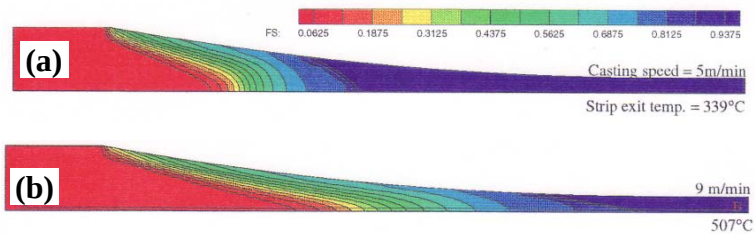

Figure 2.14 Simulating results of sump shape and strip exit temperature with casting speed variation, (a) low speed of 5 m/min with 339°C strip exit temperature and (b) high speed of 9 m/min with 507°C strip exit temperature (Bradbury 1994).

Casting speed is one of the important factors that influence the TRC process through the inner thermal field and the strip quality. **Figure 2.14** shows the simulation results of the

sump shape with the different casting speed of 2 mm gauge Al strip (Bradbury 1994). The fraction of solid (FS) of Al alloy during TRC with different casting speed is presented with colour form red to blue in the indicating scale. With slower casting speed, the higher portion of strip with high FS is observed in **Figure 2.14(a)**. In contrast, increasing the casting speed enlarge the sump depth and increased strip exit temperature (**Fig. 2.14(b)**).

Figure 2.15 shows the surface quality of TRC AZ91D strip with different casting speed from 22.5 mm·s^{-1} to 129.9 mm·s^{-1} (Bayandorian 2010). With the increased casting speed, the strip quality contains increased defects. This is consistent with the results from simulations on the sump depth and strip exit temperature. The high casting speed reduces the contact time of melt with water cooled twin roll surface, this lead to a reduced heat transfer from melt to the rolls and thus raises the strip exit temperature. As a result, the droplets left on the strip and thus surface defects form.

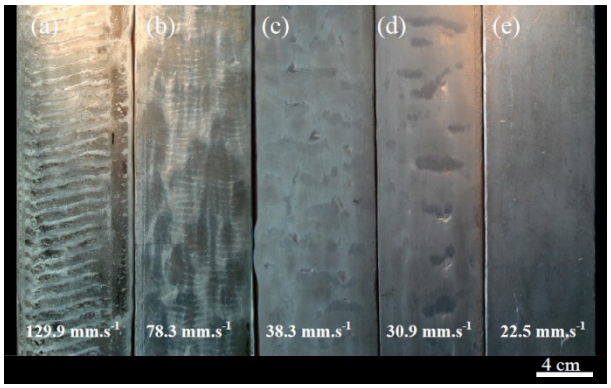

Figure 2.15 Surface quality of AZ91 D alloy produced at 615±5°C with different casting speeds, (a) 129.9 mm·s^{-1}, (b) 78.3 mm·s^{-1}, (c) 38.3 mm·s^{-1}, (d) 30.9 mm·s^{-1}and (e) 22.5 mm·s^{-1}(Bayandorian 2010).

Tip setback

Tip setback is an essential parameter which determines the pattern of TRC thermal field by the geometric relationship between the nozzle tip and twin roll kissing point. From one side, with increasing tip setback, the roll separation force is easily increased and increased the inner stress of as-cast strip. On the other hand, the simulation results (Bradbury 1994) show that sump is closer to the twin roll kissing point (**Fig. 2.16**) with increased strip exit temperature. It indicates that the effect of tip setback influence the TRC process in both directions, the selection of suitable value of tip setback depends on the preference of as-cast strip properties to be less residue stress or enhanced heat transfer during the TRC process.

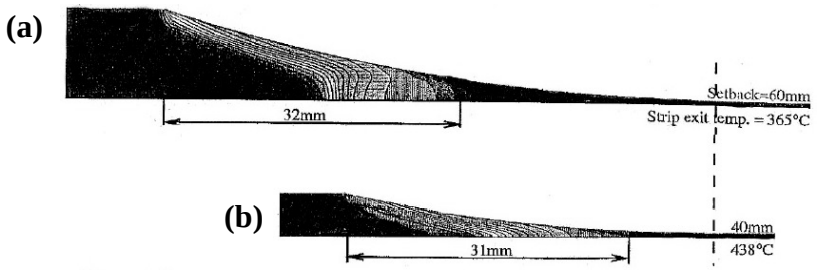

Figure 2.16 Simulating results of thermal field of Al-8Cu alloy with different tip setbacks, (a) 60 mm setback and (b) 40 mm setback (Bradbury 1994).

In this Chapter, previous research on the fundamental understanding of adhesion and dispersion of the rigid particles was reviewed. In metallurgy, the typical technological challenges involving particle distribution in particulate reinforced metal (Al and Mg) matrix composite preparation by liquid metal method and effectuate the inoculant as the heterogonous nucleation site in the dilute Mg alloy are discussed. The newly developed high shear technology in liquid metal is adapted to solve the particle agglomeration in metallurgy illustrating the versatility of such device. The high cooling rate of TRC process helps to maintain the particle distribution in the liquid metal by high shear and assist demonstration of the advantage of high shear technology to the particle distribution in the metallurgical application.

Chapter 3 Experimental Procedure

3.1. Materials and Facilities

3.1.1. Materials

The Al and Mg alloys studied in present work were commercial A356 and AZ31 alloy provided by *Norton Aluminium Ltd, Staffordshire, UK* and *Magnesium Elektron Ltd, Manchester, UK*, respectively. The chemical compositions of the as-received alloy ingots are shown in **Table 3.1** & **3.2**.

Table 3.1 Chemical Composition of Commercial A356 Alloy (in wt%)

Condition	Cu	Mg	Mn	Si	Fe	Zn	Ti	Others
Standard	<0.25	0.25~ 0.45	<0.10	6.5~ 7.5	<0.20	<0.10	<0.20	<0.05 each
As-received	0.08	0.45	0.12	6.76	0.22	0.08	0.11	<0.05 each

Table 3.2 Chemical Composition of Commercial AZ31 Alloy (in wt%)

Condition	Al	Zn	Mn	Si	Fe	Cu	Ni	ppmBe
Standard	2.5~ 3.5	0.6~ 1.4	0.2~ 1.0	<0.10	<0.005	<0.05	<0.005	-----
As-received	3.09	1.06	0.49	0.067	0.003	0.002	<0.001	12

The compositions of as-received A356 and AZ31 alloy was obtained by an arc-spark optical emission spectrometer (*Foundry Master Pro, Oxford Instruments, Oxfordshire, UK*) which include a solid-state spark source, a vacuum system, an optical system, and an output system (Jiang 2013), shown in **Figure 3.1**. A piece of sample with size of 50mm×50mm×20mm was sectioned from as-received alloy ingot. For chemical composition analysis, the 50mm×50mm surface of alloy sample was coarse ground with P120 SiC paper to obtain a flat testing surface and then washed by ethanol.

The silicon carbide particle (SiC_p) used in present work as ex-situ inoculant (reinforcement) was provided by *Electro Abrasives Corporation, NY, USA*. This black α-SiC_p has a hexagonal crystal structure and angular shape with F800 particle size (equivalent to 6.5 μm mass media). The morphology of SiC_p in **Figure 3.2** shows a clear surface with limited contamination.

Figure 3.1 The photo of Foundry Master Pro (Oxford Instruments).

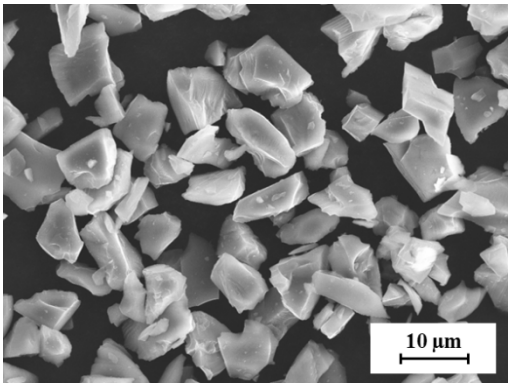

Figure 3.2 Morphology of as-received SiC_p used in present study.

3.1.2. Facilities

Induction furnace

The induction furnace (**Fig. 3.3**) provided by *Meltech Ltd, Suffolk, UK* was employed for SiC_p reinforced aluminium matrix composites fabrication. The furnace equipped with a drop coil arrangement and Pulsar inverter with power up to 125kW and frequency up to 3000 Hz for smaller non-ferrous alloy melting application.

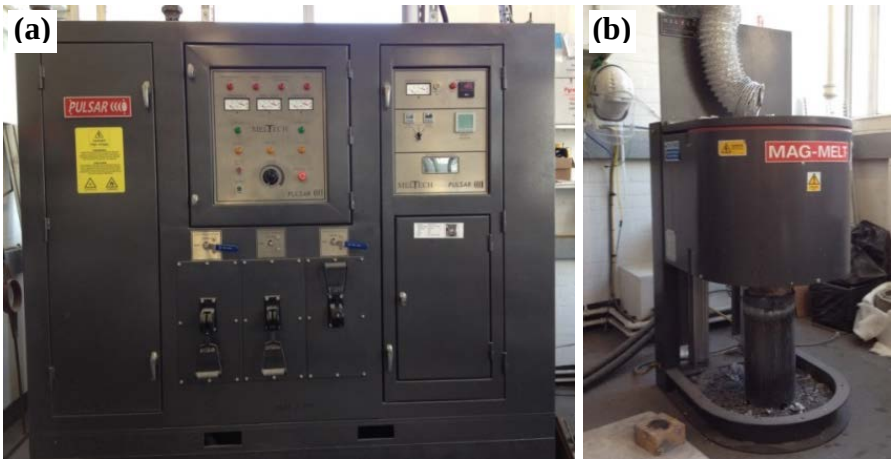

Figure 3.3 The induction furnace used in the research, (a) control panel and (b) raisable coil arrangement.

Semi-sealed tilting furnace

The in-house built semi-sealed tilting furnace specifically designed for Mg alloy melting and treatment with protective N_2+SF_6 gas coverage to further prevent the fire hazard due to the high oxidation tendency of Mg alloy melt. The internal design and structure was shown in **Figure 3.4**.

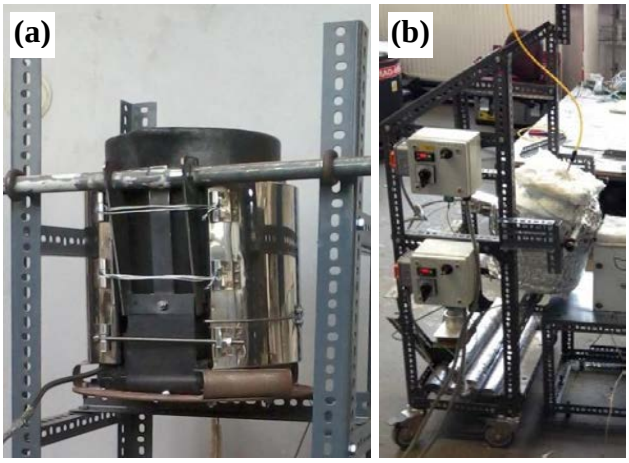

Figure 3.4 The semi-sealed tilt furnace with protective gas covering for Mg alloy melting, (a) inner design and (b) frame structure.

Four wheels were placed under the tilting furnace to allow movement of the furnace with the melt inside the furnace. A stainless steel crucible was encircled by 3 sets of heating elements which provide a melt temperature up to 750°C with 4 kg Mg alloy capacity. The outside surface of tilting furnace was covered with heat resistant super-wool to reduce the thermal loss and maintain the melt temperature. For pouring the furnace could be tilted manually up to 90° maximum.

Rotor-stator mixer

The rotor-stator mixer (*Zyomax Ltd., Uxbridge, UK*) employed in this research contains a rotating rotor (four blades impeller) with a stationary stator incorporating multi rows of apertures at the bottom. The inner diameter of stator was 32 mm and the gap between stator and edge of rotor blade is 0.1 mm. Total of 72 circulate apertures homogeneously located in 4 rows at the bottom of stator with 2.5 mm diameter of aperture. The rotor of mixer is driven by a motor through the shaft when the mixer is switched on. The rotor-stator mixer is made with either SiAlON ceramic or stainless steel for Al alloy and Mg alloy application, respectively. The geometrical schematic of rotor-stator mixer is shown in **Figure 3.5**.

Figure 3.5 The schematic illustration of rotor-stator mixer for high shear treatment (Jiang 2013).

The melt is sucked into the mixing chamber once the rotor start to rotating at high speed (1000~10000 rpm) (Fan et al. 2011), pushed into apertures on the stator by the centrifugal force of rotor blade and jetted out with increased velocity compared with the input flow at the bottom of mixer. With the velocity difference, a negative pressure builds up to suck alloy melt into the high shear chamber (Utomo et al. 2009). This leads to a continuous flow circulation (Fig. 3.6) created in the melt container. The high shear effect continuously applied to the melt in the gap between rotor and stator and also the apertures.

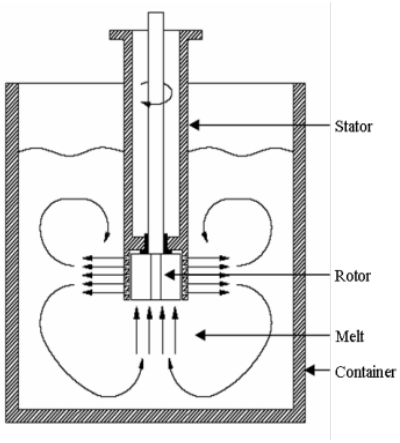

Figure 3.6 The flow pattern of liquid with rotor-stator mixer processing (Jiang 2013).

Twin-screw device

The patented twin-screw device for metallic material application is provided by *Zyomax Ltd., Uxbridge, UK* (**Fig. 3.7**). The process starts with the liquid metal feeding into treatment chamber at a pre-set temperature, and then the twin-screws rotate at speed up to 1000 rpm with the driving force from motor. The control valve release the treated melt after twin-screw high shear after a given temperature and time. The schematics of twin-screw device, show that the high shear applied on the melt where the screws contacted to each other and screw tip closing at the barrel wall.

Figure 3.7 Photo of the twin-screw device for high shear treatment of Mg alloy.

Horizontal twin roll caster

The twin roll caster used in this research is an in house built low pressure horizontal twin roll caster with small roll diameter and flexible roll position control. Twin roll casting is generally recognized as a combination of casting and hot rolling processes with the produced sheet/plate product containing a deformed microstructure. As the philosophy of present research is to evaluate the high shear effect on the particle dispersion and grain refinement, the twin roll caster is expected to act only as a continuous metallic mould with high cooling rate which can keep the original casting structure of Mg alloy.

In order to reduce the potential rolling effect on the cast strip, two major aspects are considered. First, the setback distance is reduced by the small diameter twin-roll as the setback decrease with the decreasing roll diameter at same nozzle tip geometrical design. Second, the roll position tolerance has been enlarged to minimise the resistance of strip separating force which could attribute to the deformation on the strip during casting process. The low force horizontal twin-roll caster (**Fig. 3.8**) has a range of 0-10 m/min liner speed. The steel rolls are 100 mm in diameter and 150 mm working width with an internal water circulation cooling system adjustable in the range of 5-30°C. The minimum gap of twin-rolls can be adjusted to 1 mm and related setback distance is 20 mm from nozzle tip to roll biting point.

During casting, the Mg melt was transferred from tilt furnace through a tundish then into the twin roll caster. The flow rate of the melt was controlled by the melt pouring head and the initial strip was lead out manually through twin roll gap by a 0.5 mm thickness stainless steel guide strip.

Figure 3.8 Photo of in-house built horizontal twin roll caster with integrated tundish and thermally controlled nozzle.

3.2.Processing Route

3.2.1. Aluminium Matrix Composites

The A356 Al alloy was used as the matrix alloy and angular shaped SiC_p with an average particle size of 4.5 µm were selected as the reinforcing elements. The matrix alloy was molten at 750°C (T_{mA356} ~ 615°C) in a clay-graphite crucible, which was heated in an induction furnace under the protection of N_2. The melting time of 2.5 kg A356 alloy by induction furnace was limited to 10 min (7 kg A356 alloy for 20 min) which could minimise the H_2 absorption of melt from environment compared with a normal electric resistance furnace. Subsequently, a pre-heated block of A356 alloy was put into molten alloy to adjust the A356 alloy melt to 600°C for reinforcing particle addition in semi-solid condition. The SiC_p were preheated in an oven at 400°C for 1 hour in order to remove the moisture, but lower than the sintering temperature of SiC particles, and then immediately added into melt as the melt temperature stabilised at 600°C. The processing route of experiment is shown in **Figure 3.19**.

The mixing was conducted in two stages. Firstly, the SiC_p were introduced to the melt and mixed with the help of mechanical stirring using a 45° four-bladed impeller at 650 rpm for 5 min (7 kg A356 alloy for 10 min). The stainless steel impeller was coated with BN suspension and preheated before using. Then the mixed A356 and SiC_p slurry was heated to 650°C and 730°C and subjected to high shear treatment using a rotor-stator mixer. The rotor-stator mixer is consisted of a motor driven rotor with an impeller and an open cylinder stator with narrow apertures at its bottom section. During mixing, the impeller rotates at a high speed between 1000 – 10000 rpm, sucking the melt into the

stator and forcing the melt through the narrow apertures and thus applying high shear rate to the melt (Fan et al. 2011, Patel et al. 2013). The material flow is characterized as a continuous turbulent convection (Utomo et al. 2009). In the present experiment, the high shear treatment was used at a speed of 5000 rpm for 5 min and the composite slurry was held at each temperature during shearing and was protected with N_2 gas.

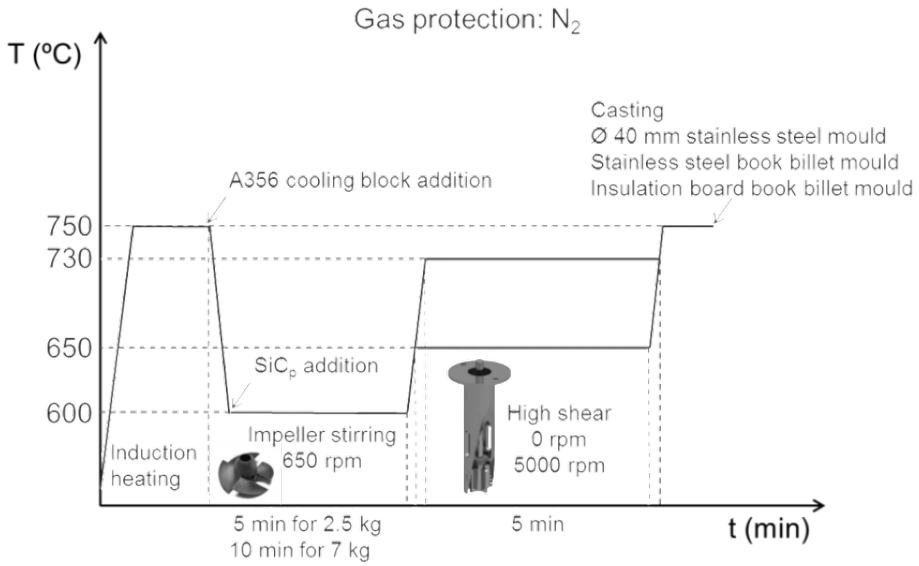

Figure 3.19 The processing route of A356/SiC_p composites with mechanical stirring and high shear by rotor-stator mixer.

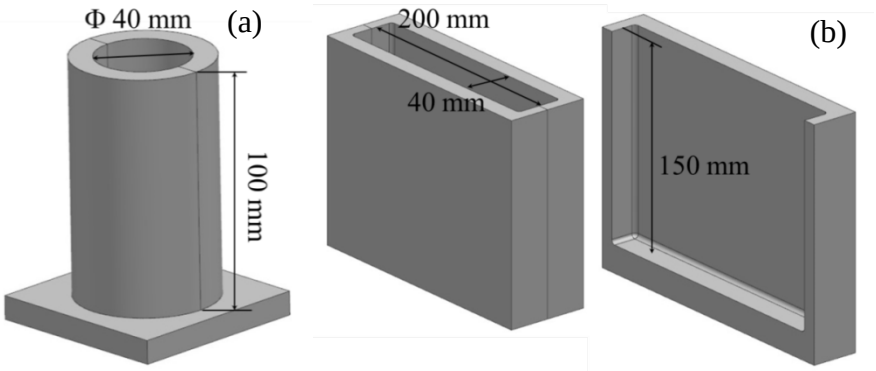

Figure 3.10 Geometry and dimension of different moulds for this research, (a) Φ 40 mm steel mould, (b) book billet mould with steel or insulation board.

This high shear treated composite slurry was then heated to 750°C and cast into Φ 40 mm stainless steel mould, stainless steel book billet mould with mould cavity size of 250 mm × 200 mm × 35 mm and insulation board book billet mould with same geometry and dimension as stainless steel mould. The dimensions of the different moulds are shown in **Figure 3.10**.

3.2.2. Magnesium Matrix Composites and their Twin Roll Casting Strip

The AZ31alloy was used as the matrix alloy and angular shaped SiC_p with an average particle size of 4.5 µm were selected as the reinforcing particles. The matrix alloy was melted at 680°C (T_{mAZ31} ~ 629°C) in a temperature controlled crucible, which was placed in semi-sealed mixing chamber with protective gas mixture of 0.42 vol% SF_6 in N_2. The SiC_p were pre-heated in an oven at 400°C for 1 hour and added to the AZ31 melt at 680°C immediately after the pre-heating. The mixing was conducted in two stages. Firstly, the SiC_p were introduced to the melt and mixed with the help of mechanical stirring using a 45° four-bladed impeller at 650 rpm for 5 minutes. Then the mixed AZ31 and SiC_p slurry was subjected to high shear treatment using a rotor-stator mixer. In this experiment, the high shear treatment was employed at a speed of 5000 rpm for 5 minutes and the composite slurry was kept at 680°C during shearing and was protected with N_2+SF_6 gas mixture. This high shear treated composite slurry was then cast into strip using the horizontal twin roll caster.

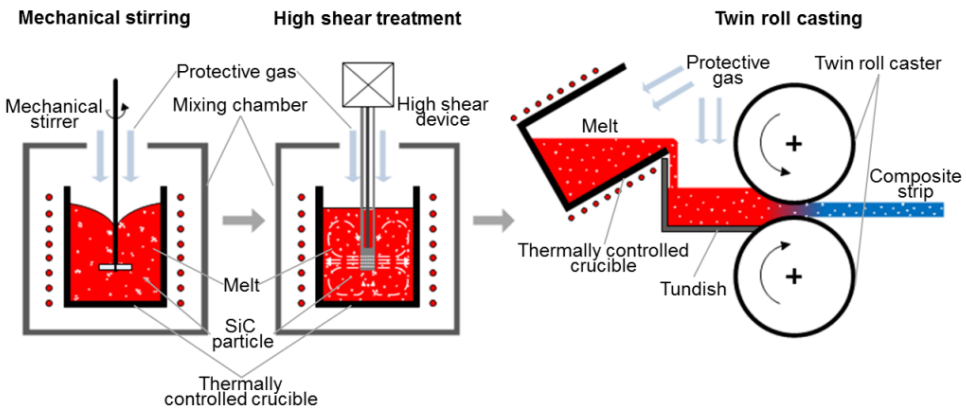

Figure 3.11 The schematic of SiC particle reinforced AZ31 Mg matrix composite strip casting process involving a two-stage mixing process and the TRC process. The inner dimension of crucible is Φ150 mm × 200 mm.

The processed composite strip is referred to as high shear (HS) strip in the following context. For comparison, AZ31/SiC_p composite strip was also produced using slurry subjected only to mechanical stir without high shear treatment and is referred to as non-high shear (nonHS) strip. The two-stage mixing process (mechanical stirring and high shear treatment) and the TRC process are schematically shown in **Figure 3.11**.

TRC process was conducted on an in-house-built horizontal twin-roll caster with an internal water circulation cooling system. The rolls were 100 mm in diameter with a

working width of 150 mm and 5 m/min rolling speed. The AZ31/5vol%SiC_p slurry of about 4 kg prepared with or without high shear treatment was fed to the caster through a stainless steel tundish with composites slurry temperature of 650°C. The setback of tundish tip to the roll biting point was 20 mm. Again, protective gas mixture of 0.42% SF_6 in N_2 was used to protect the slurry from oxidation.

Prior to tensile testing, the as-cast strip was homogenized at 400°C for 48 hour in a heat treatment furnace with forced air circulation, in order to reduce chemical segregation and residual stresses in the materials and water quenched to retain the solute solution at the homogenization temperature.

3.2.3. Melt Conditioned Twin Roll Casting Process for Magnesium Strip

Melt conditioning with inline rotor-stator mixer

AZ31 commercial alloy was molten in the semi-sealed tilting furnace at 680°C (T_{mAZ31} ~ 629°C) and hold at this temperature with N_2+SF_6 gas mixture to minimise the potential fire hazard due to the high oxidation tendency of Mg alloy melt.

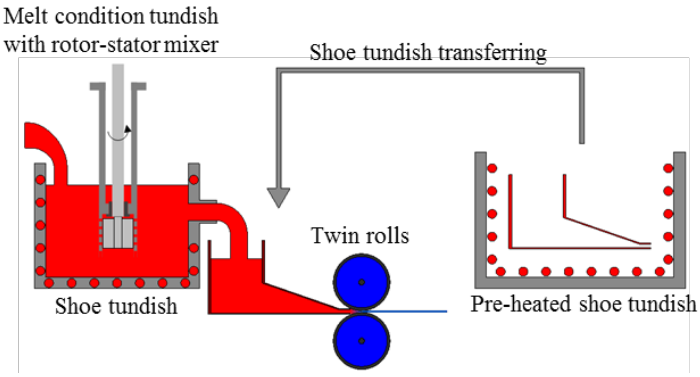

Figure 3.12 Schematic illustration of MC-TRC process with rotor-stator mixer inline high shear by steel tundish and shoe tundish combination. Schematic illustration of shoe tundish involved MC-TRC.

For the experiment with shoe tundish (**Fig. 6.4**), the steel shoe tundish was covered with 4 mm insulation and preheated in an electric resistance furnace at 800°C for 1 hour before casting. The steel tundish for high shear melt condition was set to 680°C with rotor-stator mixer merged in the high shear chamber of steel tundish and heat together. The steel tundish was also protected with N_2+SF_6 gas mixture. The shoe tundish was taken out from preheating furnace and placed between the steel tundish and horizontal twin roll, at the same time, the tilting furnace tilted manually to pouring AZ31 melt into steel tundish for

high shear treatment. When the pouring started at 680°C, the melt flow into the inlet of steel tundish continuously and then the liquid metal risen up from bottom into shear chamber and intensive high shear was applied by rotor-stator mixer with 5000 rpm positioned in the centre of shear chamber. The highly sheared Mg alloy melt was then guided to the horizontal twin roll caster through shoe tundish with 1 mm roll gap. The cast strip was caught and guided manually by a thin steel bar from the exit side of twin roll caster. The schematic of MC-TRC process was shown in **Figure 3.12**. For comparison, the AZ31 alloy without high shear treatment was also produced with same experimental set-up and the rotor-stator mixer kept still in the shear chamber inside steel tundish.

For the experiment with integrated tundish with thermally controlled nozzle, the integrated tundish (**Fig. 6.8**) was set to 650°C with rotor-stator mixer merged in the high shear chamber. The nozzle was also set to 650°C and covered with 2 mm insulation, and the 2.5 mm tip of nozzle was in contact with the roll surface. The integrated tundish was protected with the N_2+SF_6 gas mixture. At the beginning of the experiment, the tilting furnace tilted manually to pouring AZ31 melt into steel tundish for high shear treatment. When the pouring started at 680°C, the melt flow into the inlet of steel tundish continuously and then the liquid metal rise up from bottom into shear chamber and intense high shear was applied with the rotor-stator mixer at 5000 rpm positioned in the centre of shear chamber. The highly sheared Mg alloy melt was then guided to the horizontal twin roll caster through nozzle tip with 1 mm roll gap. To preventing side leaking of melt, anti-leakage dam made with insulation were placed in the gap of nozzle tip and side wall of twin roll caster. The cast strip was caught and guided out manually with a thin steel bar manually from the exit side of twin roll caster.

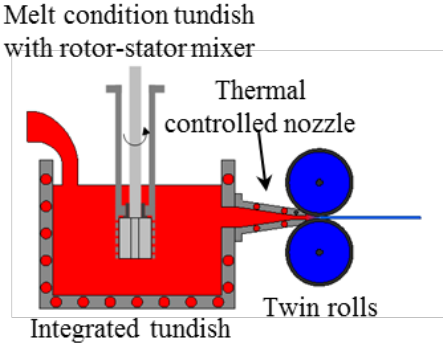

Figure 3.13 Schematic illustration of MC-TRC process with rotor-stator mixer inline high shear by integrated tundish and shoe tundish equipped with thermally controlled nozzle.

The schematic of MC-TRC process was shown in **Figure 3.13**. For comparison, the AZ31 alloy without high shear treatment was also produced with same experimental set-up and rotor-stator mixer kept still in the shear chamber inside steel tundish.

Melt conditioning with twin-screw device

AZ31 alloy was molten in an electric resistance furnace with steel liner inside at 680°C, and covered with N_2+SF_6 gas mixture. The treatment barrel within twin-screw device was heated up to 650°C with separate gas inlets of N_2+SF_6 gas mixture protecting melt feeder, treatment barrel and outlet valve. At the start of the melt conditioning, the 1.5 kg melt in the furnace were poured into twin-screw device through feeder. The twin-screw rotated at a speed of 800 rpm for 90 s, then the twin screws stop rotation and outlet valve released the high shear treated melt into ingot mould. Total 20 kg of high shear treated AZ31 ingot were prepared with twin-screw device for twin roll casting process.

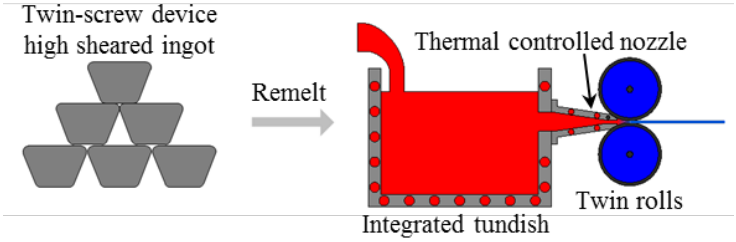

Figure 3.14 Schematic illustration of MC-TRC process with twin-screw high shear treated ingot by integrated tundish equipped with thermally controlled nozzle.

The high shear treated AZ31 ingot was molten in the semi-sealed tilting furnace with quantity of 4 kg at 680°C. The pouring tundish with thermally controlled nozzle was heated to 650°C for both tundish body and nozzle were protected with N_2+SF_6 gas mixture. When the experiment started, the tilting furnace was tilted manually to guide high shear treated AZ31 melt into pouring tundish and then guided to the horizontal twin roll caster through nozzle tip with 2.5 mm gap. The twin roll gap was set to 1 mm. To prevent side leaking of melt, anti-leakage dam made by insulation were placed in the gap of nozzle tip and side wall of twin roll caster. The cast strip was caught and guided out manually with a thin steel bar from the exit side of twin roll caster. The schematic of MC-TRC process was shown in **Figure 3.14**.

For comparison, the AZ31 alloy without high shear treatment with the twin-screw device was also produced by same experimental set-up.

3.3. Microstructure Characterization

3.3.1. Metallographic Sample Preparation

A356/SiC_p composite samples for microstructural characterization were taken from the Φ 40 mm cylinder ingot and book billet ingot. For Φ 40 mm cylinder ingots, all of the samples were taken 10 mm from the bottom of ingot with a section of 20 mm × 20 mm. For the book mould billets, the samples were also taken 10 mm from the bottom of the ingot and in the middle of long direction with a section of 20 mm × 20 mm. The ingots were sectioned with abrasive cut-off wheel, following by the compression mounting in Φ30 mm × 15 mm cylinder with Bakelite resin and SimpliMet 3000 mounting machine (*Buehler, UK*). For particle distribution analysis, microstructure and Vickers hardness test, metallographic samples were prepared following the standard route with a final polishing using an OP-S suspension (0.05 µm water based SiO_2 suspension).

Table 3.3 The metallographic sample preparation route for A356/SiC_p composites.

	Surface	Abrasive	Force	Time (m:s)	Base speed (rpm)	Head speed (rpm)	Rotation
1	UltraPrep	70 µm	25 N	Until planar	300	60	> >
2	TexMet P	9 µm MetaDi Diamond	25 N	5:00	150	60	> <
3	TexMet P	3 µm MetaDi Diamond	25 N	4:00	150	60	> >
4	ChemoMet	0.05 µm SiO_2 OP-S	25 N	1:30	150	60	> <

The sample preparation route is listed in **Table 3.3**, and the consumables are from *Buehler UK*. For elastic modulus and Brinell hardness test, the sample surfaces were ground and finished with 9 µm water based diamond suspension polishing. Baker's solution with 200 ml distilled water and 10ml fluoroboric acid was used for sample anodizing. The anodizing of A356/SiC_p samples was performed at 15V voltage, 70 s at room temperature using a DC power supply.

AZ31 and AZ31/SiC_p composites samples for microstructural characterization were taken along the longitudinal section (TD plane) and transverse section (CD plane) through the

middle of both HS and nonHS strip. For particle distribution analysis, five sets of samples were taken from the middle of composites strip, 500 mm from each other along the casting direction. AZ31/SiC_p composite samples of 10×10 mm in square shape for X-ray diffraction (XRD) analysis were taken from the centre of the HS strip. Metallographic sample preparation of AZ31 and AZ31/SiC_p composites were performed following the standard route with a final polish using a 0.05 µm oil base alumina suspension. The sample preparation route is listed in **Table 3.4**.

Table 3.4 The metallographic sample preparation route for AZ31 and AZ31/SiC_p composites.

	Surface	Abrasive	Lubricant	Force	Time (m:s)	Base speed (rpm)	Head speed (rpm)	Rotation
1	UltraPrep	40 µm	AutoMet oil	20 N	Until planar	300	60	> >
2	TexMet P	9 µm diamond Oil base	-/-	25 N	5:00	150	60	> <
3	TexMet P	3 µm diamond Oil base	-/-	25 N	4:00	150	60	> >
4	TexMet P	1 µm diamond Oil base	-/-	25 N	3:00	150	60	> >
5	ChemoMet	0.05 µm Al_2O_3 Oil suspension	AutoMet oil	25 N	2:30	150	60	> <

The oil based diamond suspension and alumina suspension are from *Metprep UK*. The polishing closes are supplied by *Buehler UK*. Ethanol solution with 5% HNO_3 was used as etchant for revealing α-Mg and β-$Mg_{17}Al_{12}$ phase morphology under optical microscope. For primary α-Mg grain size measurement, a solution of 4.2 g picric acid, 15 ml acetic acid, 70 ml ethanol and 15 ml distilled water was used for colour etching. Samples for particle distribution analysis were not etched. The fracture features of the AZ31/SiC_p composites tensile samples were examined with the scanning electron microscopy (SEM) immediately after tensile tests.

3.3.2. Optical Microscopy

The optical microscopic (OM) observations were performed on a Carl Zeiss AxioScope A1 optical microscope (**Fig. 3.15**) equipped with 2.5×, 5×, 10×, 20×, 50× and 100× objective lenses with bright field and polarization field mode. The images of sample

microstructure were captured by the AxioCam MRm digital camera on the top of microscope and saved with the image processing software AxioVision 4.9 (**Fig. 3.16**).

Figure 3.15 Photo of Carl Zeiss AxioScope A1 optical microscope.

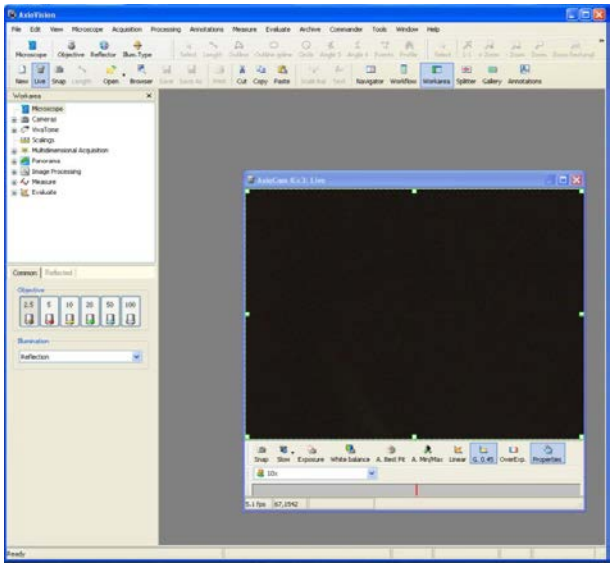

Figure 3.16 The interface of AxioVision 4.9 image processing software

3.3.3. X-ray Diffraction

The X-ray diffraction (XRD) analysis was conducted on a Bruker D8 Advance (**Fig. 3.17**) Cu-K_α source on polished sample surfaces. The 2Theta angle of XRD analysis was set between 25° to 80° with the step size of 0.01°/s and total scan time for each sample were approximately 100 min. The Bruker D8 Advance XRD was equipped with LYNXEYE

high resolution energy-dispersive1-D detector and DIFFRAC.SUITE software package for operation (*Bruker, Coventry, UK*).

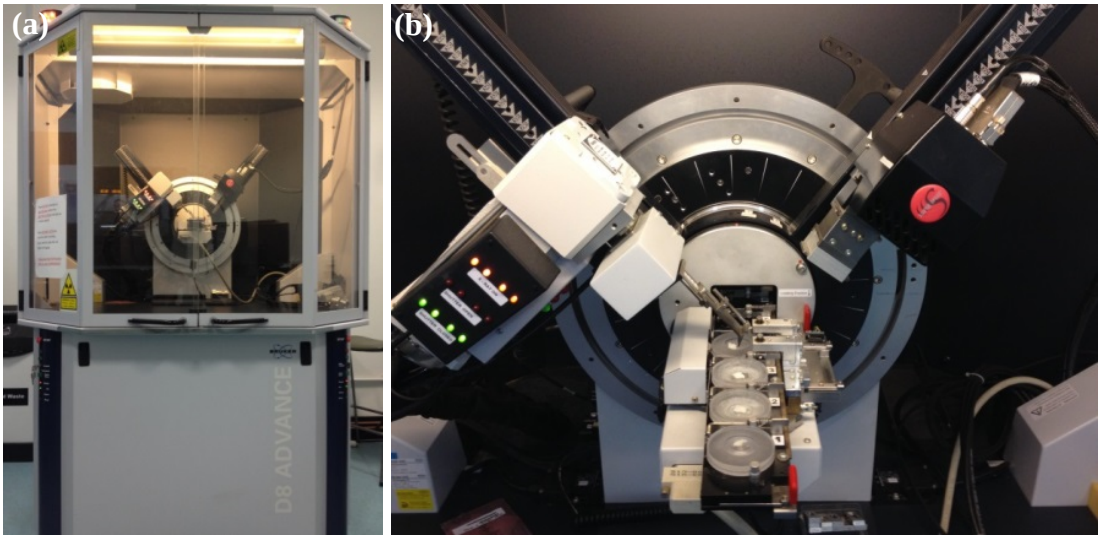

Figure 3.17 Photo of Bruker D8 Advance XRD (a) and energy-dispersive 1-D detector (b).

3.3.4. Electron Microscopy

Scanning electron microscopy (SEM)

The secondary and backscattered electron imaging and EDS mapping was performed on a Zeiss Supra 35 field-emission gun SEM (**Fig. 3.18**) equipped with energy dispersive X-ray spectroscopy (EDS) (*Oxford Instruments, Oxfordshire, UK*). The TEAM 4.3 software was used for processing EDS maps. An accelerating voltage of 20 kV and working distance at 6 mm were used for the microstructure observation and element mapping.

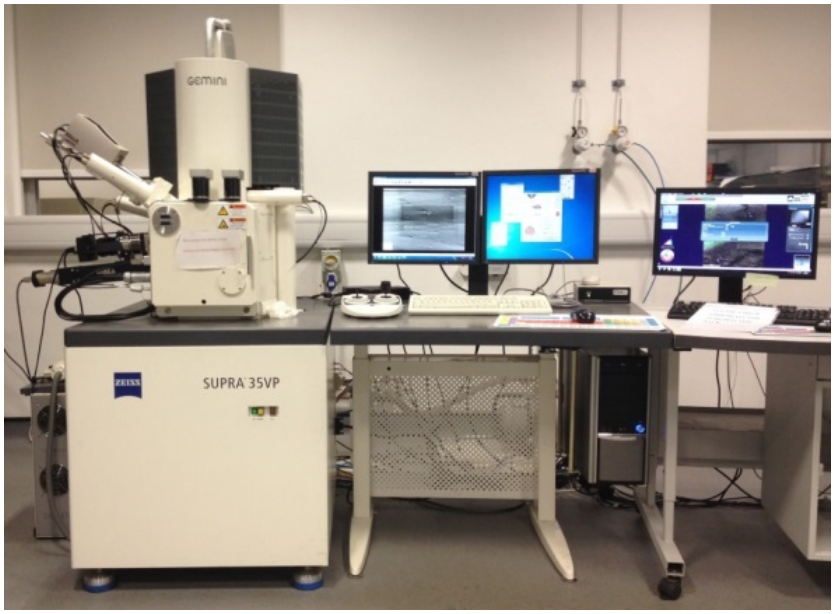

Figure 3.18 Photo of Zeiss Supra 35 field-emission gun SEM with EDS and EBSD detectors.

Electron backscattered diffraction (EBSD)

Electron backscattered diffraction of AZ31 and AZ31/SiC_p composite strips were performed on Zeiss Supra 35 SEM with high speed high sensitivity Hikari EBSD camera (**Fig. 3.19**). TEAM 4.3 software was used for operation mapping and OIM 7.3 software was used for the EBSD data analysis (*EDAX, NJ, USA*).

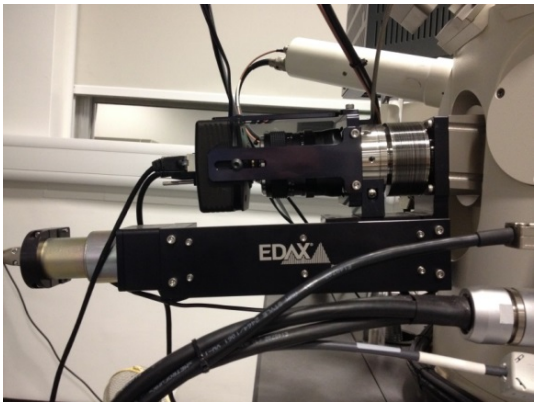

Figure 3.19 Photo of EDAX TSL EBSD camera.

The accelerated voltage used was 15 kV and working distance was 10 mm for both low magnification global mapping and local mapping at high magnification. The step size of EBSD mapping varies from 0.10 µm to 2.00 µm depending on the dimension of mapping area. The samples were held in 70° pre-tilt sample holder (**Fig. 3.20**). The sample preparation method differs for different materials for EBSD analysis. The AZ31 TRC strip was prepared by electropolishing with electrolyte of 15% HNO_3 in Methanol solution. The sample taken from longitudinal section prepared with standard mechanical polishing. Then the electropolishing processed with a voltage of 12 V at -30°C for 30s, immediately washing within methanol and blow dried afterward.

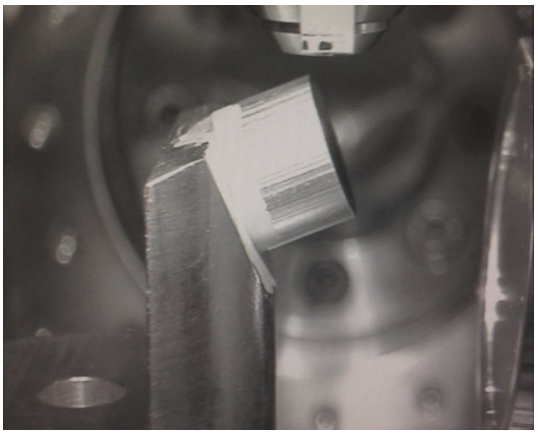

Figure 3.20 The sample position inside vacuum chamber of Supra SEM.

Due to the combination of ductile metallic matrix and hard brittle ceramic reinforcing particles, the electropolishing of AZ31/SiC_p sample was limited by the electrochemically inert SiC particles. The topography generated by electrochemical difference between AZ31 alloy and SiC would hinder the electron backscattered signal received by EBSD detector which led to a low indexing rate and inaccuracy. Alternately, the AZ31/SiCp composite strip was prepared with ion beam milling which minimise the polishing rate difference between metallic and ceramic phases. The sample taken from strip normal section and reduced the thickness to ~0.5 mm by standard mechanical polishing. For further sample surface polishing, a precision ion polishing system (PIPS) from *Gatan UK, Abingdon, UK* was used. The ion beam polishing was performed under 10^{-3} Torr vacuum and liquid nitrogen cooling environment with 5 keV voltage and 25 µA current beam generated from both guns to the top sample surface with 3° tilt. The process took 10 h to acquire stress free flat surface for EBSD analysis.

Transmission electron microscopy (TEM)

A JEOL2100 field emission gun transmission electron microscope (FEG TEM) shown in **Figure 3.21** was utilised for α-Mg and SiC phase interface observation using high resolution TEM imaging (HRTEM) and select area diffraction (SAD) acquisition with the accelerating voltage of 200 kV. A double-tilt holder (*JEOL Ltd., Tokyo, Japan*) was used in the TEM observation for high resolution bright field imaging. For the α-Mg and SiC phase interface observation, the sample was taken from normal section of AZ31/SiC_p composite strip, mechanical grinded to less than 70 µm thickness and cut into 3 mm diameter discs. Then a Gatan precision ion polishing system (PIPS) was used for ion beam thinning with 5.0 kV and 6° incident angle for 120 min and another 20 min by 4° incident angle to enlarge the thinned area on the composite sample.

Figure 3.21 Photo of JEOL2100 field emission gun transmission electron microscope.

3.3.5. Quantitative Metallography

The grain size measurements of α-Mg phase in AZ31 and AZ31/SiC_p composites strip were performed on Carl Zeiss AxioScope A1 optical microscope by polarization field with macro etched sample for α-Mg.

The mean linear intercept technique was used to quantify grain size with no less than 500 grains with the guidance of ASTM E 112 standard. The volume fraction measurements of SiC reinforcing phase in AZ31/SiC_p with and without high shear treatment were also processed on Carl Zeiss AxioScope A1 optical microscope with AxioVision 4.9 imaging process software. The grey contrast range of SiC particle under optical microscopy identified for phase distinguishing and to quantify the volume fraction. In general, the grey contrast method gives the area fraction of a given phases/particles in the image. With the random distribution of the phases/particles, the area fraction equals to the volume fraction in 3-dimensioned situations (Underwood 1970). For each data point, 5 sample areas were measured.

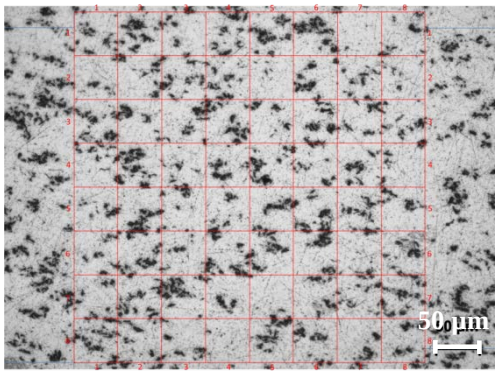

Figure 3.22 The Quadrat Method for AZ31/5wt%SiC_p composite strip fabricated with high shear treatment, the 8×8 quadrat is presented in red.

For the reinforcing particle dispersion quantification, Quadrat Method (Barekar et al. 2009) was employed with a given quadrat grid covering a sample field. The Skewness β value, expressed by following equation (Lloyd 1994):

$$\beta = \frac{q}{(q-1)(q-2)} \sum \left[\frac{N_{qi} - N_q^{mean}}{\sigma} \right]^3 \qquad (3.1)$$

where q is the total number of quadrats studied, N_{qi} is the number of SiC particles in the ith quadrat (i= 1, 2, ……, q), N_q^{mean} is the mean number of SiC particles per quadrat, and

σ is the standard deviation of the N_q distribution. For AZ31/SiC_p composites strips, 8×8 quadrat grids covering an area of 416 μm × 416 μm. More than 3500 SiC particles in 5 optical micrographs were counted for each sample (**Fig. 3.22**).

The hydrostatic weighing method (Hidnert, Peffer 1950) is used for the determining the density of A356/SiC_p composites. The composite samples were cut into cubic shape with the dimension of 20 mm × 20 mm ×20 mm. The sample is first weighed in air, and then weighed suspended in water. The density of composite sample is calculated from the weight in the air divided by its volume. This volume is equal to the loss of weight of the sample divided by the density of the water (1.000 g/cm^3) at room temperature. For each sample, the measurement of composite density is repeated 3 times.

3.4. Mechanical Property Tests

3.4.1. Tensile Test

The tensile samples of both HS and nonHS AZ31/5SiC_p strip were machined following the ASTM B557 standard along the strip casting direction. Mechanical properties were measured on an Instron 5500 Universal Electromechanical Testing System (**Fig. 3.23**) with constant cross head speed of 0.65mm/min (2×10^{-4} s^{-1} initial strain rate) and Bluehill software for test process control. All the tests were performed at ambient temperature (~25°C).

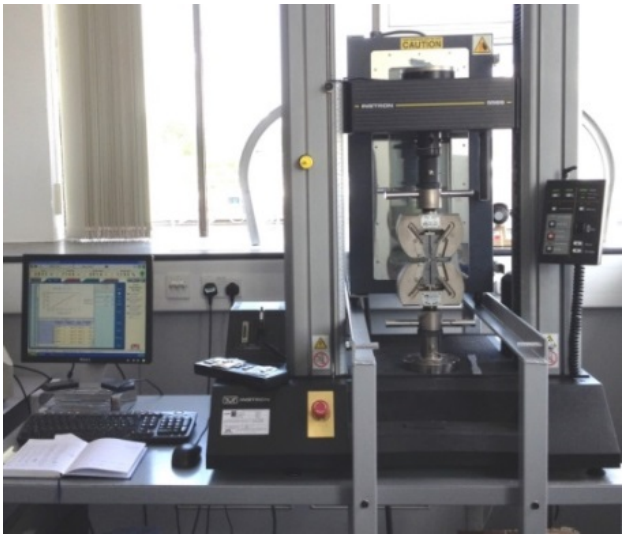

Figure 3.23 Photo of Instron 5500 universal electromechanical tester.

3.4.2. Hardness Test

Brinell hardness test

Brinell hardness test was performed on a Wilson BH3000 (*Buehler, UK*) Brinell hardness tester (**Fig. 3.24** (a)) with a load of 250 kgf, an load time of 5.0 s and a dwell time of 15.0 s. Samples for Brinell hardness test were sectioned from book mould ingot and Φ40 mm mould ingot, then grinded with 75 micron diamond coated grinding disc.

Vickers hardness test

Vickers hardness test was performed on a Buehler Micromet 5101 Vickers Hardness tester (**Fig. 3.24** (b)) with a load of 0.5 kg and for a dwell time of 10 s. Samples for Vickers hardness test were taken from the longitudinal section of both as-cast HS and nonHS strips with standard polishing process.

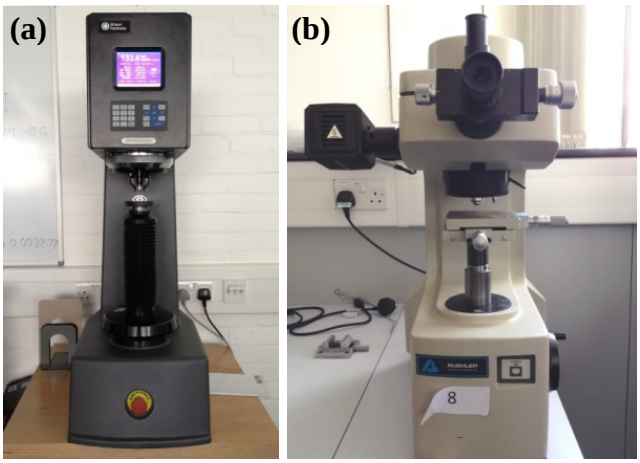

Figure 3.24 Hardness testing facilities used in the research, (a) Brinell hardness tester, and (b) Vickers hardness tester.

3.4.3. Elastic Modulus Measurement

The elastic modulus of a material is defined as the slope of tensile stress-strain curve in the elastic deformation region. The elastic modulus measurement performed with two experimental methods.

The measurement of AZ31/SiC_p composites was performed with stress-strain curve with uniaxial tensile test on an Instron 5500 Universal Electromechanical Testing System at room temperature. The elastic modulus (E) of A356/SiC_p composites was calculated with Poisson's Ratio (v) which can be expressed in the following equation (Birks et al. 1991):

$$E = \frac{V_L^2 \rho(1+v)(1-2v)}{1-v} \tag{3.2}$$

where

$$v = \frac{1-2(\frac{V_T}{V_L})^2}{2-2\left(\frac{V_T}{V_L}\right)^2} \tag{3.3}$$

and

$$V = \frac{T}{t/2} \tag{3.4}$$

V is the velocity of ultrasound wave travelling inside object, V_T and V_L represent Shear (transverse) velocity and Longitudinal velocity respectively, ρ is the density of object, T is the thickness of samples and t is the round trip transit time of ultrasound wave.

Figure 3.25 Elastic modulus measurement with ultrasonic thickness gauge (Olympus).

In this research, an Olympus 38DL PLUS ultrasonic thickness gauge (**Fig. 3.25**), a M112 broadband longitudinal wave transducer (10 MHz) and a V156 normal incidence shear wave transducer (5 MHz) were used for elastic modulus measurements of A356/SiC_p composites due to the inadequate castability of composites slurry for tensile sample casting. The composite samples were sectioned in 20 mm thicknesses following standard mechanical polishing with 0.05 μm SiO_2 suspension as the final polishing. For each sample, 10 points were measured for the elastic modulus calculation.

Chapter 4 Aluminium Matrix Composites: Results and Discussion

4.1. The Effect of High Shear on Aluminium Matrix Composites

Due to the demands of superior mechanical properties and light weight, the MMCs were expected to further advance the properties of conventional light metals (e.g. Al, Mg, Ti) in given applications (Lloyd 1994). Al and its alloys, as one of the most used light metals, have been widely used in the automobile, aerospace, electronics and package industries (Polmear, John 2005). Al-MMCs are also one of the first commercialized MMC materials in the world. In last two decades, extensive research conducted on the fundamental investigations and engineering development. A critical challenge for fabricating Al-MMCs, as for any other types of MMCs, is to overcome severe agglomeration of the reinforcing particles which deteriorate composites properties (Hashim et al. 2002a).

In the PM process, ball milling and tumble blending (Lenel 1980) is normally used to mix the reinforcing particles with the matrix powder. Mechanical stirring has been a routine method to mix the reinforcing particles in the molten matrix alloys using the casting route (Hashim et al. 2002a). The problem with the conventional mechanical stirring is that the shear rate applied is inadequate to break up particle agglomerations, particularly when the reinforcing particles are ultrafine (< 10 μm) and there is a high volume fraction of particles (Barekar et al. 2009). The turbulence generated in the melt surface during mixing using conventional mechanical stirring is a main cause of the gas entrapment in the matrix melt (Hashim et al. 2002b).

In order to overcome the cohesive forces with in the clusters embedded in the liquid melt, a rotor-stator device has been developed at BCAST for melt conditioning by high shear technology. It generates high shear rate (up to ~10^6 s^{-1}) with minimum turbulence on the melt surface (Fan et al. 2011, Patel et al. 2013). It has been shown that the application of the shear force can surpass the cohesive bonding of neighbour particles which dominates the agglomeration strength (Hansen et al. 1998), and thus can effectively break up agglomerations, leading to a more uniform reinforcement distribution with improved interfacial wettability between the matrix and reinforcing particles. The objective of this

part of the research is to investigate the effect of high shear provided by the rotor-stator mixer on the particle distribution in Al-MMCs.

4.1.1. Reinforcement Distribution

The microstructures of reinforcing particle distribution in A356/5wt%SiC_p composites with different fabrication parameters are presented in **Figure 4.1**. With mechanical stirring using steel impeller coated with boron nitride (Impeller stirring (IS)), the SiC particles with 5wt% addition was incorporated into the A356 alloy show large agglomerates (grey contrast in block) and porosities (dark contrast in block) in **Figure 4.1**(a) and (b).

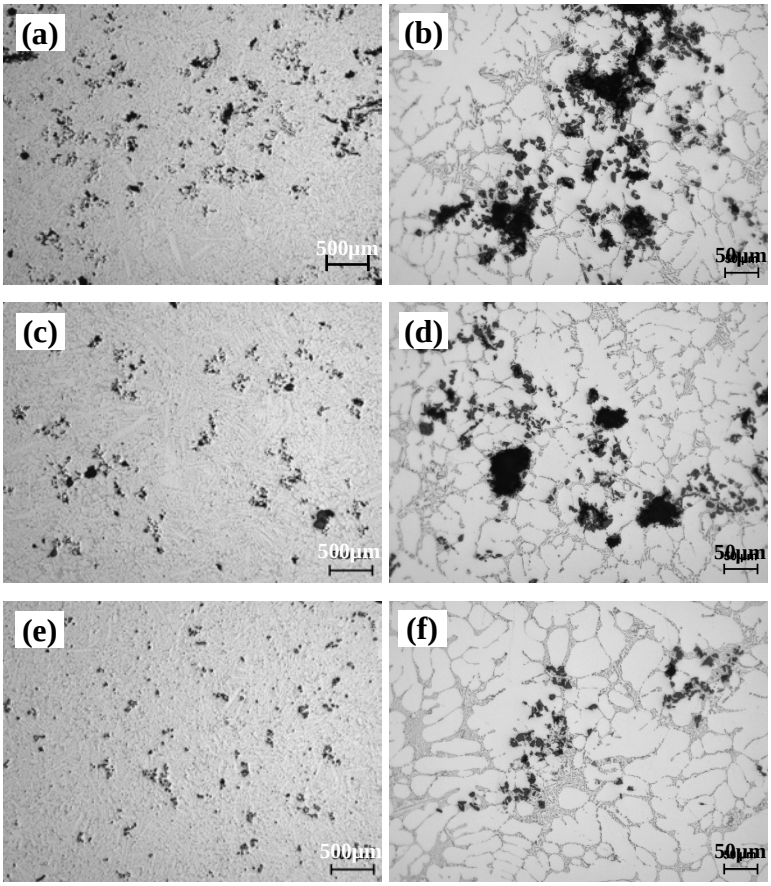

Figure 4.1 Microstructure of A356/5SiC_p composites fabricated by impeller stirring (IS) (a) and (b), impeller stirring and high shear treatment at 650°C (IS+HS) (c) and (d), and impeller stirring and high shear treatment at 730°C (IS+HS) (e) and (f). All samples were prepared with an Φ 40 mm steel mould.

Once the rotor-stator high shear (HS) treatment applied after mechanical stirring (IS+HS), the size of SiC agglomerates and amount of porosity decreased with improved reinforcement distribution (**Fig. 4.1**(c) and (e)). The reinforcement distribution of A356/5wt%SiC_p composites by IS+HS route was also influenced by the processing

temperatures with same treatment time. An improved SiC particle distribution with reduced SiC agglomeration size and minimised porosity volume faction can be observed by visual examination in **Figure 4.1**(e) and (f) with processing temperature of 730°C, compared with **Figure 4.1**(c) and (d) with 650°C.

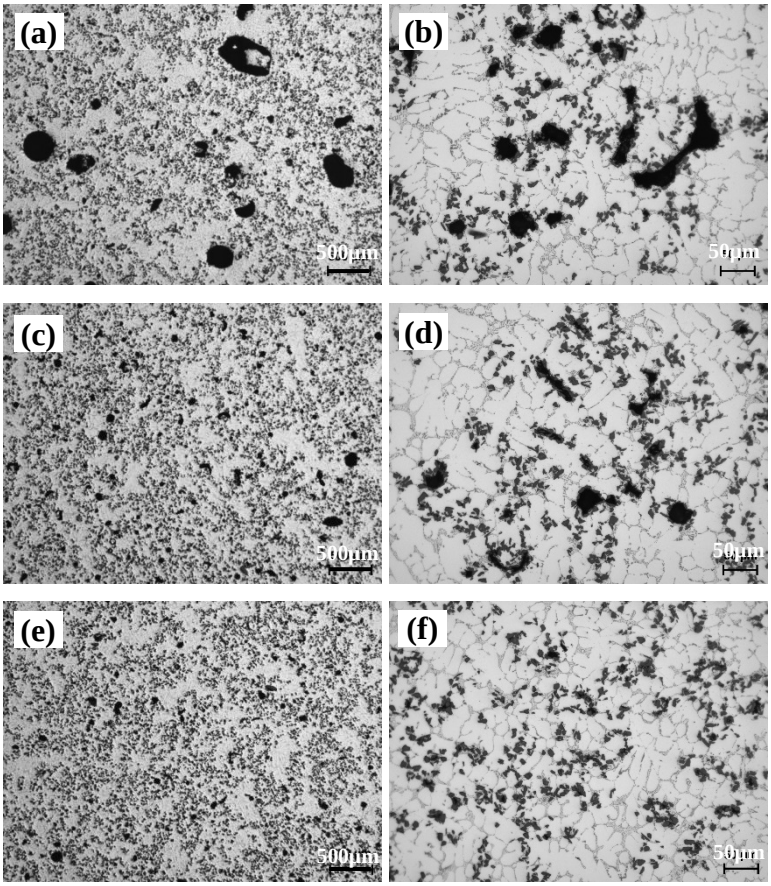

Figure 4.2 Microstructure of A356/12SiC_p composites fabricated by impeller stirring (IS) (a) and (b), impeller stirring and high shear treatment at 650°C (IS+HS) (c) and (d), and impeller stirring and high shear treatment at 730°C (IS+HS) (e) and (f). All samples were prepared with an Φ 40 mm steel mould.

Figure 4.2 shows the reinforcement distribution in A356/12wt%SiC_p composites with different fabrication routes and parameters. Large pores and particle-free matrix was found in IS route at 600°C and then cast at 750°C (**Fig. 4.2**(a)). With the high shear treatment (IS+HS), the size of individual porosities reduced dramatically (**Fig. 4.2**(c) and (e)).

Additionally, the areas of particle-free matrix reduced with a more uniform distribution of SiC particles in the microstructure. Comparing the IS+HS routes with different high shear temperatures, a further improvement of SiC distribution was obtained by processing

at 730°C with the dispersed SiC particles occupying more matrix area, reduction in the size of individual particle-free area and the reduced porosity size.

Similar reinforcement distribution was observed in A356/17wt%SiC_p composites (**Fig. 4.3**). With IS route, target addition of SiC particles was achieved, but large amount of porosity was observed (**Fig. 4.3**(a)). IS+HS process improved the local distribution of reinforcing particles which is illustrated by the minimised particle-free matrix. With increased processing temperature of IS+HS to 730°C, improved reinforcement distribution was obtained globally and locally (**Fig. 4.3**(e)).

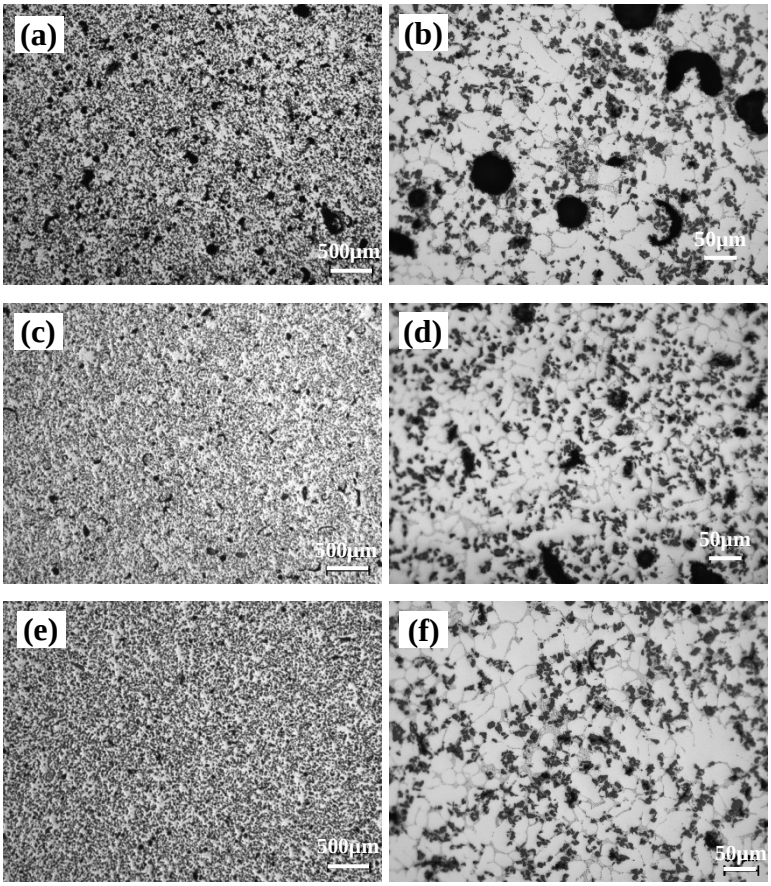

Figure 4.3 Microstructure of A356/17SiC_p composites fabricated by impeller stirring (IS) (a) and (b), impeller stirring and high shear treatment at 650°C (IS+HS) (c) and (d), and impeller stirring and high shear treatment at 730°C (IS+HS) (e) and (f). All the sample were prepared with an Φ 40 mm steel mould.

The results of A356/SiC_p composites fabricated with different routes suggest that the SiC particle distribution was influenced by the intensive convection of the composite slurry created from high shear treatment. It breaks down the agglomerates to small clusters or discrete particles leading to a reduction of particle-free matrix as the dispersed particles are able to occupy a larger area in the A356 matrix under a given solidification condition. In the rotor stator device, the melt undergoes a two-stage treatment. Within the stator, the rotor rotates at a predetermined speed and breaks down the particle agglomerations by

shear stress generated between rotor and stator. The shear stress (τ) can be estimated with the following equation (Atiemo-Obeng, Calabrese 2004):

$$\tau = \eta \frac{\pi N D}{\delta} \tag{4.1}$$

where η is the dynamic viscosity of composite melt, N is the rotating speed of the rotor head, D is the diameter of rotor head and δ is the gap between the rotor head and the inside surface of the stator. The viscosity η of A356/SiC_p slurry can be calculated by equation (Guth, Simha 1936):

$$\eta = \eta_0 \left(1 + \frac{5}{2}\varphi + \frac{109}{14}\varphi^2\right) \tag{4.2}$$

where η_0 is the dynamic viscosity of liquid phase, φ is the volume fraction of solid particles. Here for liquid A356, η_0 is about 1.045×10^{-3} Pa·s (Wang, Overfelt 2002). For the high shear mixing process, rotation speed is 5000 rpm. Combining Eq. (1) and (2) together, the minimum shear stress on the composite melt for 5 wt% SiC_p was calculated to be 421 Pa.

According to the Rumpf's model (Rumpf 1962), the tensile strength T of an agglomeration containing SiC particles is estimated with the following equation:

$$T = \frac{9}{32}\frac{\varphi}{\pi a^2} n_b F \tag{4.3}$$

where φ is the volume fraction of reinforcing particles with the radius of a, F is the average binding force of a single bond and n_b is the average number of bonds per particle (in nonHS sample of present study, $n_b$is 6 in average). Considering the particle-particle cohesive force from 5 nN to 15 nN, for different ceramic particles of similar size as in this study (Jones et al. 2003), the tensile strength of agglomerate is calculated to be in the range 6.5 ~ 19.5 Pa which is much lower than 421 Pa. The shear stress provided by rotor-stator device is significantly higher than the strength for holding SiC agglomeration and can effectively break down the agglomerates. As the cluster tensile strength is inversely proportional to the square of particle size ($T \propto \frac{F}{a^2}$), the smaller the particle size, the higher the strength of a cluster. As the SiC particle size of reinforcement decreases, increased rotation speed of the rotor in the rotor-stator device is desirable to ensure a good dispersion of SiC_p.

At the same time, the high speed turbulent flow increases the contact between the particles and the melt and improves wetting between the alloy melt and the reinforcing particles, leading to a uniform dispersion of SiC_p within the A356 alloy melt. A special feature of the rotor stator device is the provision of apertures evenly distributed at the bottom part of the stator, through which the well mixed slurry is forced out. At this stage, the composite slurry undergoes the high shear stress due to the nature of the friction generated from the viscous effect on the aperture wall through fluid squeezing and jetting out by high speed rotating rotor impeller. Once the slurry is forced into the stator aperture, the slurry flow velocity decreases dramatically at the inner wall surface of aperture where the fluid dynamics change. As a consequence large velocity gradient built up from the boundary layer close to the inner wall surface of the aperture to the centre of aperture hole where the shear stress applied on the composite slurry. The shear stress (τ) on the composite slurry through stator aperture is presented by the equation (Douglas et al. 2011),

$$\tau = f\rho\vartheta^2/2 \tag{4.4}$$

where f is the flow friction factor which is 0.03 for turbulent in steel pipe (the Moody chart (Douglas et al. 2011)), ρ is fluid density and ϑ is the mean flow velocity. The theoretical density of A356/5SiC slurry is 2.711 g/cm^3 which calculated with the rule of mixture and approximate flow velocity of slurry in similar rotor-stator mixer geometry and parameters is 10 m/s (Utomo et al. 2009). The shear stress experienced by the composite slurry passing through a single stator aperture is calculated to be 4.1×10^3 Pa which further contributes to the particle dispersion by breaking up the particle agglomerations inside the apertures.

4.1.2. SiC Uniformity of Composite Slurry in Large Volume

The settling of reinforcing particles in composite slurry due to the density differences during the fabrication process is recognised as one of the factors influencing the global distribution of reinforcement in large scale preparation of MMCs. **Figure 4.4** shows the microstructures of A356/17SiC_p composite cast from different heights of 7 kg slurry with varying moulds. In combination with **Figure 4.5**, it shows a similar SiC content close to 17wt% (15.5% in volume) at different height which suggests that the settlement of SiC was avoided by the intensive shearing from rotor-stator mixer. Although the distribution of particle-free area and porosity morphology are different, this could be related to the

different cooling rates of the moulds. The uniform SiC particles distribution in 7 kg slurry suggests that shear region of rotor-stator mixer is capable of covering large amount of melt with sufficiently intensive shearing on the reinforcement agglomerate to break it down.

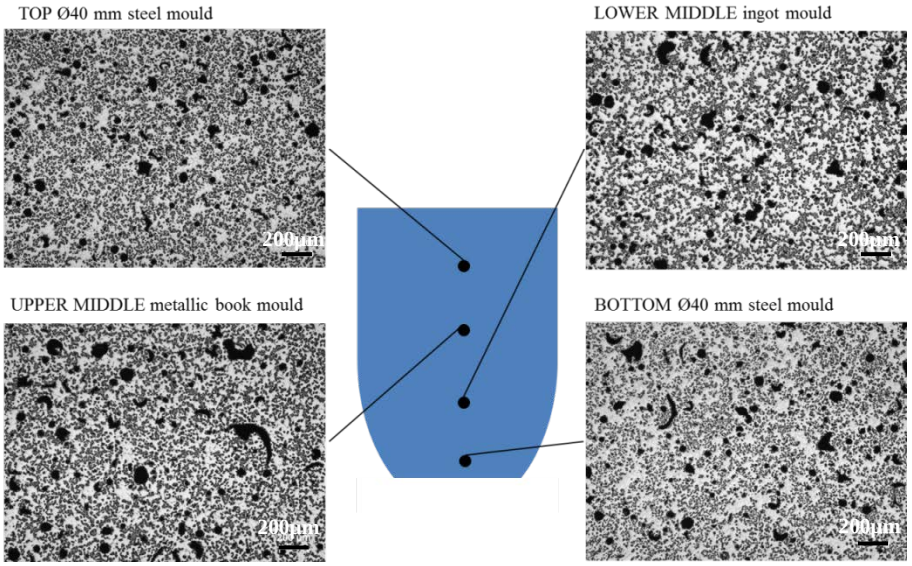

Figure 4.4 SiC_p distributions of different melt positions within the crucible of 7 kg A356/17SiC_p composite fabricated with high shear treatment at 650°C.

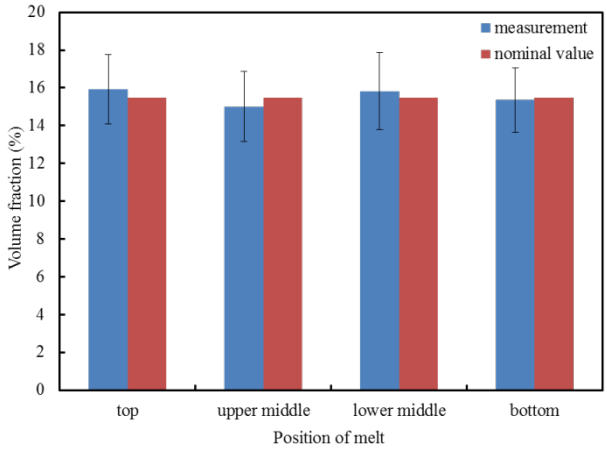

Figure 4.5 Measured volume fraction of SiC by grey contrast method in different positions of 7 kg A356/17wt%SiC_p composite fabricated with high shear treatment at 650°C (due to the density difference between SiC and A356 alloy, 17 wt% SiC in A356 alloy equivalent to 15.5 vol% in volume fraction. Density of liquid A356 alloy is 2.45 g/cm^3, and density of SiC is 3.21 g.cm^3).

4.1.3. Porosity

The effect of high shear treatment on porosity reduction was observed in the microstructure in section **4.1.1**. The quantified analysis of density of A356/SiC_p composites in **Figure 4.6**, show that the measured densities are closer to calculated theoretical values using the rule of mixture (in dash line) with the high shear treatment

compared with only mechanically stirred sample. The difference between the measured density and the corresponding theoretical value is attributed to the porosity which lowers the density of composite samples. Processing with high treatment temperature achieves a higher density closer to the calculated density. These observations are consistent with the previous microstructural observation.

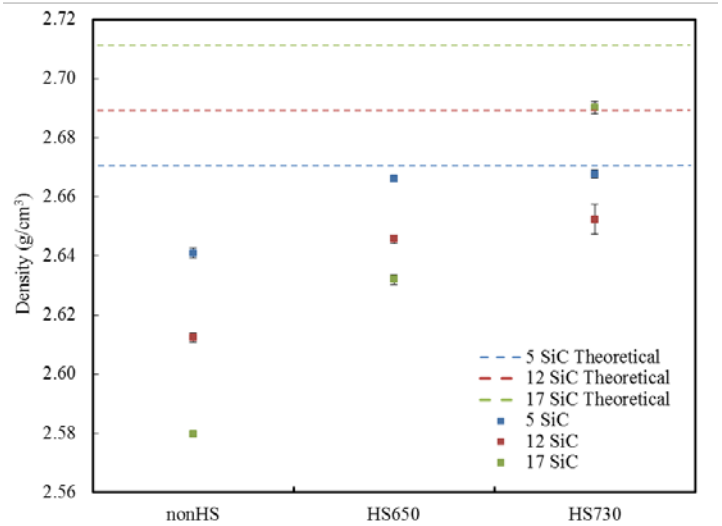

Figure 4.6 The measured density of A356/SiC_p composites fabricated with and without high shear treatment and cast with Φ 40 mm steel mould.

The SEM image in **Figure 4.7** reveals that two types of porosity morphology were observed. The first type of porosity (**Fig. 4.7**(a) and (b)) was in large scale with SiC particles on the wall of pore and air trapped inside. This is initially caused by the gas entrapment (Hashim et al. 2002a) during mechanical stirring as the reinforcing particles as well as air bubbles are introduced into the melt by the vortex created from rotating impeller. Oxide films have lower interfacial energy with ceramic particles compared with Al melt, so the SiC particles tend to adhere to the wall of gas bubbles (**Fig. 4.8**(a)). Then the bubbles with attached reinforcing particles trap inside the composite during the solidification as the viscosity of composite slurry overcomes the floating force of gas bubble. The squeezed shape of porosity shown in **Figure 4.7**(a) is due to the stress applied during solidification of the matrix. The second type of porosity is shown in **Figure 4.7**(c). The reduced size and spherical morphology distinguished these from the first type. The formation of this type of porosity is schematically illustrated in **Figure 4.8**(b).

Based on the microstructural observations, the mechanisms of defect formation are proposed. The pores are caused by the loose SiC agglomerate with gas in the gaps of the

particle surface. During the solidification of A356/SiC_p slurry, it remained in the composite. Due to the metallurgical sample preparation, the loosely contacted ceramic particles in the centre of agglomerate fall out during polishing and leave the out layer of SiC particles visible under OM and SEM observation. Strictly speaking, the second type of porosity was in characteristic of agglomerate as the empty area inside pores was filled with reinforcing particles in the as-cast state without sample preparation.

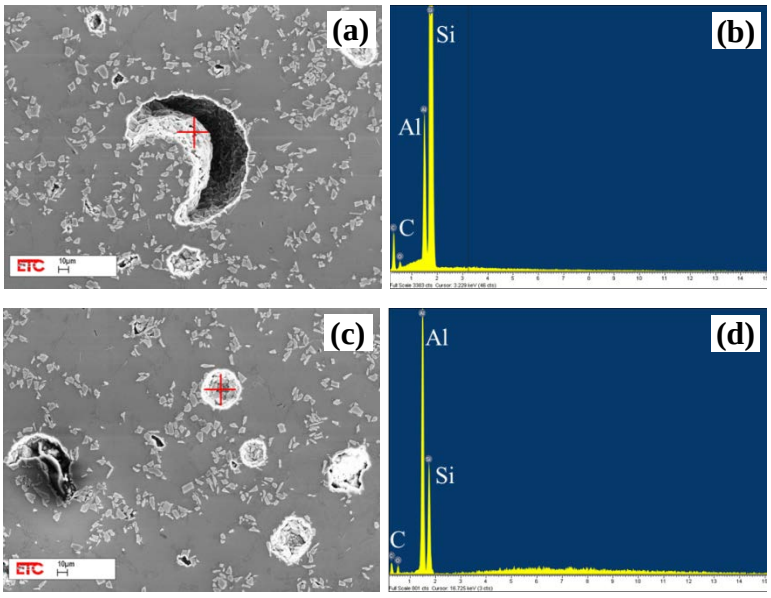

Figure 4.7 Typical morphology of porosity in A356/17SiC_p composite fabricated without high shear treatment and cast with Φ 40 mm steel mould, (a) the porosity formed due to the gas entrapment and the EDS result of wall of porosity (b), and (c) the porosity of SiC agglomeration and the EDS result of consistence of porosity.

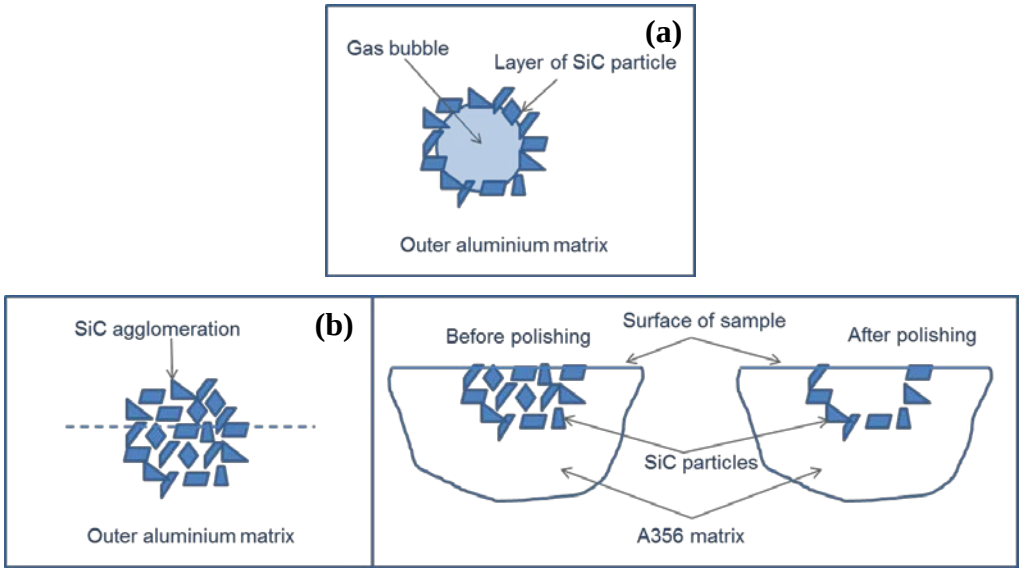

Figure 4.8 Schematics of porosity formation mechanisms related to the porosity morphology A356/SiC composites, (a) gas porosity and (b) SiC agglomeration.

4.1.4. Elastic Modulus

Figure 4.9 shows the measured elastic modulus of A356/SiC_p composites fabricated with different process route and parameters. Improved elastic modulus was observed in the high shear treated sample compared with only mechanical stirred sample. In general, the volume fraction of reinforcement is the dominant factor that controls the elastic modulus (**Fig. 4.9)**. However, at similar volume fraction of reinforcement, spatial distribution of particles and defects content significantly influence the elastic modulus (Lloyd 1994). Non-uniform distribution of the reinforcement leads to the non-uniform stress distribution and can cause the reduction in the modulus. The defects affect the integrity of bulk material and influence the reflection of stress on the strain status which also worsens the rigidity of the metallic material (Kumar et al. 2011).

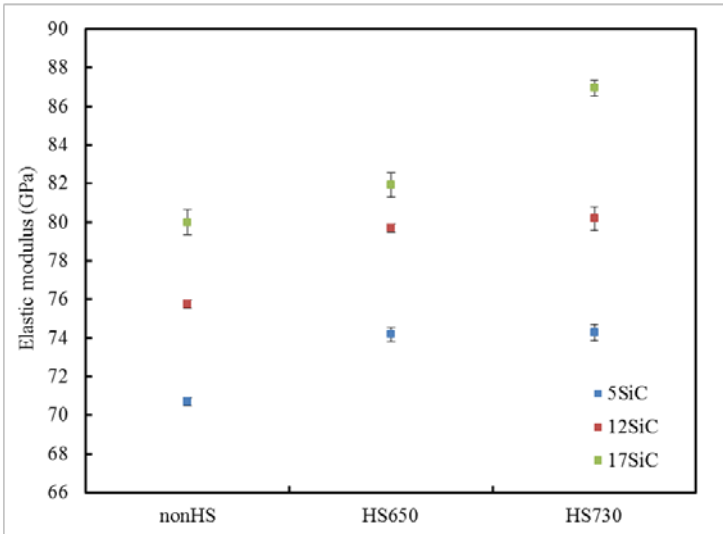

Figure 4.9 The measured Elastic modulus of A356/SiC_p composites fabricated with and without high shear treatment and cast with Φ 40 mm steel mould.

4.1.5. Brinell Hardness

Figure 4.10 shows the Brinell hardness value of A356/SiC_p composites fabricated with different process routes and parameters. An improvement of Brinell hardness is observed in the high shear treated sample compared with only mechanical stirred sample. With the higher processing temperature of high shear treatment, the Brinell hardness increased. This is related to the defects elimination of rotor-stator mixer on the breaking down the porosity and agglomerates. Experimental observations indicated that the reduction in porosity volume fraction, individual agglomerate size and particle-free matrix area were

obtained with high shear treatment at 730°C with various SiC additions compared with samples processed at a lower processing temperature or without high shear treatment.

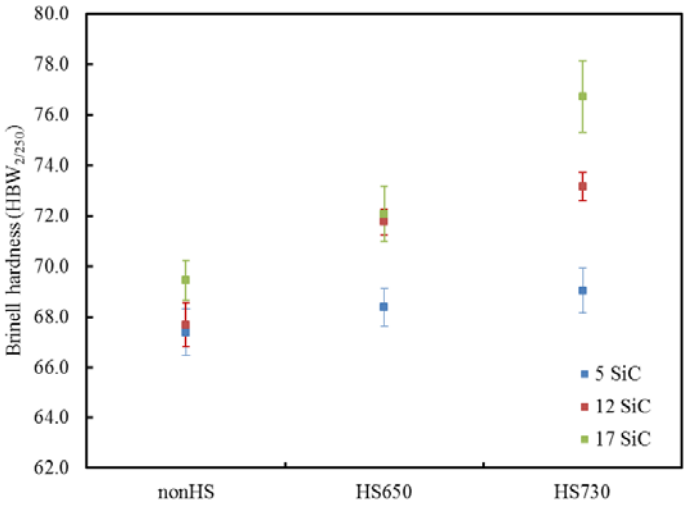

Figure 4.10 The measured Brinell hardness of A356/SiC_p composites fabricated with and without high shear treatment and cast with Φ 40 mm steel mould.

4.2. The Effect of Particle Content on Aluminium Matrix Composites

The A356/SiC_p composites with different particle additions fabricated with and without high shear treatment were examined using the microstructure, defect distribution and mechanical properties. The objective of this part of the research is to investigate the effect of SiC addition on the particle distribution of high sheared and non-high sheared Al-MMCs.

4.2.1. Reinforcement Distribution

The optical microstructure of A356/SiCp composites prepared with mechanical stirring is shown in **Figure 4.11**. The presence of porosity and SiC agglomerates was observed in the micrographs from 5wt% to 17 wt% reinforcing particle addition. With the increase in SiC particle content, the number density of pores in the composite samples tends to increase but the size of the pores remain relatively constant. The SiC particles and agglomerates are distributed in the eutectic Al-Si area of A356 matrix with similar α-Al dendritic arm spacing.

During the mechanical stirring process, the SiC particles were drawn into the melt by the vortex generated from rotating impeller. The shear force provided by the impeller rotation

helps to introduce reinforcing particles into the melt and also breaks down the agglomerates of bulk cohesive SiC powder.

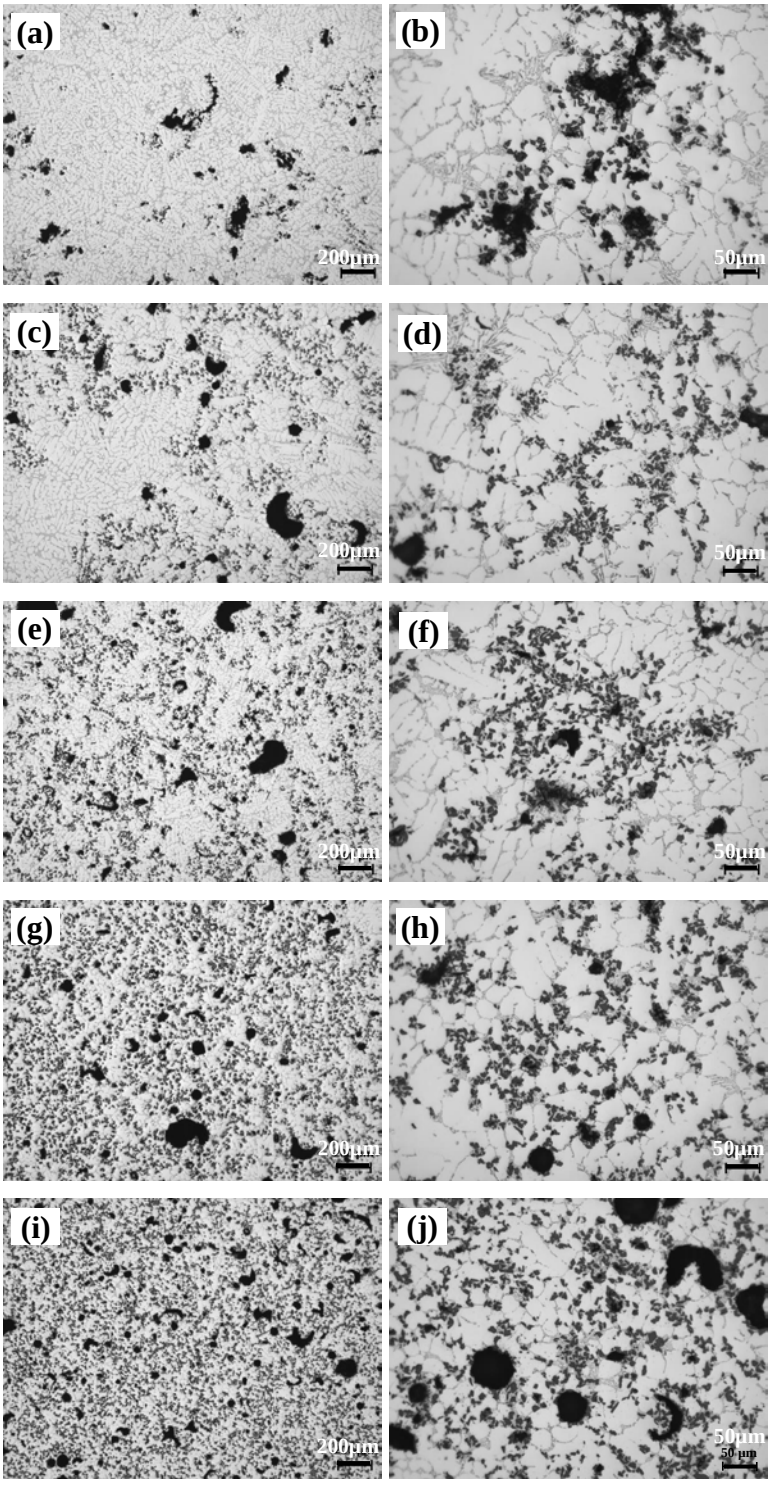

Figure 4.11 The microstructure of A356/SiC_p composites fabricated with different SiC content without high shear treatment and cast at 750°C with Φ 40 mm steel mould, (a) and (b) 5%SiC, (c) and (d) 10%SiC, (e) and (f) 12%SiC, (g) and (h) 15%SiC, and (i) and (j) 17%SiC.

The maximum force on a particle cluster in a shear flow of impeller stirring can be expressed as (Nienow et al. 1997):

$$F = 6\pi\eta\alpha^2\dot{\gamma} \tag{4.5}$$

where α is the radius of each primary particle in the cluster, η is the dynamic viscosity and $\dot{\gamma}$ is the shear rate in the surrounding liquid medium.

The degree of mixing is effected by the viscosity of melt flow when the shear rate and particle condition are constant in the process. According to the equation 4.2, the dynamic viscosity $\eta \propto \varphi$. With the increase in SiC addition, the dynamic viscosity of A356/SiC_p composite slurry increase as well. The increase in dynamic viscosity lead to the increased shear force on the impeller and consequently reduce the size of SiC agglomerates in A356/17wt%SiC composite in comparison to the sample with 5 wt% addition.

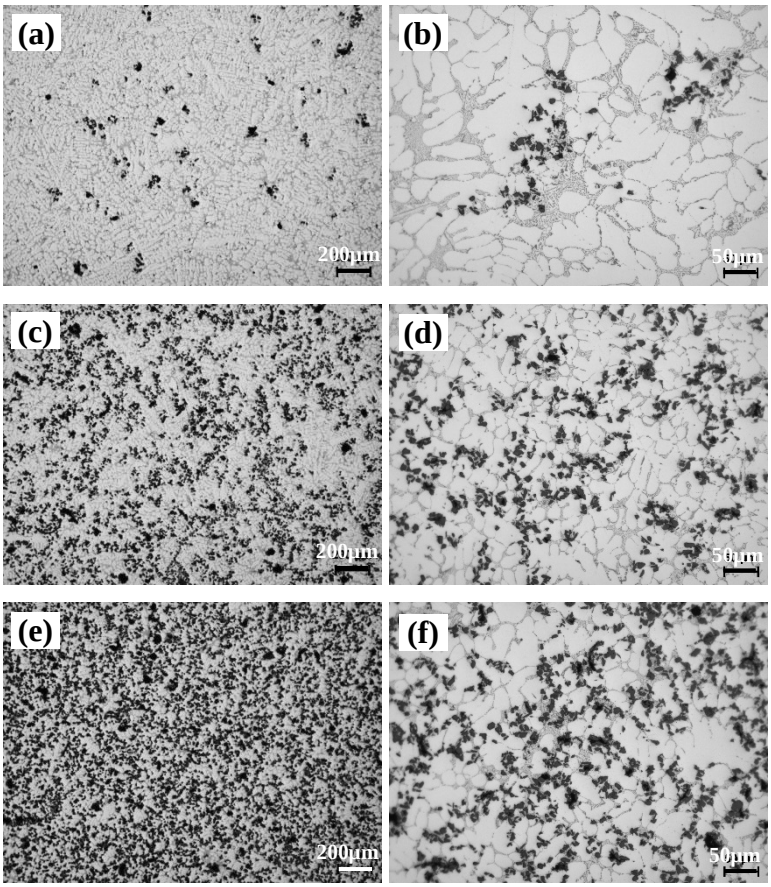

Figure 4.12 The microstructure of A356/SiC_p composites fabricated with different SiC content with high shear treatment at 730°C and cast with Φ 40 mm steel mould, (a) and (b) 5%SiC, (c) and (d) 12%SiC, and (e) and (f) 17%SiC.

Figure 4.12 shows the microstructure of A356/SiC_p composites with SiC addition of 5wt%, 12wt% and 17 wt% by mechanical stirring and high shear treatment (IS+HS). Large pores have disappeared with reduced size of SiC agglomerates. Compared with

associated non-high sheared sample, the global distribution and local particle dispersion are all improved. The high magnification images (**Fig. 4.12**(b), (d) and (f)), show that discrete SiC particles occupied the Al-Si eutectic network which indicated the good wettability of matrix melt on the SiC particles. This is due to the particle cluster break-up and particle surface flushing through the two stage intensive shearing of composite slurry in the gap of rotor-stator and apertures on the stator wall as discussed in the previous section.

4.2.2. Porosity

The calculation of porosity is based on the difference between theoretical and measured density of composites with different SiC addition and fabrication routes. The relationship of porosity with theoretical and measured density of composites can be expressed as:

$$\rho_T = \frac{m_c}{V_c} \tag{4.6}$$

and

$$\rho_M = \frac{m_c}{V_c + V_p} \tag{4.7}$$

Combining (4.6) and (4.7), the volume fraction of porosity in the composite sample can be expressed as:

$$\frac{V_p}{V_c + V_p} = \frac{\rho_T - \rho_M}{\rho_T} \tag{4.8}$$

where ρ_T is the theoretically calculated density, ρ_M is the experimentally measured density of composites; V_c is the theoretical volume of composite, V_p is the volume of porosity entrapped in the composite and m_c is the mass of composite.

The measured and calculated density of A356/SiC_p composites fabricated with and without high shear treatment is shown in **Figure 4.13**. The plots indicates the theoretically calculated density of composite with the rule of mixture. The solid red line indicates the density of composites without high shear treatment and solid blue line indicates the composite density with high shear treatment. The dashed red line shows the porosity of composite samples without high shear treatment and dashed blue line presents the porosity of high shear treated A356/SiC_p composites. The theoretical density of

composites increases with the increasing SiC addition as the SiC is denser than the matrix Al-Si alloy. The sample with high shear treatment shows the similar tendency for the measured density with particle content. Limited density deviation of A356/SiC_p composites with high shear is observed in comparison with the grey and blue plots.

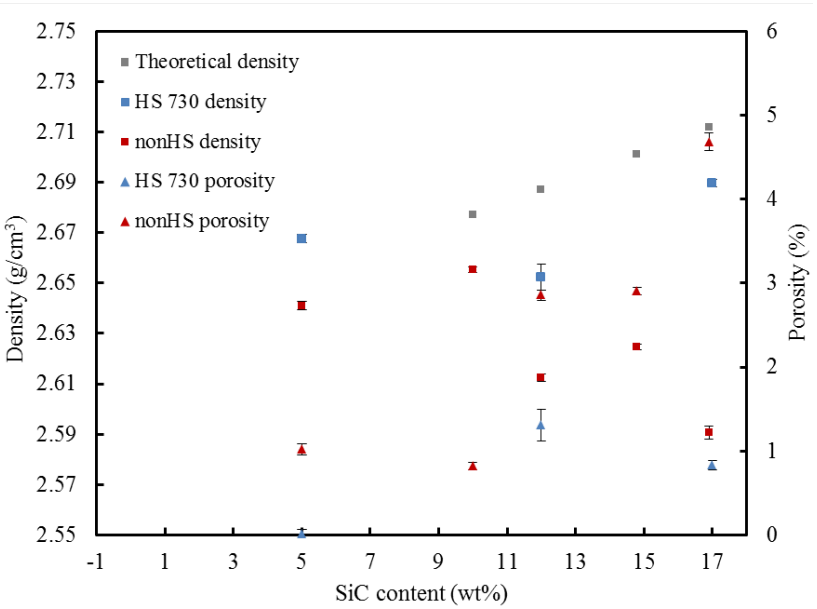

Figure 4.13 The measured and calculated density of A356/SiC_p composites fabricated with and without high shear treatment for different SiC contents, cast with Φ 40 mm steel mould.

In contrast, the non-high shear treated composite shows a decreased density with the increased SiC addition. Higher the SiC_p content, larger the deviation of density compared with the theoretical value. This is significantly influenced by the level of porosity inside the composite samples. In general, the gas entrapment in composite slurry during fabrication is highly related to the amount of powder addition and duration of vortex, the more powder is added into melt and longer the of vortex time for introducing powder, the higher content of porosity. As the mechanical stirring time was strictly controlled to 5 minutes, the high porosity level in non-high sheared A356/17SiC_p composite is mainly caused by the higher content of SiC powder compared with the other composite samples without high shear treatment.

4.2.3. Elastic Modulus

The Halpin-Tsai model (Lloyd 1994), which predicts the modulus of particle reinforced composites with the assumption of homogeneous reinforcement distribution in the matrix, is used to evaluate the elastic modulus of the A356/SiC_p composites fabricated with and

without high shear treatment. The elastic modulus of a composite is expressed as (Halpin 1984):

$$E_c = \frac{E_m(1+2sqV_p)}{1-qV_p} \tag{4.9}$$

where

$$q = \frac{(E_p/E_m-1)}{(E_p/E_m)+2s} \tag{4.10}$$

and E_c, E_m and E_p are the elastic modulus of the composite, matrix and particles, respectively, V_p is the volume fraction of particles, and s is the particle aspect ratio. Since SiC particle morphology used in this study is angular, s is measured to be between 1.5 and 3.

Figure 4.14 shows the comparison of elastic modulus prediction and experimental measurement for composite samples with and without high shear treatment. The area in between calculation with s =1.5 and s=3 (indicated with grey arrow) is the theoretical region predicted by Halpin-Tsai model. The measured Elastic modulus of composites with high shear treatment is presented in blue and the value of composites without high shear treatment is shown in red.

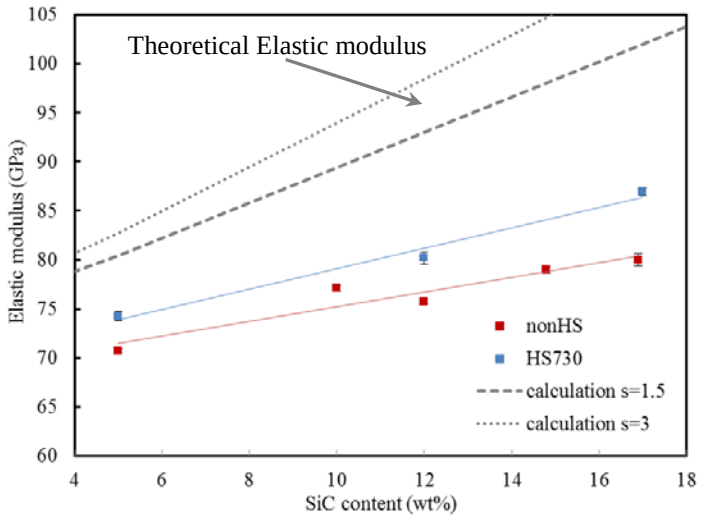

Figure 4.14 The measured Elastic modulus of A356/SiC_p composites fabricated with and without high shear treatment for different SiC contents and cast with Φ 40 mm steel mould.

The measured elastic moduli for the high sheared samples are closer to the lower limit of theoretical values, and in comparison, a given deviation was observed in the non-high sheared composites. However, the gap between measured value of Elastic modulus of high sheared samples and the theoretical value could be attributes to the acoustic

scattering of composites materials and the presence of porosity (Fowler et al.). Acoustic energy would be scattered from individual grains and/or interface of matrix and ceramic particles in the A356/SiC_p composites. Porosity can cause the similar effect as the continuity of materials has been affected which lead to acoustic scattering and reduce the accuracy of Elastic modulus measured by ultrasonic thickness gauge. The improvement of Elastic modulus value of high sheared samples compared with non-high sheared samples can be explained as improved reinforcing particle distribution and/or reduced porosity content, all indicate an improvement in continuity of composites. Further research is needed to confirm this.

In general, the volume fraction of reinforcement is the dominant factor that controls the elastic modulus. However, given the similar volume fractions, e.g. 5wt%, 12 wt% and 17 wt% SiC additions, spatial distribution of particles and material continuity significantly influence the elastic modulus. Non-uniform distribution of the reinforcement leads to a non-uniform stress distribution in the material and cause the reduction in the modulus (Wang et al. 1993). High content of porosity deteriorate the integrity of the bulk sample and influence of the reaction of strain to the applied stress.

4.2.4. Brinell Hardness

Figure 4.15 shows the measured Brinell hardness value of A356/SiC_p composites fabricated with different process route and parameters. A linear improvement of elastic modulus was observed in the high shear treated sample presented in blue compared with only mechanically stirred sample in red. With the high shear treatment, the Brinell hardness increased with the increased SiC content. On the contrary, the Brinell hardness of non-high sheared samples show a slight improvement with the increased reinforcing particle addition. This is affected by the high porosity content in the non-high sheared composites which reduced the resistance of the indenter pressure.

During the high shear treatment of the composite slurry, the intense flow convection forced the particle clusters and also the entrapped gas bubbles go through the rotor-stator mixer, thus particle clusters break up into discrete particles and gas bubbles tear and reduced. With similar SiC additions of 5 wt%, 12 wt% and 17 wt%, the difference between composites with high shear and without high shear became more significant with the increased reinforcing particle addition. This is related to the defects elimination effect

of rotor-stator mixer on the breaking down the porosity and agglomerates. Microstructure observation indicates that the reduced porosity volume fraction, individual agglomerate size and size of particle-free matrix area were achieved with high shear treatment compared with associated samples without such treatment.

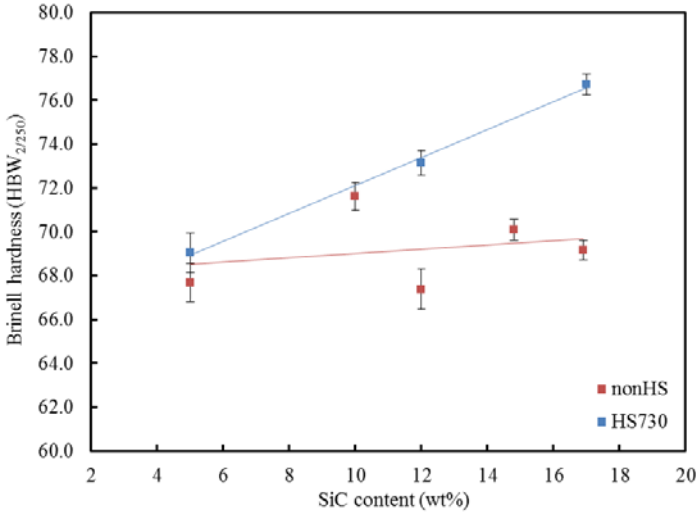

Figure 4.15 The measured Brinell hardness of A356/SiC_p composites fabricated with and without high shear treatment for different SiC contents, cast with Φ 40 mm steel mould.

4.3. The Effect of Cooling Rate on Aluminium Matrix Composites

Cooling rate, as a parameter influencing the solidification behaviour of alloy melt or composite slurry (Lloyd 1989), determines the microstructure evolution once the melt flow into casting mould. The high shear treatment aimed to improve the particle distribution in the pre-casting stage by the melt treatment to distribute the particle clusters and agglomerates. The final distribution of reinforcing particles was also determined by the casting parameters controlling the solidification process. As the pouring temperature and mould temperature are controlled at 750°C and 200°C, respectively, the cooling rate is the only variable that influences the final distribution of SiC particles. The objective of this part of my research is to investigate the effect of cooling rate on the particle distribution during the solidification of high shear treated Al-MMCs.

4.3.1. Reinforcement Distribution

Figure 4.16 shows the SiC particle distribution of A356/17SiC_p composite fabricated with mechanical stirring and high shear treatment but cast into different moulds with different cooling rates.

The coarse α-Al dendrites were observed in **Figure 4.16**(a) and (b) with the cooling rate of 0.26 K/s during the solidification in the insulation board book mould. The low cooling-rate favours the formation of large dendrites. Together with later solidification of Al-Si eutectic, the SiC particles were rejected by the growing α-Al dendrites and crowded into inter-dendritic regions. On the contrary, the steel book mould shares the same design with insulation board book mould but the cooling rate is higher (91.85 K/s). The solidification of composite slurry in this mould leads to enhanced nucleation of α-Al, the growth of dendrite giving rise to the reduction of SiC particles agglomeration during the microstructure evolution. An improved global and local distribution is observed in **Figure 4.16**(e) and (f), particles are disconnected and individually distributed in the network of Al-Si eutectic.

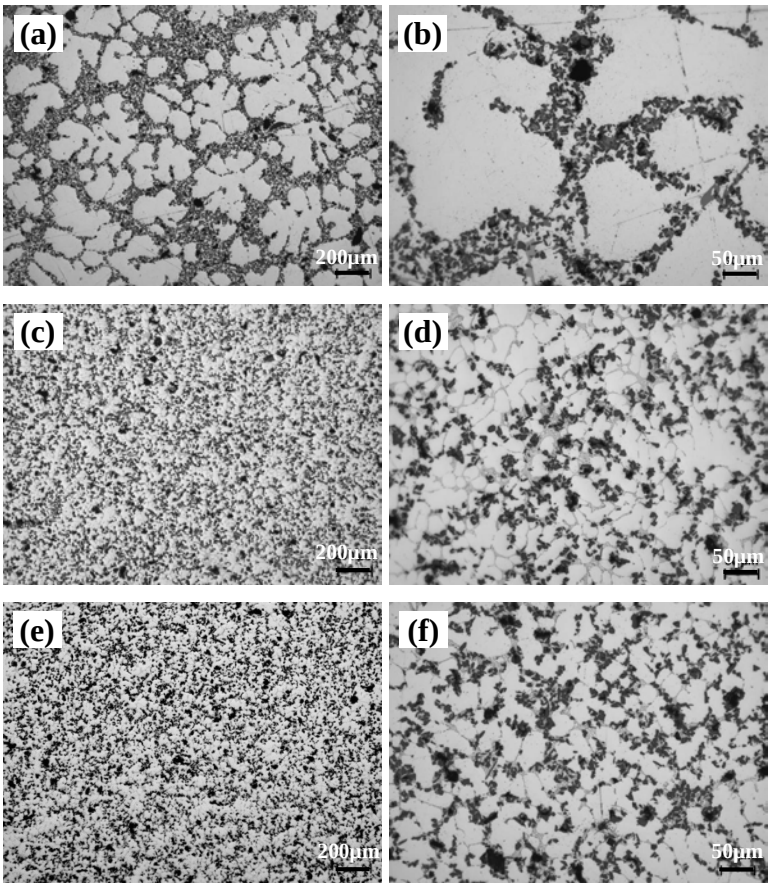

Figure 4.16 Microstructure of A356/17SiC$_p$ composites fabricated by insulation board book mould (0.26 K/s) (a) and (b), Φ 40 mm cylinder steel mould (30.14 K/s) (c) and (d), and metallic book mould (91.85 K/s) (e) and (f) with high shear treatment at 730°C.

The cooling rates of these three different moulds were calculated from measured cooling curves with A356/17SiC$_p$ composite slurry. The thermal couple were placed in the position similar to the positions of sample for metallographic preparation (in section

3.3.1). The composite slurry was poured at 750°C and the cooling curve was recorded from pouring temperature to the liquidus of A356 alloy. The slope of linear region of cooling curve above the liquidus of A356 alloy was used to calculate cooling rate of each mould. Thus high cooling rate retains the distribution of reinforcing particles in the liquid matrix and enhances the effect of high shear treatment on the particle dispersion.

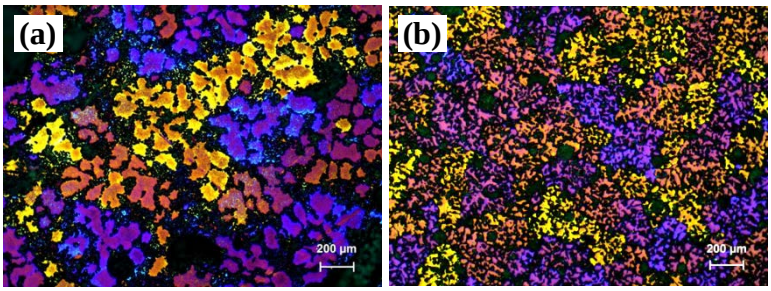

Figure 4.17 Microstructure of A356/17SiC$_p$ composite fabricated by insulation board book mould (0.26°C/s) (a) and metallic book mould (91.85°C/s) (b) with high shear treatment at 730°C under polarized light.

The polarised micrographs of A356/17SiC$_p$ composite in **Figure 4.17**, show a reduced grain size for α-Al phase for a high cooling rate of 91.85 K/s compared with the microstructure of composite solidified at 0.26 K/s. The higher cooling rate provides sufficient under cooling for more nucleation sites to be activated, and thus increases the number density of nuclei resulting in a refined microstructure.

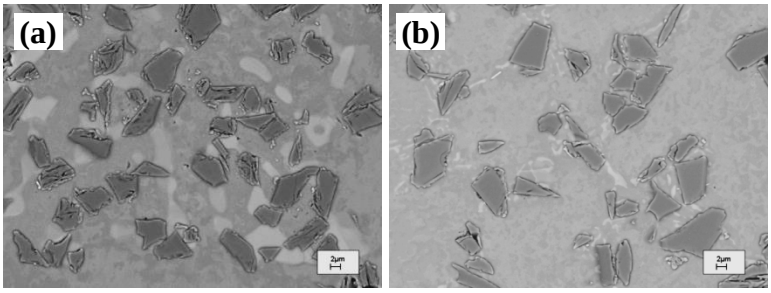

Figure 4.18 SEM image of A356/17SiC$_p$ composites fabricated by insulation board book mould (0.26°C/s) (a) and metallic book mould (91.85°C/s) (b) with high shear treatment at 730°C under BSE signal.

Figure 4.18 is the SEM image of the SiC particles in the Al-Si eutectic area with different cooling rates. In the low cooling rate condition, the SiC particles have more connections with neighbouring particles in the coarse eutectic area. However, with the high cooling rate, the size of the eutectic Si is reduced and SiC particles are more separated from each other reducing the contact between the neighbouring particles. These observations of composites microstructure suggest that the high cooling rate helps to retain the good particles distribution achieved by the high shear treatment in the liquid state. With the

reduced cooling rate, the reinforcing particles tend to be pushed out by the solidification front of primary phase and crowded in the inter-dendritic area.

4.3.2. Porosity

The porosity of A356/17SiC$_p$ composite cast in different moulds was examined and the results are shown in **Figure 4.19**. With increased cooling rate, the porosity increased slightly. The dominant factor that influences the porosity volume fraction is the high shear treatment. As the melt was treated by the same process, the samples cast with varying cooling rates show similar measured density.

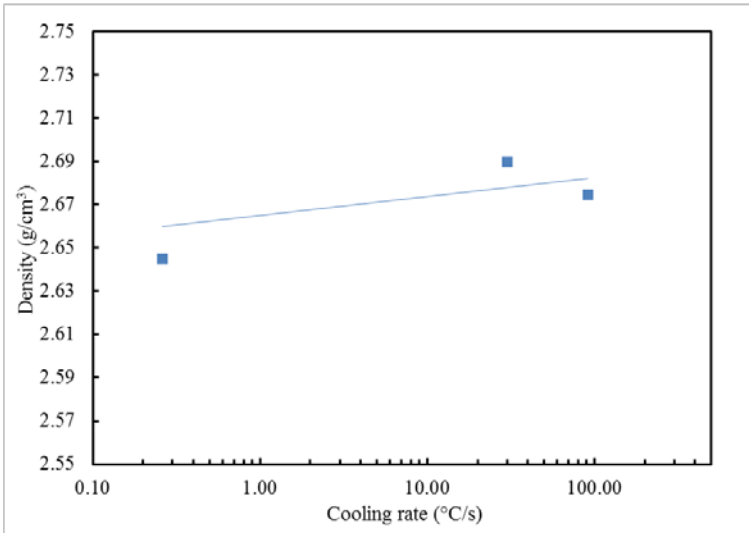

Figure 4.19 The measured and calculated density of A356/17SiC$_p$ composites fabricated with high shear treatment at 730°C and solidified under different cooling rates.

4.3.3. Elastic Modulus

Figure 4.20 shows the Elastic modulus of the high shear treated composite slurry cast in different moulds. The value of measured Elastic modulus of A356/17SiC$_p$ composites increased slightly with the increase in cooling rate.

This subtle difference could be related to the homogeneity of bulk material as the coarse α-Al dendrite may act differently in the test compared to the SiC particles occupied Al-Si eutectic. The composite cast at a cooling rate of 91.85 K/s forms a more homogeneous bulk structure with a uniform reinforcing particle distribution.

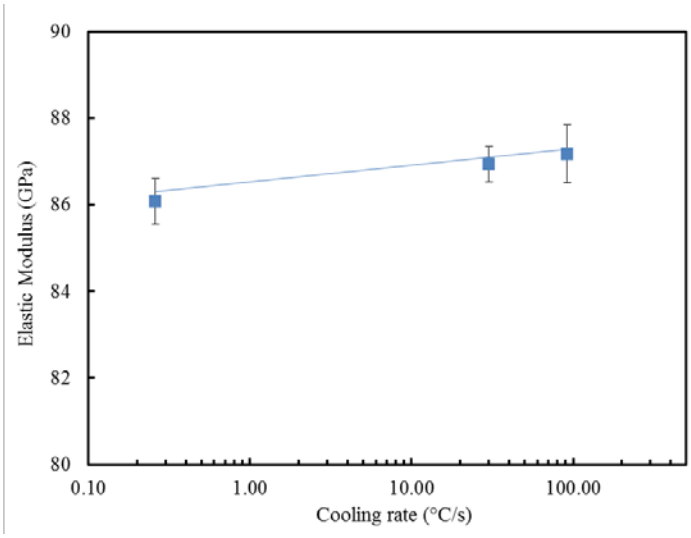

Figure 4.20 The measured Elastic Modulus of A356/17SiC$_p$ composites fabricated with high shear treatment at 730°C and solidified under different cooling rates.

4.3.4. Brinell Hardness

Figure 4.21 shows the Brinell hardness of high shear treated A356/17SiC$_p$ composite cast under different cooling rates. The value of Brinell hardness increased with increase in cooling rate from 65.91±1.06 HBW$_{5/250}$ to 79.63±2.43 HBW$_{5/250}$.

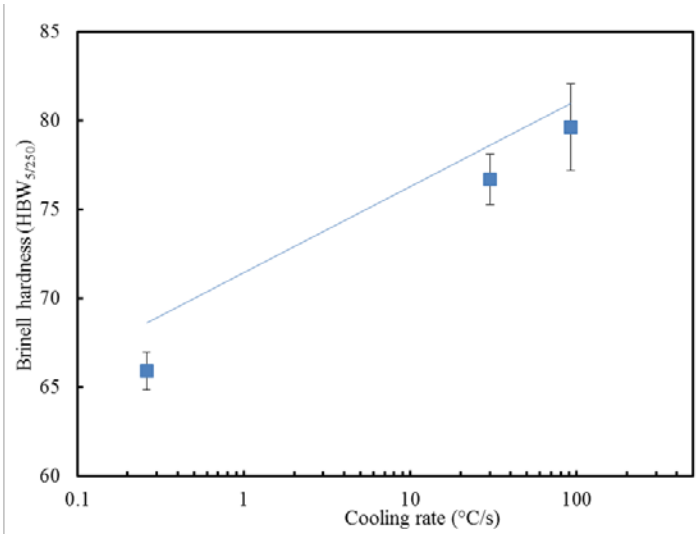

Figure 4.21 The measured Brinell hardness of A356/17SiC$_p$ composites fabricated with high shear treatment at 730°C and solidified under different cooling rates.

As the content of reinforcing particles is similar, the significant improvement of Brinell hardness can be attributed to the microstructural changes in the matrix. From the microstructure observation, the reduced α-Al dendrite size, refined α-Al grain and fine Al-Si eutectic network with small Si particles through the high cooling rate all contribute to Brinell hardness increase by material integrity and continuity improvement which

reinforce the resistance to indenter pressure and increase the hardness value (Dahle et al. 2005).

Chapter 5 Magnesium Matrix Composites and their Twin Roll Casting strip: Results and Discussion

5.1. The Effect of High Shear on Magnesium Matrix Composites Strip Fabrication

With the experimental conditions described in Chapter 3, AZ31/5wt%SiC_p slurry exhibited sufficient fluidity and the TRC process was conducted smoothly. The developments associated with the twin roll casting process will be discussed later in Chapter 6.

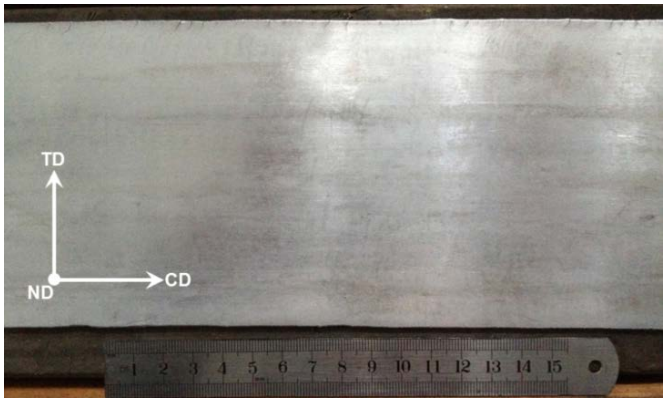

Figure 5.1 Photograph of AZ31/5SiC_p composite strip

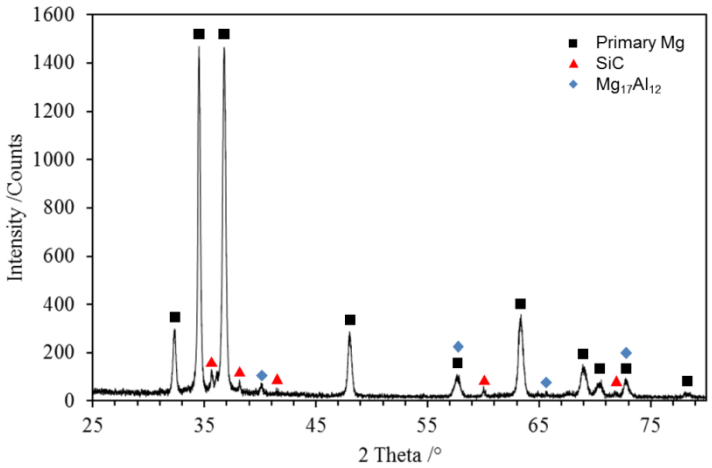

Figure 5.2 XRD pattern of TRC strip fabricated from high shear treated AZ31/5SiC_p slurry. The PDF numbers of primary Mg, SiC and $Mg_{17}Al_{12}$ are 01-077-6798, 01-075-8314 and 01-073-1148, respectively.

The strip thickness obtained was about ~1.7 mm, with limited variations along the strip width and length. The typical strip length with a uniform microstructure cast during

stabilized process parameters was about 3 m, which was used for further processing and analysis. The objective of this part of the research is to investigate the effect of high shear provided by the rotor-stator mixer on the particle distribution, microstructure evolution and mechanical property variation in Mg-MMCs TRC strip fabrication.

Figure 5.1 shows a macrograph of a typical AZ31/5wt%SiC_p composite strip. The surface finish is reasonably good, although there are some fine cracks at the edge of the strip. Microstructural examinations confirmed that there were no defects such as bleeding (Barekar, Dhindaw 2014) and cracking in the material apart from the fine cracks at the very edges of the strip. XRD analysis revealed that the constituents of the composite consisted mainly of α-Mg phase, SiC reinforcement and $Mg_{17}Al_{12}$ intermetallic phase, which corresponds to the peaks in the XRD spectrum in **Figure 5.2**.

5.1.1. Reinforcement Distribution

Figure 5.3 shows the optical micrographs obtained from both the TD and CD sections of both the HS and nonHS strips in the as-cast condition, in which SiC particles appear as the dark phase.

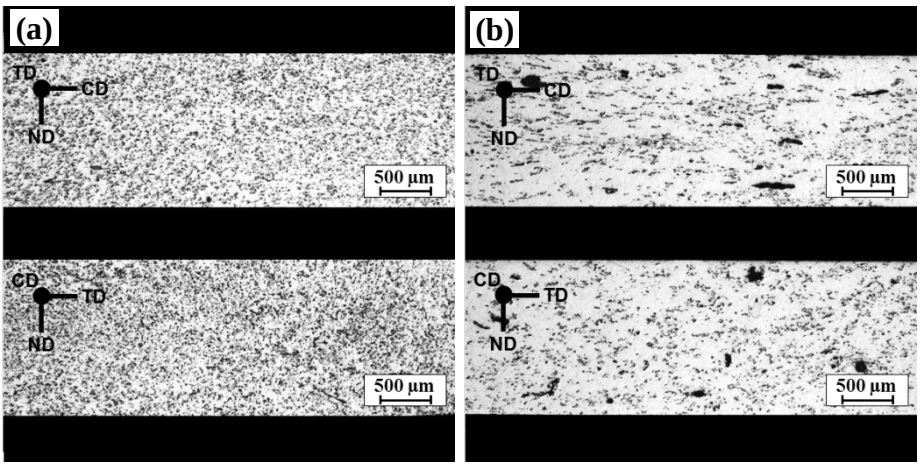

Figure 5.3 The longitudinal section and transverse section view of AZ31/5SiC_p composite TRC strip fabricated with high shear treatment (a), and without high shear treatment (b).

Figure 5.3(b) shows that the composite strip subjected to only mechanical stirring prior to TRC show severe particle agglomerations in the form of cluster of varied size and some with area of several hundred microns. The particle clusters elongated along the casting direction, corresponding to the material flow due to plastic deformation during TRC. Severe particle agglomeration resulted in large areas which are depleted of reinforcing

particles. On the other hand, the composite strip subjected to both mechanical stirring and high shear treatment display a globally uniform particle distribution within the matrix alloy with substantially reduced agglomerations. As shown in the **Figure 5.3**(a), the reinforcing SiC particles spread evenly over both the TD and CD planes throughout the strip thickness. Microstructure examination shows that such particle distribution features remain consistent over the full strip length obtained under steady state TRC.

A critical problem for the twin roll casting of Mg alloys and most other alloys is the formation of central line segregation consisting of solute rich phases, which is primarily due to the directional columnar growth of primary α-Mg phase from the surface towards the centre (Barekar, Dhindaw 2014). In the present work, no columnar structure was observed for both the HS and nonHS composite strips and variations in reinforcing particle volume fraction and of chemical compositions through the strip thickness were reduced in the HS strip. Previous studies on melt conditioned Mg alloys suggested that the high shear treatment provides homogeneous thermal and chemical fields, which results in a uniform distribution of potential nuclei, such as the magnesium oxide particles for the heterogeneous nucleation (Fan et al. 2009). The high shear treatment demonstrated the improvement of the size distribution of potential nuclei so that the nucleation efficiency was enhanced (Men et al. 2010a). The high shear treatment plays a similar role in improving the spatial and size distribution of heterogeneous nucleation sites. These sites can be magnesium oxide particles, which exist inevitably in the melt and the reinforcing ceramic SiC particles which can act as potent nucleation sites (Günther et al. 2006, Lelito et al. 2012).

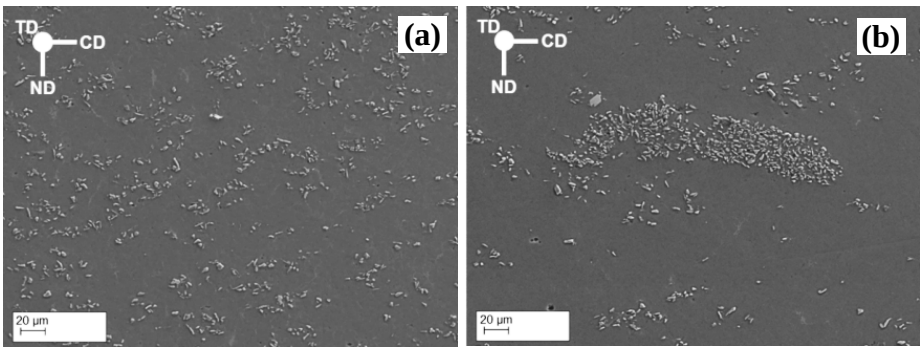

Figure 5.4 SEM image of longitudinal section view of AZ31/5SiC_p composite TRC strip fabricated with high shear treatment (a), and without high shear treatment (b).

At high magnifications in **Figure 5.4**, for the HS strip, individual SiC particles seems to disperse randomly and uniformly in the matrix, although some are still in clusters of a

few or at most over ten particles (**Fig. 5.4**(a)). In contrast, SiC particles in the nonHS strip are mainly agglomerated and the agglomeration contains hundreds to thousands of particles, leaving a large volume of the material free of SiC_p (**Fig. 5.4**(b)). This suggests that the high shear treatment effectively dispersed the reinforcing SiC particles and that the agglomeration of particles during TRC is avoided, due to the high cooling rate associated with the process.

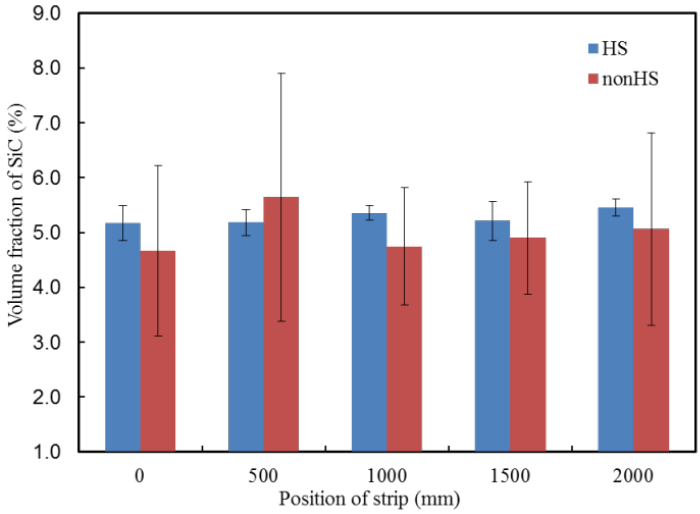

Figure 5.5 Spatial variation of the volume fraction of SiC particles in longitudinal section of AZ31/5SiCp composite TRC strip fabricated with high shear treatment (HS) and without high shear treatment (nonHS).

Figure 5.5 shows the variation in reinforcing particle volume faction along the strip length for both the HS and nonHS strips. The average particle volume fraction was 5.2% and 5.0% for HS and nonHS, respectively, which is very close to the nominal value of 5%. However, the large scale agglomeration of SiC particles in the nonHS strips led to large scatter in measured values through the strip thickness. The standard deviation of SiC particle volume fraction in the nonHS strip was around 6 times higher than that for the HS strip.

In order to evaluate the homogeneity of SiC particle distribution, Quadrat Method (Tzamtzis et al. 2009) was employed with 8×8 quadrat grid covering an area of 416 µm × 416 µm. More than 3500 SiC particles in 5 optical micrographs were counted for each sample. The Skewness β value (Lloyd 1994), expressed by following equation is used quantify the distribution of the reinforcing particles:

$$\beta = \frac{q}{(q-1)(q-2)} \sum \left[\frac{N_{qi} - N_q^{mean}}{\sigma} \right]^3 \quad (5.1)$$

where q is the total number of quadrats studied, N_{qi} is the number of SiC particles in the ith quadrat (i= 1, 2, ……, q), N_q^{mean} is the mean number of SiC particles per quadrat, and σ is the standard deviation of the N_q distribution. The lower the β value, the more uniform the distribution of the reinforcing particles. The calculated Skewness β value of HS strip (**Fig. 5.6**) is lower at each measured points than the nonHS strip. A good consistency in β value was also obtained along 2000 mm long HS strip, which indicates improved particle distribution homogeneity at both the microscopic and macroscopic scales in the HS composite strip.

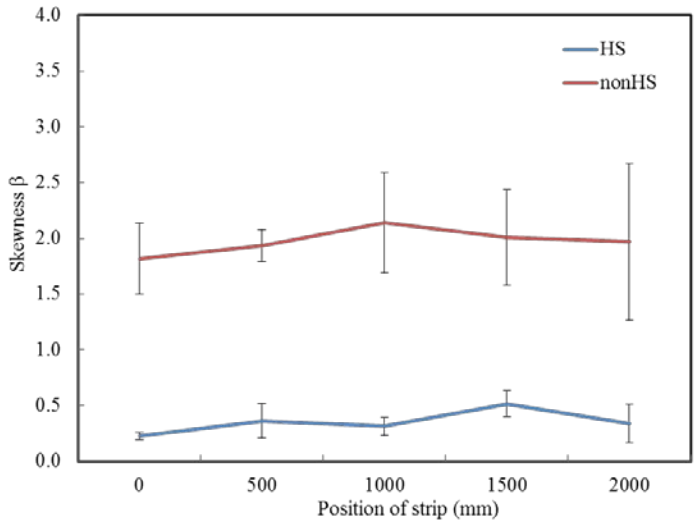

Figure 5.6 The distribution of reinforcing particles (Skewness β) determined by quadrat method in longitudinal section of AZ31/5SiC$_p$ composite TRC strip fabricated with high shear treatment (HS) and without high shear treatment (nonHS) at different positions along the strip.

In the two-stage mixing process shown in **Figure 3.12**, mechanical stirring with an impeller is responsible for the introduction of SiC particles into the melt with initial wetting and a globally uniform distribution. Effective wetting between the particles and the molten alloy is obtained via high shear treatment in the second stage of the mixing process. In the rotor stator device, the melt also undergoes two-stage treatment as the fabrication of A356/SiC$_p$ composites. The shear stress (τ) (Atiemo-Obeng, Calabrese 2004) generated between rotor and stator can be estimated with the following equation:

$$\tau = \eta \frac{\pi ND}{\delta} \tag{5.2}$$

where η is the dynamic viscosity of composite melt, N is the rotating speed of the rotor head, D is the diameter of rotor head and δ is the gap between the rotor head and the

inside surface of the stator. The viscosity η of AZ31/5wt%SiC_p slurry is calculated to be 1.41×10^{-3} Pa·s by Guth's model (Guth, Simha 1936). For the high shear mixing process, rotation speed of 5000 rpm was performed in the experiment. The shear stress on the composite melt is calculated to be 496 Pa. The tensile strength of SiC agglomerate is calculated to be in the range of 6.5 ~ 19.5 Pa which is less than 496 Pa in the previous chapter. The shear stress provided by rotor-stator device is significantly higher than the strength for holding SiC agglomeration and can effectively break down the agglomerates. As the cluster tensile strength is inversely proportional to the square of particle size ($T \propto \frac{F}{a^2}$), the smaller the particle size, the higher the strength of the cluster. As the SiC particle size of reinforcement decreases, increased rotation speed of the rotor in the rotor-stator device is desirable to ensure a good dispersion of SiC_p.

Once the composite slurry is forced into the apertures on the stator which are evenly distributed at the bottom part of the stator, it undergoes a high shear stress due to the nature of friction generated from the viscous effect on the aperture wall through fluid squeezing and jetting out by high speed rotating rotor impeller. The flow velocity of composites slurry decreases dramatically at the inner wall surface of aperture where the fluid dynamics change. As a consequence large velocity gradient built up from boundary layer closer to the inner wall surface of the aperture to the centre of aperture hole where the shear stress is applied on the composite slurry. The shear stress (τ) on the composite slurry through stator aperture is calculated to be 2.6×10^3 Pa by Douglas' model (Equation 4.4), a further particle dispersion is achieved inside the apertures.

5.1.2. Matrix Microstructure

Figure 5.7 shows the polarized light optical micrographs for both the HS and non HS composite strips, showing the difference in the primary α-Mg grain structures obtained from the different melt treatment schemes prior to TRC. The grain structure for the HS strip is uniform and fine with an average grain size of 39.3±14.9 μm. On the contrary, the nonHS strip shows an inhomogeneous grain structure with both coarse (above 100 μm) and fine grains of primary α-Mg phase, and the average grain size is 52.7±21.6 μm. The typical α-Mg grain size of majority of grains in the HS sample is in the range of 20 to 60 μm. For nonHS composites strip sample, grain size of the primary α-Mg phase can be 100 μm or more (**Fig. 5.8**).

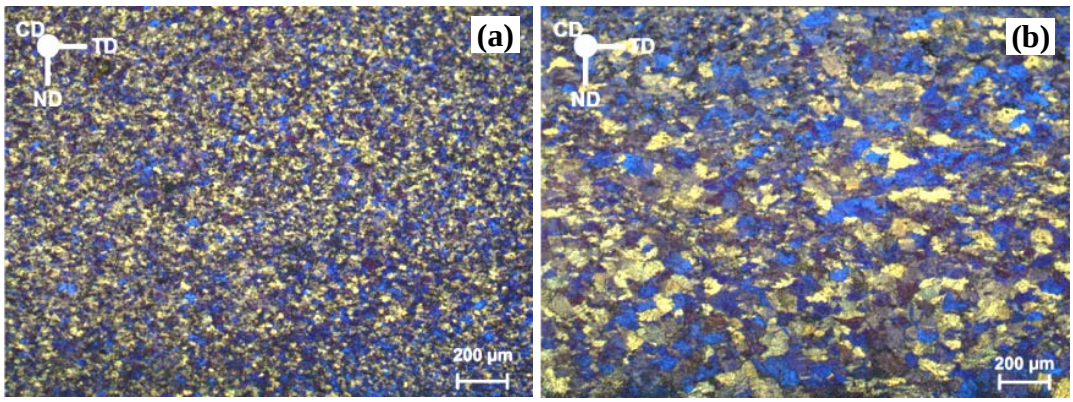

Figure 5.7 Polarised optical light microscopy images of transverse section of AZ31/5SiC$_p$ composite TRC strip fabricated with high shear treatment (a), and without high shear treatment (b).

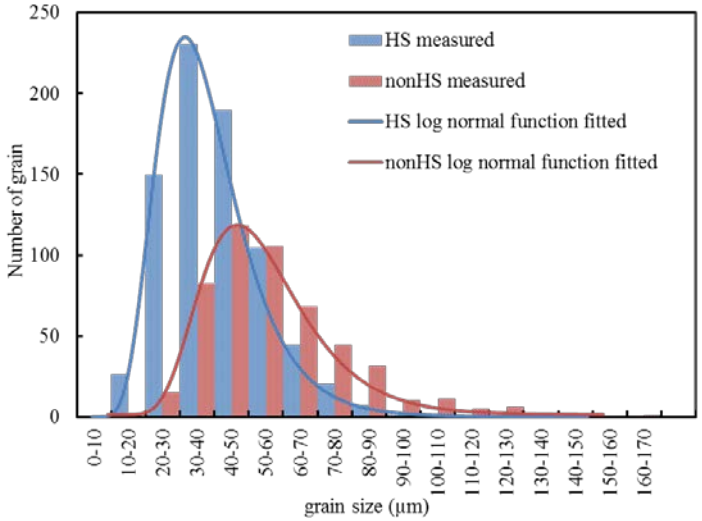

Figure 5.8 The primary α-Mg grain size distribution in transverse section of AZ31/5SiC$_p$ composite TRC strip fabricated with high shear treatment (HS) and without high shear treatment (nonHS).

Figure 5.9 shows the microstructure inhomogeneity of nonHS sample with both the polarized and bright field micrographs. With absence of SiC particles in **Fig. 5.9**(a) and (c)), a coarse primary α-Mg with size about 120 µm was observed, which was measured in the polarized micrograph.

On the other hand, with the SiC particle agglomeration/cluster in Mg matrix (brighter contrast in **Fig. 5.9**(b) and dark contrast in **Fig. 5.9**(d)), a more refined microstructure was observed which is typical microstructure of fine α-Mg grains. These microstructures suggest that the fine primary α-Mg grains in the composite TRC strip relate to the presence of SiC reinforcement as individual particles or small agglomerations/clusters.

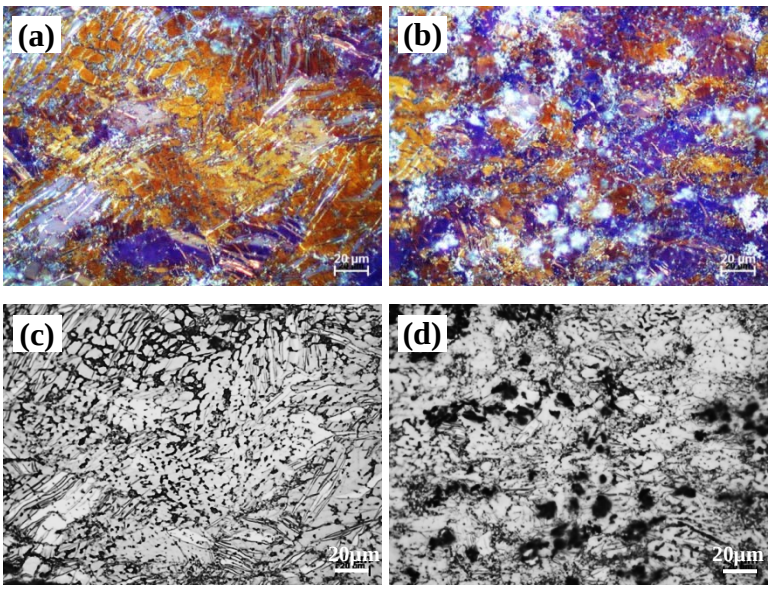

Figure 5.9 Polarized and bright field optical microstructures of nonHS AZ31/5SiCp composite strip in particle free area (a) and (c), and SiC cluster area (b) and (d), respectively.

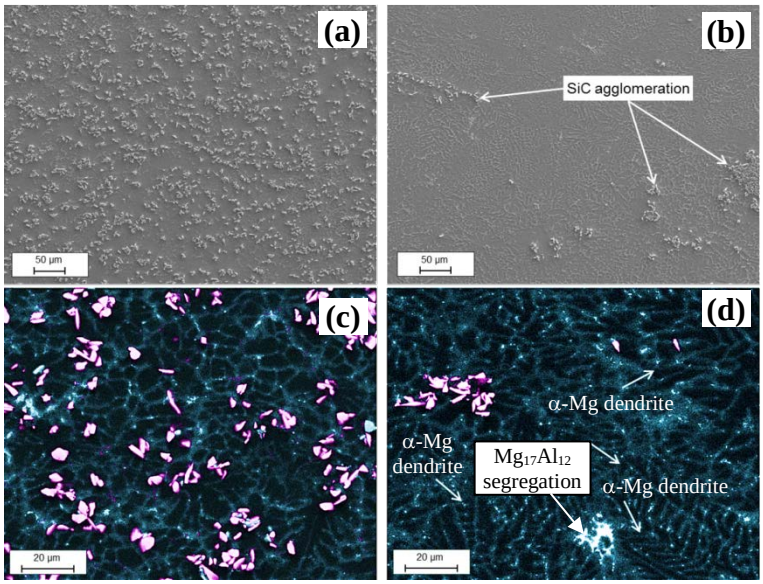

Figure 5.10 SEM image and the EDS mapping (Si and Al elements overlap) of the AZ31/5wt%SiC_p composite TRC strip fabricated with high shear treatment (a) and (c), and without high shear treatment (b) and (d), respectively. The bright pink contrast represents Si element on EDS mapping and dilute white contrast represent Al element in the composite TRC sample, respectively.

Figure 5.10 shows the β-$Mg_{17}Al_{12}$ phase morphology with SiC distribution in the etched HS and nonHS strip samples. A clear α-Mg dendritic structure has been drawn out by the solute rich compounds emphasizing the interdendritic region in particle free area in the nonHS sample (**Fig. 5.10**(b)). On the contrary, the β-$Mg_{17}Al_{12}$ phase presented discretely in the HS sample with uniform distribution of SiC in **Figure 5.10**(a). The further investigation of element distribution was conducted using EDS mapping. The α-Mg dendrites with long dendrite arms and large branches (indicated with white arrow) are

shown in **Figure 5.10**(d) with Al containing solute pushed to the interdendritic area form coarse intermetallic phase. The network of interdendritic phase distributed uniformly accompanied by SiC particles were well dispersed in the HS sample (**Fig. 5.10**(c)). The improved wetting between SiC and matrix AZ31 alloy was observed in the HS strip as some of the reinforcement particles were located inside the α-Mg dendrites rather than pushed to the interdendritic area (Lloyd 1994) where the liquid solidified at a later stage.

The uniform microstructure through the strip thickness and the significant reduction of solute segregations suggest that the solidification kinetics significantly improved during TRC due to the high shear treatment. Combined with evidence above, the SiC could influence the solidification behaviour of AZ31 alloy during the casting process. Previous research (Cai et al. 1999) suggests that SiC particles are a potent nuclei for the heterogeneous nucleation of α-Mg due to small misfit of 2.3% with crystallographic orientation relationship of $(10\bar{1}0)_{Mg}[0\ 0\ 0\ 1]_{Mg}//(0001)_{SiC}[\bar{1}5\bar{4}0]_{SiC}$. Fine and uniform primary α-Mg grains in the AZ31/5wt%SiC_p HS sample in **Figure 5.7**(a) could be explained as the heterogeneous nucleation was enhanced by these well dispersed SiC particles which act as potential nuclei during solidification of the strip. Therefore, nucleation take place evenly through the strip thickness and equiaxed growth prevailed due to the uniform temperature and composition fields.

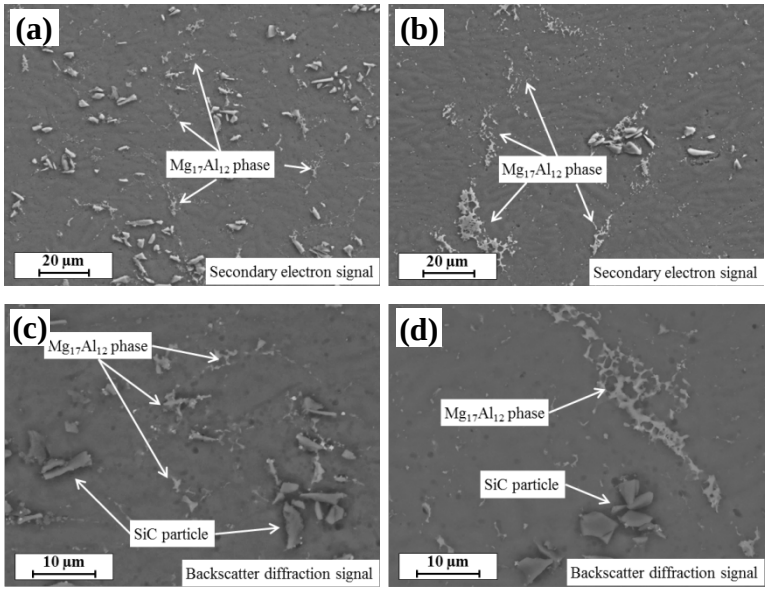

Figure 5.11 SEM image of the β-$Mg_{17}Al_{12}$ phase segregation of AZ31/5SiC_p composite TRC strip fabricated with high shear treatment (a) and (c), and without high shear treatment (b) and (d).

The promotion of the enhanced nucleation sites in the HS sample by good dispersion of SiC particles minimised the solute segregation through the composite strip. The SEM images of β-$Mg_{17}Al_{12}$ phase morphology and distribution are shown in **Figure 5.11**. In the HS sample, $Mg_{17}Al_{12}$ phase marked with white arrows, was located in the interdendritic area with a length less than 10 μm (**Fig. 5.11**(a) and (c)). In the case of the nonHS sample (**Fig. 5.11**(b) and (d)), $Mg_{17}Al_{12}$ phase was coarser with size >20 μm in length, and the number density of $Mg_{17}Al_{12}$ phase significantly reduced. From the solidification sequence of AZ31 alloy (Laser et al. 2006), $Mg_{17}Al_{12}$ phase is expected to appear after the primary α-Mg formation from the melt. The size and distribution of the primary α-Mg phase can determine the size and distribution of inter-grain area and further influence the solute segregation in the TRC process (Barekar, Dhindaw 2014).

The size and distribution of the primary α-Mg grain and $Mg_{17}Al_{12}$ phase in AZ31/5wt%SiC_p composite TRC strip are all influenced by the high shear dispersion of SiC_p during the solidification. Such a uniform microstructure and chemistry is important for the composite strip to display reliable mechanical and physio-chemical performance.

5.1.3. Mechanical Properties

Strength and ductility

The mechanical properties of the homogenized HS and nonHS composite TRC strips are presented in **Figure 5.12**. The yield and ultimate tensile strengths of the AZ31/5wt%SiC_p HS strips were improved by 34.8% and 47.9% respectively, compared with that of the nonHS strips. The elongation is also improved from 2.3±0.6% to 3.0±0.3% by high shear dispersion.

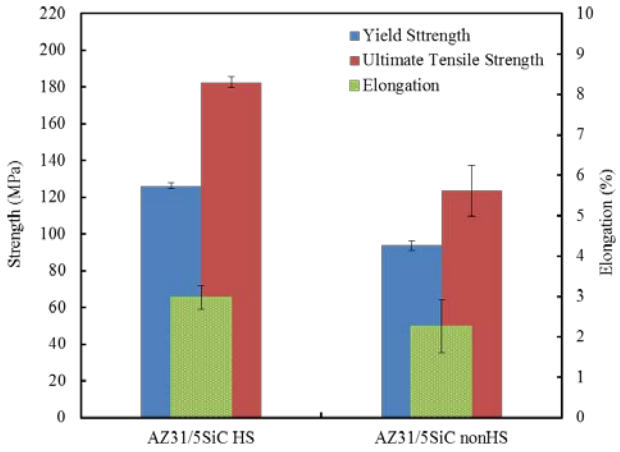

Figure 5.12 The mechanical properties of AZ31/5SiC_p composite TRC strip fabricated with high shear treatment (HS) and without high shear treatment (nonHS).

Figure 5.13 illustrates the SEM images of fracture surfaces. Uniform and small dimples were observed on the fracture surface of the AZ31/5wt%SiC_p HS sample, whereas large α-Mg grain boundaries and small dimples were observed in sample without high shear treatment. Homogeneously distributed SiC particles resulted in uniform and small dimples in the HS sample, which gives rise to the ductile fracture behaviour. On the contrary, for the nonHS sample, large SiC agglomeration resulted in large voids, which contributes to the brittle fracture like behaviour. Under tensile load, homogeneous distribution of the reinforcement particles contributes to uniform stress distribution and well-bonded fine and hard SiC particles within AZ31 matrix behave like precipitates increasing the energy consumption for void formation, deboning or separation between the reinforcements and matrix (Sreekumar et al. 2015). On the other hand, in the nonHS samples the weaker bonding between SiC/SiC interfaces within SiC clusters, leads to development of cracks at lower loads and the failure occurs at early stages of the tensile loading.

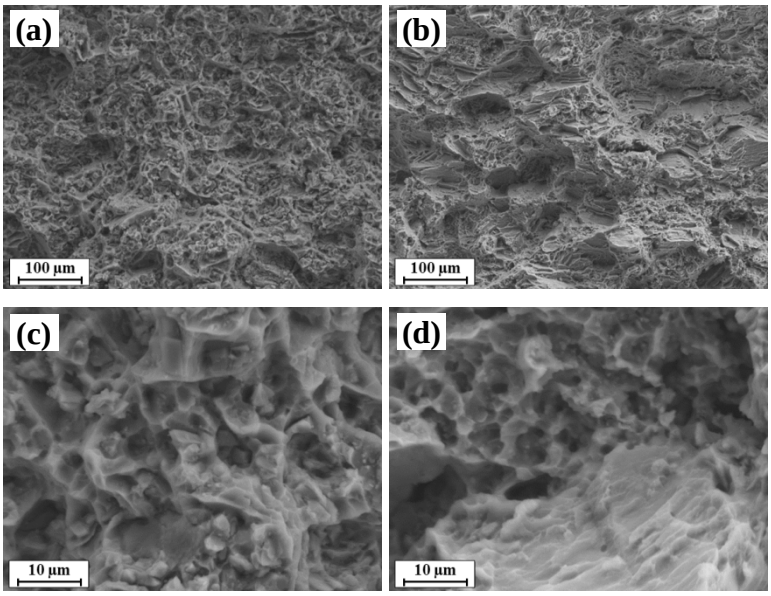

Figure 5.13 SEM image of the tensile fracture of AZ31/5SiC_p composite TRC strip fabricated with high shear dispersion (a) and (c), and without high shear dispersion (b) and (d).

Hardness

The Vickers hardness of the AZ31/5wt%SiC_p HS and nonHS composite TRC strip samples are shown in **Figure 5.14**. The average Vickers hardness values of the HS and nonHS samples are 86 Hv0.5 and 75 Hv0.5, respectively. The Vickers hardness values along three line scans through the strip thickness for the HS sample are in a narrower range (indicated with blue shade) between 74 Hv0.5 and 99 Hv0.5. In contrary, in the

nonHS sample, large fluctuations (red shade) observed, which reflects the inhomogeneous SiC_p distribution. In the regions where SiC agglomerates hardness values is as high as 120 Hv0.5 was observed. However, in the SiC particle free regions, a lower hardness of 45 Hv0.5 was recorded. Hurricks (Hurricks 1973) reviewed the metallurgical factors controlling the abrasive wear resistance of metallic materials and identified a direct correlation between measured hardness and wear performance. To have superior wear performance, it is important to have minimal spatial variation of the hardness across the composite. The homogeneous hardness observed in the HS strip suggests higher wear resistance for the HS composite strip sample which can be attributed to improved SiC reinforcement distribution by high shear treatment.

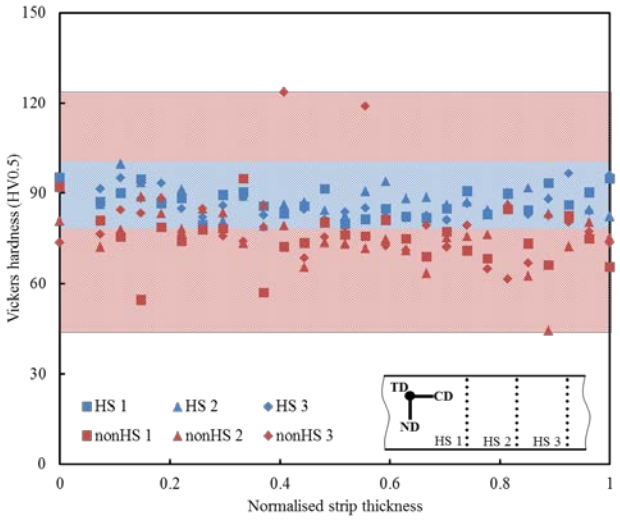

Figure 5.14 The Vickers hardness of AZ31/5SiC_p composite TRC strip fabricated with high shear treatment (HS) and without high shear treatment (nonHS). Inset shows a sketch of three line scans of HV indentation locations.

Elastic modulus

Halpin-Tsai model (Halpin 1984) is used to compare the elastic modulus measured with theoretical elastic modulus for both homogenized HS and nonHS composite TRC strips. The elastic modulus of a composite is:

$$E_c = \frac{E_m(1+2sqV_p)}{1-qV_p} \tag{5.3}$$

where

$$q = \frac{(E_p/E_m-1)}{(E_p/E_m)+2s} \tag{5.4}$$

and E_c, E_m and E_p are the elastic modulus of the composite, matrix and particle, respectively, V_p is the volume fraction of particle, and s is the particle aspect ratio. Since SiC particle morphology used in this study is angular, s is measured to be between 1.5 and 3.

The comparison of elastic modulus prediction and experimental measurement is presented in the **Figure 5.15**. The measured elastic modulus for the HS sample is in agreement with the range predicted by the model but that for the nonHS composite TRC strip has a significant deviation from the model prediction. In general, the volume fraction of reinforcement is the dominant factor that controls the elastic modulus. However, given similar volume fraction between the HS and nonHS samples, spatial distribution of particles significantly influences the elastic modulus. Non-uniform distribution of the reinforcement leads to the non-uniform stress distribution in the material and may cause the reduction in the modulus (Wang et al. 1993).

The measured elastic modulus of the AZ31/5wt%SiC_p nonHS composite deviated from the theoretical calculation due to the presence of large SiC agglomeration and particle free areas. In the case of the AZ31/5wt%SiC_p HS composite TRC strip, the measured elastic modulus is in good agreement with the Halpin-Tsai model due to homogeneous distribution of SiC particles.

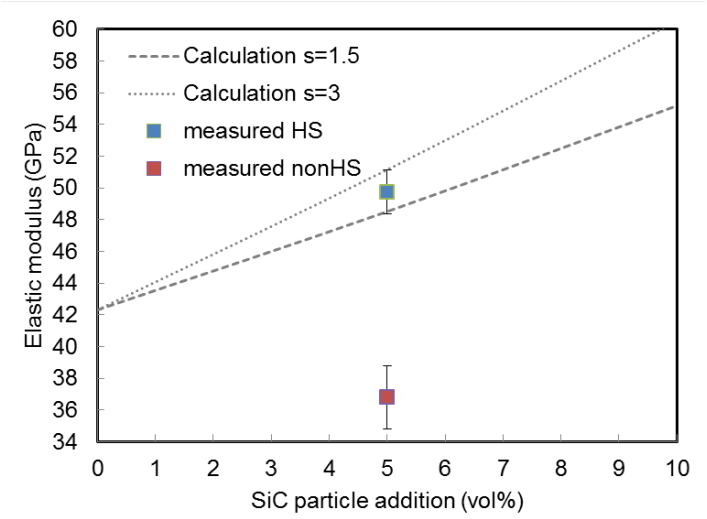

Figure 5.15 The predicted modulus as a function of reinforcement concentration by Halpin-Tsai model with two different particle aspect ratios. Measured elastic modulus of AZ31/5SiC_p composite TRC strip with high shear treatment (HS) and without high shear treatment (nonHS) are also shown.

5.2. The Effect of SiC on the Refinement of Primary α-Mg Grains in AZ31 alloy

The grain refinement of α-Mg grains in AZ31 alloy with SiC addition and high shear treatment was observed in the AZ31/5SiC_p composite strip fabricated by rotor-stator mixer treatment and TRC process. Therefore, the grain refinement could be enhanced through heterogeneous nucleation by MgO and/or SiC particles. The objective of this part of my research is to investigate the effect of SiC_p addition on the grain refinement of α-Mg with high shear treatment Mg-MMCs and study the mechanism of grain refinement of AZ31 alloy with SiC_p addition from the view of crystallography.

5.2.1. The Effect of SiC Addition on the Refinement of Primary α-Mg Grain

Figure 5.16 shows the microstructures of AZ31 alloy with high shear treatment and different SiC additions cast in Φ 40 mm stainless steel mould. An equiaxed structure was observed through all the samples of AZ31 ally with different SiC additions.

Dendritic structures form in AZ31 without SiC_p (**Fig. 5.16**(a) and (b)) with a reduced grain size was observed in the high shear treated sample. The grain refinement due to high shear has been studied and found to be due to the dispersed MgO particles acting as the potent nuclei and enhancing the heterogeneous nucleation in the solidification process of AZ31 alloy. With the 0.1 wt% and 0.5 wt% additions of SiC particles, the dendritic structures reduced and α-Mg grain size is 180.52±67.54 μm and 159.80±64.57 μm (**Figure 5.16**(c) and (d)), respectively.

The morphology of α-Mg grains in AZ31 alloy transformed from well-developed dendrites to the rosette grains with further SiC addition (Figure 5.16(e), (f) and (g)). The structure change of α-Mg in AZ31 alloy with increased SiC addition indicates that the solidification kinetics of primary phase changed and led to a rosette grain formation with high content AZ31/SiC_p samples. The thermal condition of AZ31 alloy with high SiC addition changed due to the difference of thermal physical properties including specific heat and thermal conductivity, and thus difference led to a reduced thermal gradient at the solidification front of individual α-Mg grain during solidification.

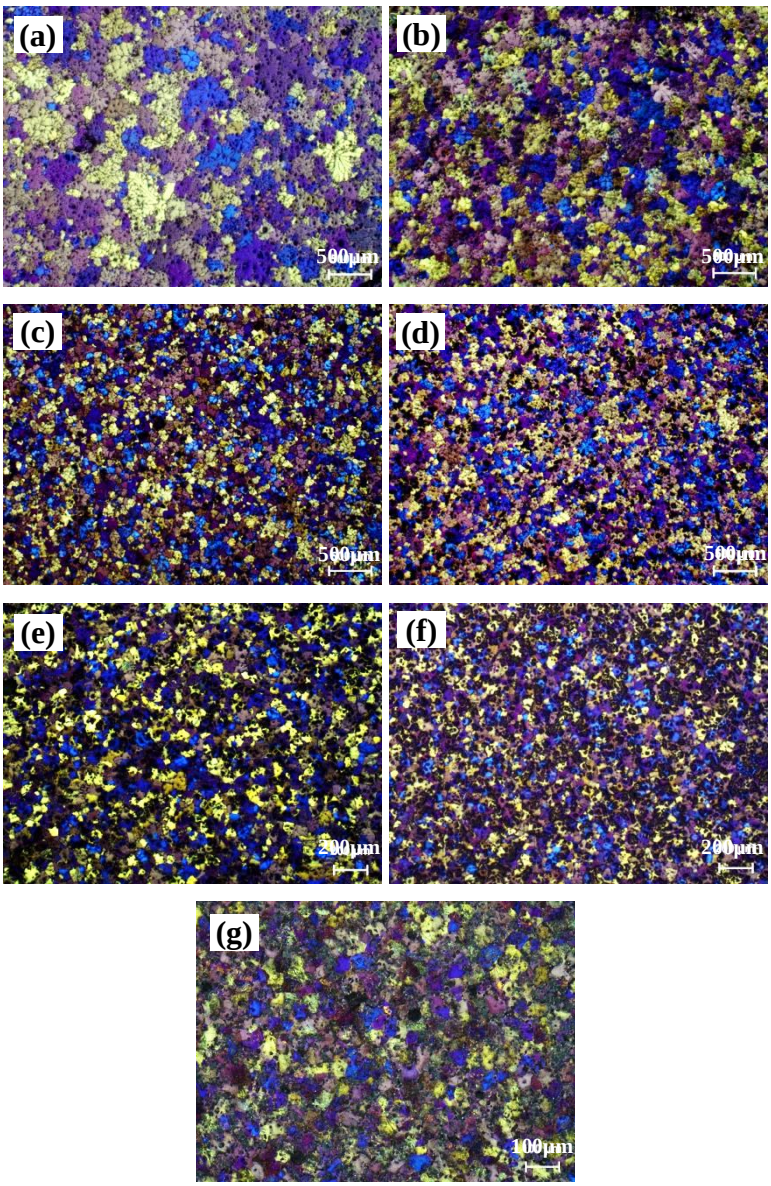

Figure 5.16 The as-cast microstructure of AZ31 alloy with different SiC contents, (a) 0SiC and no high shear , (b) 0SiC with high shear, (c) 0.1wt% SiC with high shear, (d) 0.5 wt% SiC with high shear, (e) 1.0 wt% SiC with high shear, (f) 3.0 wt% SiC with high shear, and (g) 5.0 wt% SiC with high shear. Different magnifications were used to acquire microstructure of AZ31 alloy with varying SiC addition.

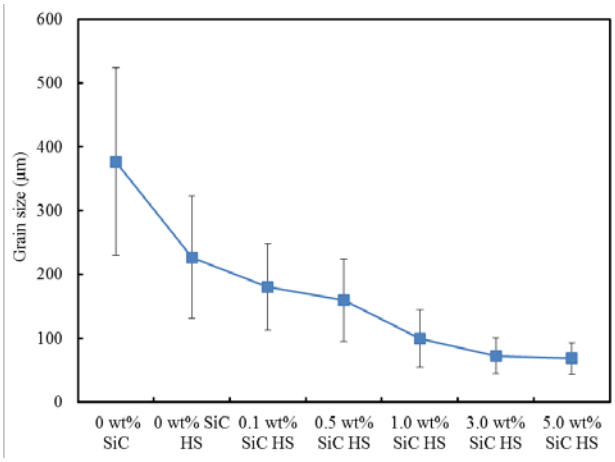

Figure 5.17 The α-Mg grain size of AZ31 alloy with different SiC additions.

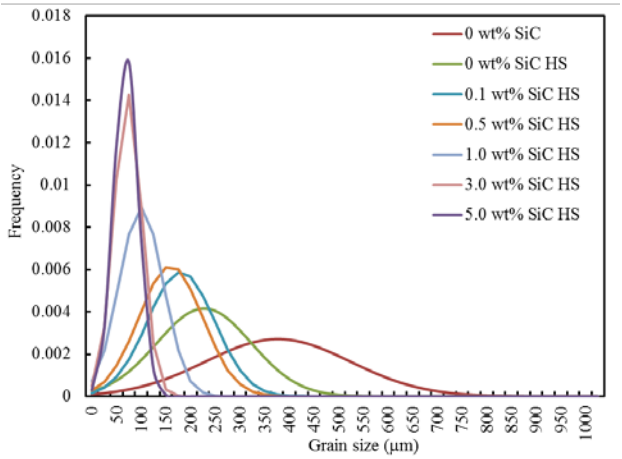

Figure 5.18 The α-Mg grain size distribution of AZ31 alloy with different SiC additions.

Figure 5.17 and **Figure 5.18** illustrate the α-Mg grain size variation and distribution with different SiC additions. The α-Mg grain size decreased with the increased SiC addition and high shear treatment from 376.66±146.92 μm of reference AZ31 alloy to the 69.27±24.57 μm of high shear treated AZ31/5SiC_p composite. The distribution of grain size becomes narrower with the higher SiC addition. The standard deviation of grain size of AZ31 alloy with high shear but without SiC addition was 95.87 μm, however the value of AZ31/1SiC_p HS sample was 44.53 μm and AZ31/5SiC_p HS was 24.57 μm. Although the effect of MgO cannot excluded in the high shear treated AZ31/SiC_p sample as the magnesium oxide is unavoidable in the melting and casting, the effect of SiC on the grain refinement was observed with only 0.1 wt% SiC addition in **Figure 5.16** (b) and (c) in comparison to SiC free samples.

5.2.2. The Mechanism of α-Mg Grain Refinement

The effect of SiC on α-Mg grain refinement in the AZ31 alloy with high shear was investigated also with the conventional mould casting. However, the mechanism behind the grain refinement is still unclear. The cooling curve of alloy during the casting helps to reveal the solidification behaviour of molten metal during the phase transformation from liquid to solid.

Figure 5.19 shows the cooling curves of AZ31 alloy with high shear and AZ31/5SiC_p composite with high shear. Prior to solidification, the cooling rate of both curves were almost identical at 0.16 K/s for AZ31 and 0.15 K/s for AZ31/5SiC_p composite. The liquidus temperatures, which are the starting point of nucleation, are both around 628.5°C.

The undercooling is the difference between the liquidus temperature and the recalescence temperature (minimum point on the cooling curves before the temperature rises again). For the curves with and without SiC addition, the undercooling is 0.16°C and 0.30°C, respectively.

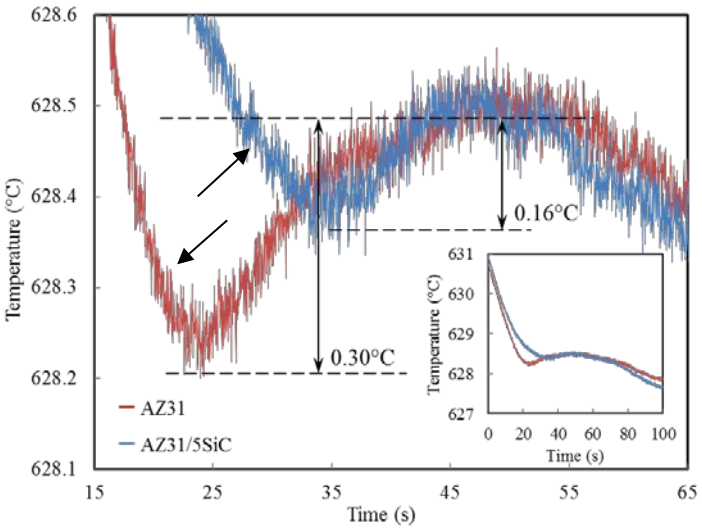

Figure 5.19 Measured cooling curves for the AZ31 alloy with and without SiC particle addition. The maximum undercooling is estimated on the cooling curve relative to the thermal plateau after recoalescence. The measured cooling rate is 0.16°C/s for AZ31 melt, and 0.15°C/s for AZ31/5SiC$_p$ melt.

The important stage between nucleation start temperature and nucleation finish temperature (indicated in black arrows) determines the final grain size. Where nuclei start to grow, the melt temperature drops at this stage, the cooling curve starts to deflect. Further growth of matrix releases more latent heat and more deflection of the curve is observed.

Based on the free growth model (Greer et al. 2000), nucleation on substrates with various diameters starts to grow freely at different temperatures. The larger the substrate diameters, the smaller the undercooling required. Therefore, the number of grains that grow increases with the temperature dropping from the nucleation starting point to the finishing point. When the temperature drops to the nucleation finishing point, there is no further potential nucleation sites that can produce more grains freely, and the number of grains which grow will be determined (Jiang 2013). In previous research, the undercooling (Maxwell, Hellawell 1975) is recognized as the driving force and key factor for the liquid-solid transformation during solidification process. Smaller undercooling indicates that lower driving force is required which means more effective nucleation sites are available in the melt.

With similar cooling rate for both curves, the undercooling for the AZ31/5SiC$_p$ composite melt was smaller compared with that without SiC addition. This suggested that there are more grains that grow in the sample with SiC addition. Combined with that the number of grains that are viable can potentially determine the final grain size of alloy, the grain size of the composite should be smaller than that without SiC additions. The SiC particles could be an effective nucleation site for α-Mg in AZ31 alloy.

The crystallographic examination of SiC particles with α-Mg phase, The SEM images and EBSD patterns of selected sample area were recorded and indexed with TEAM™ software (EDAX Inc.). The result was investigated with OIM™ crystallography orientation analysis software (EDAX Inc.). The indexing was performed with the lattice parameters: $a =$ 0.3081 nm and $c =$ 1.5125 nm for hcp α-SiC (6H); and $a =$ 0.3200 nm and $c =$ 0.5198 nm for hcp α-Mg (Capitani et al. 2007, Von Batchelder 1957).

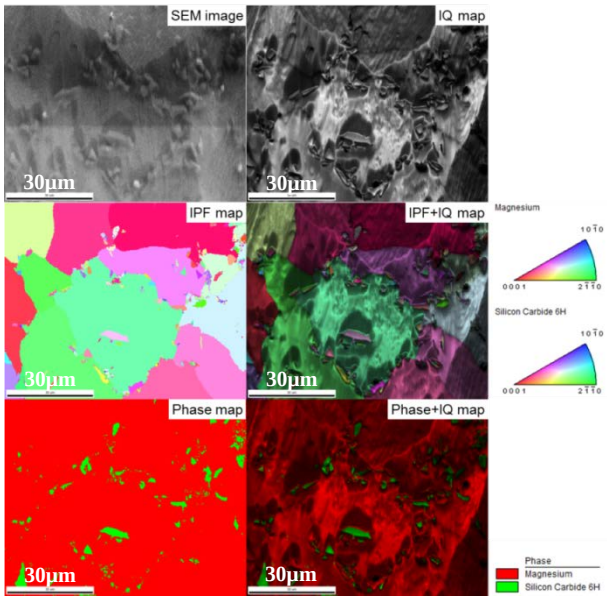

Figure 5.20 The EBSD mapping of AZ31/5SiC composite with crystallographic orientation and phase information obtained simultaneously in one mapping.

The crystal structure and lattice parameters are similar between α-SiC (6H) and α-Mg, so accurate indexing the Kikuchi pattern of one phase from the other is critical for further crystallographic data analysis. **Figure 5.20** shows a typical EBSD mapping of AZ31/5vol%SiC$_p$ sample. The crystallographic OR information is presented in the inverse pole figure with varying colour indicating different crystallographic orientations of α-SiC (6H) and α-Mg. From the phase map **of Figure 5.20,** the silicon carbide is

distinguished with green and magnesium with red. Combining the inverse pole figure and phase map of composite sample, it shows a well indexed EBSD map with accurate phase identification.

Figure 5.21 Image of the EBSD mapping of AZ31/5SiC composite with grain and image quality maps overlapping, each individual α-Mg grain is identified with unique number.

Figure 5.21 presents a 300 µm × 250 µm EBSD map of composite sample. The indexing rate of α-Mg partition is 96.03% with an average confidence index (CI) value (Wright, Nowell 2006) of 0.73 and average fit of 0.90. The indexing rate of α-SiC (6H) partition is 69.32% with an average confidence index value of 0.38 and average fit of 1.24.

The unique grain and image quality overlapping map provides crystallographic information of 101 α-Mg grains containing 667 α-SiC (6H) particles inside α-Mg grain and along the grain boundaries. Seventy-nine couples of SiC-Mg within 20 grains were examined using the numerical OR determination method correlating the two phases by Euler rotations which has been demonstrated by Qiu and Zhang (Qiu et al. 2009).

Instead of Kikuchi pattern, Euler angle (ϕ_1, $\phi$and ϕ_2) can be indexed and recorded automatically from EBSD mapping process for presenting the crystallographic orientation of target phases. These angles are the orientation of the crystal on terms of a reference coordinate defined by the sample holder profile. An Euler rotation matrix (Bunge 1982) can usually be expressed as:

$$R(\phi,\xi)=\begin{bmatrix}(1-u^2)\cos\phi+u^2 & uv(1-\cos\phi)+w\sin\phi & uw(1-\cos\phi)-v\sin\phi\\ uv(1-\cos\phi)-w\sin\phi & (1-v^2)\cos\phi+v^2 & vw(1-\cos\phi)+u\sin\phi\\ uw(1-\cos\phi)+v\sin\phi & uw(1-\cos\phi)-u\sin\phi & (1-w^2)\cos\phi+w^2\end{bmatrix} \quad (5.5)$$

where ϕ is the rotation angle (Euler angle) and ξ is the vector of rotation axis, *u*, *v* and *w* are the three components of the vector ξ.

The OR matrix (${}_{A}\mathbf{O}_{S}$) between an arbitrary crystal A and the sample holder profile S can be calculated by the product of the three Euler Rotation matrices (**R**, $\mathbf{R}_1$ and $\mathbf{R}_2$) which corresponding to the three Euler angles (Bunge 1982):

$${}_{A}\mathbf{O}_{S}=\mathbf{R}_2(\phi_{2A},\mathbf{z}_2)\mathbf{R}(\phi_A,\mathbf{x})\mathbf{R}_1(\phi_{1A},\mathbf{z}_S) \quad (5.6)$$

Where $\mathbf{z}_S$ is normal dissection of the sample holder. In Supra 35 SEM, the $\mathbf{z}_S=[0\quad 0\quad 1]'$, $\mathbf{x}=\mathbf{R}_1[1\quad 0\quad 0]'$ and $\mathbf{z}_2=\mathbf{R}\mathbf{R}_1\mathbf{z}_S$. With same description, the OR matrix between crystal B and the sample holder profile S can be expressed as (Bunge 1982):

$${}_{B}\mathbf{O}_{S}=\mathbf{R}_2(\phi_{2B},\mathbf{z}_2)\mathbf{R}(\phi_B,\mathbf{x})\mathbf{R}_1(\phi_{1B},\mathbf{z}_S) \quad (5.7)$$

Then, the OR matrix between crystal A and B is (Qiu et al. 2009):

$${}_{B}\mathbf{O}_{A}={}_{B}\mathbf{O}_{S}({}_{A}\mathbf{O}_{S})^{-1} \quad (5.8)$$

Hence, the determination of OR of two certain crystals becomes the calculation of two sets of Euler angles (ϕ_{1A}, ϕ_A and ϕ_{2A}) and (ϕ_{1B}, ϕ_B and ϕ_{2B}). Such crystallographic information can be directly extracted from EBSD analysis.

So based on the methodology described above, two distinguishable, but reproducible ORs are observed and are expressed as:

$$[10\bar{1}0]_{SiC}//[\bar{2}113]_{Mg},\ (0006)_{SiC}//(10\bar{1}1)_{Mg},\ (1\bar{2}1\bar{6})_{SiC}//(\bar{2}20\bar{2})_{Mg} \quad \text{(a)}$$

and

$$[01\bar{1}0]_{SiC}//[1\bar{1}00]_{Mg},\ (0006)_{SiC}//\ (0002)_{Mg},\ (\bar{2}110)_{SiC}//(11\bar{2}0)_{Mg} \quad \text{(b)}$$

In the 79 determined ORs in the SiC-Mg system, there are 10 OR (a), 5 OR (b) and other random ORs. Reproducibility of these two distinguishable ORs indicates the crystallographic relationship between heterogeneous nucleation sites and the matrix

metals (Qiu et al. 2009), confirming that the α-Mg grains did nucleate on the α-SiC (6H). Other random ORs of SiC-Mg system suggest that the corresponding silicon carbide particles only act as the reinforcing phase.

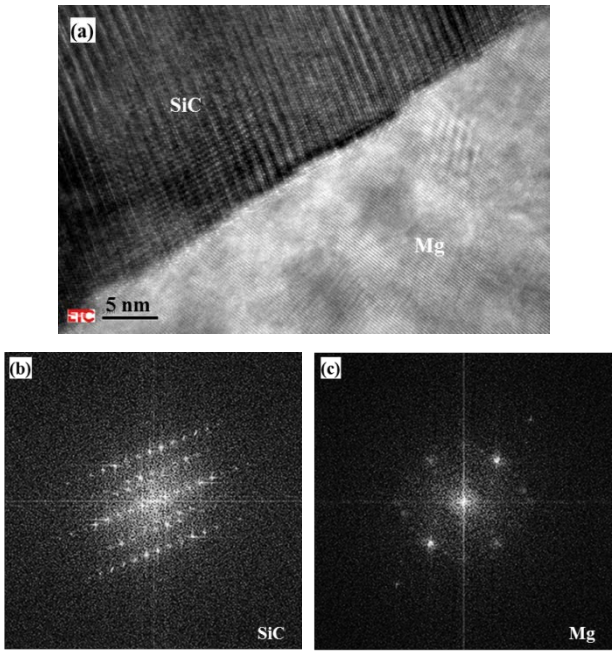

Figure 5.22 High resolution image of SiC and α-Mg interfacial lattice arrangement (a) and their corresponding crystal diffraction patterns (b) and (c) obtained by FFT, respectively.

The interface between α-SiC (6H) and α-Mg of as-cast AZ31/5wt% composite is also examined with HRTEM to exclude the possible nucleation mechanism by interfacial reaction between reinforcement and matrix (Easton et al. 2006, Huang et al. 2011). A clear interface is observed in **Figure 5.22**(a) between α-Mg matrix (bright contrast) and corresponding SiC particle (dark contrast). The diffraction patterns of both crystals are obtained through FFT processing for phase identification. There is no significant contrast change found in **Figure 5.22**(a), which indicates that α-Mg and SiC particle are in contact at the interface directly. This supports the nucleation of α-Mg by α-SiC (6H) with the crystallographic orientation relationships identified above.

Chapter 6 Melt Conditioned Twin Roll Casting Process for AZ31 Thin Gauge Strip: Results and Discussion

6.1. Development of Twin Roll Casting Facility

The objectives of this part of the research are development of twin roll casting facilities and optimisation of twin roll cooling system for melt conditioned twin roll casting process.

6.1.1. Development of Melt Feeding System

The continuous MC-TRC process primarily consist of integration of melt conditioning unit with TRC facilities, including tundish for transferring melt from a tilt furnace to the twin roll caster. The schematic illustration of the rotor-stator mixer involved MC-TRC process for thin gauge Mg-alloy strip casting shown in **Figure 6.1**.

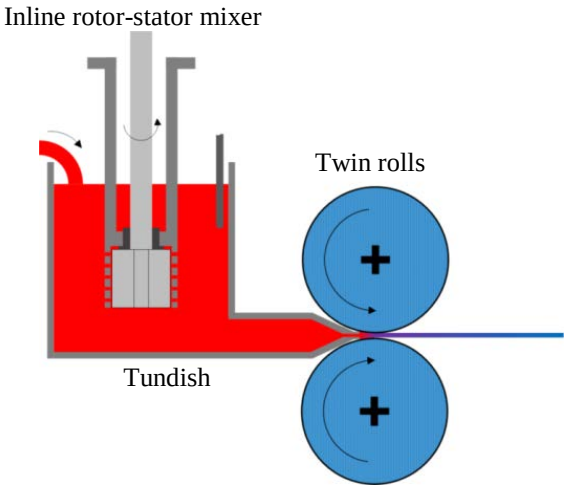

Figure 6.1 Schematic illustration of Melt Conditioned Twin Roll Casting (MC-TRC) process for thin gauge Mg alloy strip incorporating rotor-stator high shear technology.

In the initial facility development stage, a steel rotor-stator mixer with stator inner diameter of Φ 32 mm was employed for high shear of the Mg alloy melt.

The main advantages of the high shear device include, but are not limited to, enhancement of kinetics for chemical reactions, homogenisation of chemical composition, dispersion of solid particles in liquid and forced wetting of usually difficult to wet solid particles in the liquid. In the present research, the high shear device is used for physical grain refinement by dispersing naturally occurring oxides.

Development of feeding system Phase 1

The conversion of the discontinuous process to continuous MC-TRC is associated with a technical challenge to design a fit-for-purpose tundish having a separate chamber to facilitate continuous high shear and stable delivery of the MC treated melt to the roll surface for the strip casting. In order to understand the flow behaviour of liquid melt during and after high shear treatment, preliminary tundish design was made with transparent acrylic tubes and sheets (**Figure 6.2**(a)). The tundish was divided into three sections namely, pouring, shearing and delivery. A baffle was placed at the entry of the shearing chamber to prevent incoming liquid bypassing the high shear zone. Another baffle was positioned at the exit of the shearing chamber to avoid turbulence created by the rotor-stator mixer and to provide enough residence time for melt conditioning treatment. The effect of intense shearing on fluid flow was investigated by incorporating graphite particles in water. It is essential to achieve an adequate liquid circulation and homogeneous distribution of the particles. The desirable situation is when the shear force is large enough to break up the agglomerates of particles and avoid stagnant zones in the high shear chamber.

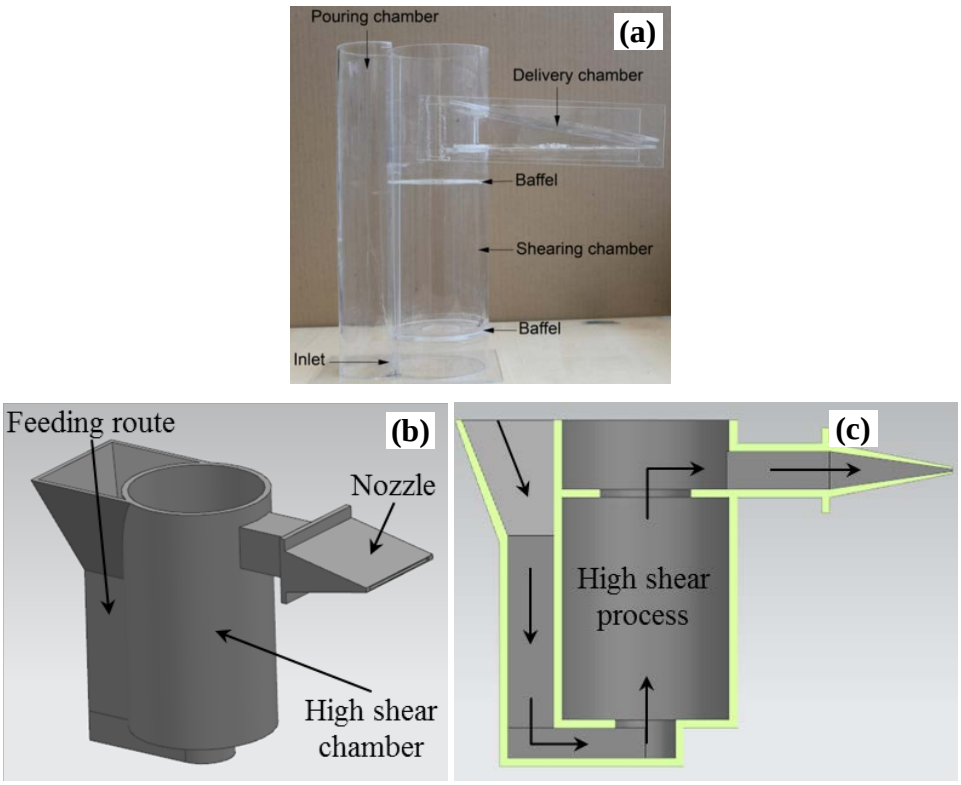

Figure 6.2 The initial design of melt feeding and conditioning tundish for MC-TRC process, (a) transparent model for fluid simulation by water and graphite particle, (b) tundish structure and (c) melt flow route inside tundish.

With preliminary water trials and modifications of transparent tundish model, a stainless steel tundish was made for continuous MC-TRC process of Mg-alloys. **Figure 6.2**(b) and (c) shows the final design and flow path of the steel tundish for continuous MC-TRC process.

As the tundish for continuous MC-TRC process was made from stainless steel, it dissipated heat to the surrounding environment and that it was difficult maintain the required melt temperature inside the tundish. To overcome the heat loss during the pre-heating step, melt shearing and transferring process, a detachable furnace setup was developed and assembled to the steel tundish as shown in **Figure 6.3**.

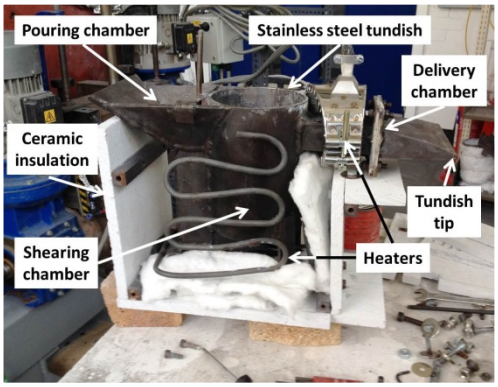

Figure 6.3 Prototype of in-house made steel tundish and equipped with heating elements for thermal control.

The heating elements were bent to specific shape encircling the outer frame of the tundish for maximum heat transference in order to compensate the heat loss and maintain the tundish temperature at service condition. Ceramic insulation boards were used to make the shell of the tundish to prevent the heat loss into the surrounding. The insulation wool was placed into the gap between the heating elements and the ceramic insulation board to enhance the heating efficiency. As the whole body of the steel tundish was wrapped in heaters and insulation except the nozzle which is in contact with the twin rolls in the MC-TRC process.

The heat radiation from the rest of the tundish body and superheated melt were expected to be the main heat source to heat up the nozzle and achieve the required working temperature as practiced in the conventional TRC process. In the first hot trial of steel tundish with molten AZ31 alloy at 680°C and nozzle pre-heated by radiation from tundish body to 580°C, the melt poured from tilt furnace into steel tundish, rose from the bottom

of shearing chamber, fulfil the chamber and then flow into the nozzle. The Mg-alloy melt froze inside the nozzle closing the tip. This suggests that the heat radiation and extra heat from Mg melt can't raise the nozzle temperature to above the AZ31 liquidus (629 °C), and caused the melt to solidify in the nozzle. The specific heat capacity of AZ31 alloy and stainless steel were around 0.96 J/g·K (Garg et al. 2007) and 0.50 J/g·K (Philip 1982), respectively. However, the weight difference between the nozzle and capacity of the Mg melt was more than 4 times. The heat of magnesium melt will be absorbed by nozzle structure when it flows over and temperature drop of Mg melt lead to the freezing of the melt in the nozzle tip. Higher melt temperature may further increase the nozzle temperature and heat it up to the liquidus of AZ31 alloy, but according to the data from the hot trial and calculated with thermal balance, AZ31 melt >730 °C is desired to heat the tundish nozzle and provide flow smoothly from nozzle tip. Thus high temperature of Mg melt would be too difficult to handle as the oxidation of Mg alloy tends to be worse with increased temperature and thus leading to fire hazard. The design of initial steel tundish has to be modified for the thermal capacity.

Development of feeding system Phase 2

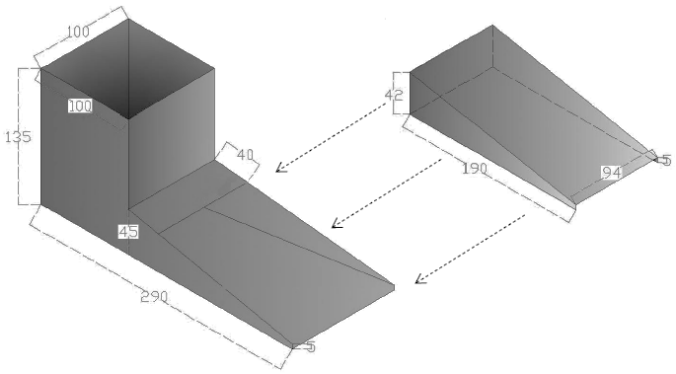

Figure 6.4 Schematic illustration of shoe tundish employed for delivery Mg melt form steel tundish for high shear treatment to the twin roll surface. The lid on the right of image will fit onto the shoe tundish before the casting experiment. All the dimension units are in millimeter (mm) unless otherwise stated (Bayandorian 2010).

The thermal condition of the nozzle of the first steel tundish prototype was tested to identify its capability to maintain an appropriate temperature for Mg melt pass. A substitute design was used to replace the nozzle on the steel tundish and implement the function of Mg melt delivery to twin roll surface. A preheated shoe-shaped tundish (**Fig.**

6.4) was connected to the steel tundish without the nozzle to collect the melt and transfer it to the twin roll caster with sufficient initial tip temperature.

Figure 6.5 shows the experimental setup and the AZ31 alloy strip cast using MC-TRC process. From left to right of **Figure 6.5**(a), the setup was separated into three sub-systems namely: melt holding system (tilting furnace), melt feeding system (rotor-stator mixer equipped steel tundish and shoe tundish), and casting system (low pressure twin roll caster).

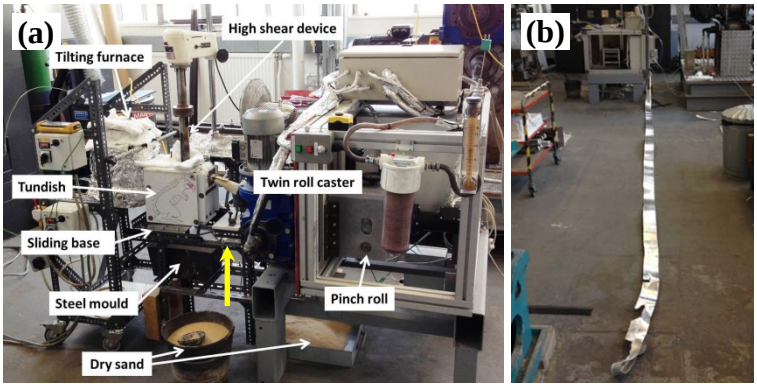

Figure 6.5 Experimental set-up of MC-TRC process combined with steel tundish for rotor-stator high shear and shoe tundish for melt delivery (a) and AZ31 strip produced by these facilities (b).

The steel tundish with rotor-stator mixer is heat to 660°C for 2 hours. The shoe tundish will also be pre-heated in the furnace at 800°C for 2 hours. The protective gas mixture of N_2+SF_6 covers the tilt furnace, the steel tundish and the open area of the shoe tundish.

Once the experiment started, the pre-heated shoe tundish is taken from furnace at 800°C and set between steel tundish and twin roll caster (the position for pre-heated shoe tundish is marked with yellow arrow), then the sliding base located to the high shear steel tundish close to shoe tundish in the correct position. The melt was poured manually at 680°C when all these setups were in position. The melt was poured into the steel tundish continuously, and then rose into high shear chamber for intensive shearing due to the high turbulence and convection generated by the inline rotor-stator mixer. The high shear treated Mg melt flow into the shoe tundish and contacted the twin roll surface from the tip of shoe tundish. A 6 meters long AZ31 solid strip was prepared from the exit of twin roll caster with good control of strip width (**Fig. 6.5**(b)).

The microstructures and thickness of MC-TRC strip in 1 m intervals were investigated to understand the consistency of strip quality and process stability of the continuous liquid metal fabrication method. **Figure 6.6** shows the results of microstructure and thickness variation of AZ31 alloy strip produced by MC-TRC process at 1 m intervals. The TRC process is a fabrication method combining casting and hot rolling processes together, any variation of process will influence the microstructure evolution and reflects in the value of separating force and strip thickness variation in macroscale (Bradbury 1994).

According to the thickness of AZ31 MC-TRC strip, the whole strip can be separated into three parts: initial, steady state and end. The thickness of strip in initial part from start point to 3 m position show an increased thickness as the casting started. This could due to the increase in the melt flow rate by the gradual build in the pouring head in the shoe tundish with the cold roll surface. From 2 m point to 3 m position, the thickness of strip reduced slightly which is in response to warming surface of rolls. The roll surface temperature increased with the decreased separating force on the similar melt feeding rate. The microstructure comparison between strip at 2 m and 3 m position show more deformed grains at 3 m position, with higher rolling temperature, it is easier to reduce the strip thickness.

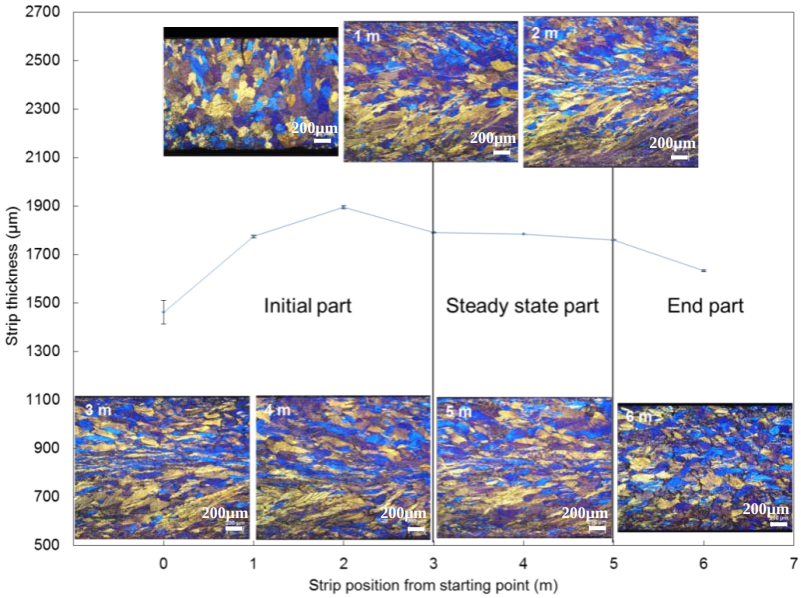

Figure 6.6 The thickness distribution and microstructure evolution of AZ31 strip fabricated with steel tundish and shoe tundish combination through the length of strip.

The steady state part of MC-TRC strip was in the range of 3 m to 5 m. The thickness of strip shows a consistent value and a similar microstructure. The end of strip is from 5 m

to the end with reduced thickness. This is related to the shoe tundish temperature dropping continuously even with the compensation from Mg melt flow. This effects the microstructure evolution and also stops the melt flow. The microstructures in 0 m position and 6 m position, both contain equiaxed grains. The equiaxed grain forms in 0 m position due to the undercooling provided by cold roll surfaces. In contrast, the equiaxed structure at the end of strip was due to the cooling effect of shoe tundish with continuous temperature drop. The melt pouring temperature decreased and time for grain growth was lower during the strip solidification. When the shoe tundish temperature continuously decrease below the liquidus of AZ31 alloy (~629°C), the melt solidified in the shoe tundish and melt flow stopped.

The prototype of melt feeding system with shoe tundish involved was employed with the other sub-systems for the MC-TRC process. The experimental setup functions well and a 6 m long AZ31 alloy strip was cast using this experimental setup. The strip thickness and microstructure along the whole strip were examined with 1 m interval. The result shows that the strip quality was in a limited consistency and process was in a fairly low stability as only 2 m long steady state part was achieved in more than 6 m long strip. The increasing roll surface temperature and fluctuating melt level in shoe tundish were attributing to the strip thickness. Additionally, the temperature dropping of the shoe tundish also influences the strip microstructure evolution, causing limited steady state strip and stops the melt flow.

Development of feeding system Phase 3

The result of strip produced with melt feeding system incorporate shoe tundish demonstrated the complete process route of MC-TRC with rotor-stator mixer and obtained an AZ31 strip with 6 m in length. However, as a continuous processing method, the drawback of thermal instable shoe tundish prevent the process being sustained for a longer steady state period and the instability leading to a unreliable result on the continuity of process pace.

The disadvantage of shoe tundish is the heat loss when it was taken out from pre-heating furnace. The length of the MC-TRC process is limited by the time of shoe tundish temperature. Once the temperature decreased to the liquidus of the alloy, the strip casting process will be terminated by the solidified melt prior to entering the twin rolls and block

the melt flow path. From the result of MC-TRC process, it clearly shows that less than 2 m steady state AZ31 strip was obtained before the MC-TRC process was terminated due to the temperature drop of shoe tundish. This length is insufficient for demonstrating a process which is expected to be continuous.

The focus of melt feeding system was on the nozzle temperature control. A thermally controlled nozzle on the steel tundish for high shear treatment was desired. **Figure 6.7** shows the difference between previous shoe tundish involved melt feeding system and new design of integrated tundish with a temperature controlled nozzle for melt delivery. The new design of temperature controlled nozzle reduced the pre-heating shoe tundish before the experiment which required not only quick motion but also the need to precisely assemble the full experimental setup. The experimental setup with thermally controlled nozzle equipped tundish (**Fig. 6.7**(b)) composed of all stationary parts will be in position and only waiting for the start of process by melt pouring from a tilt furnace.

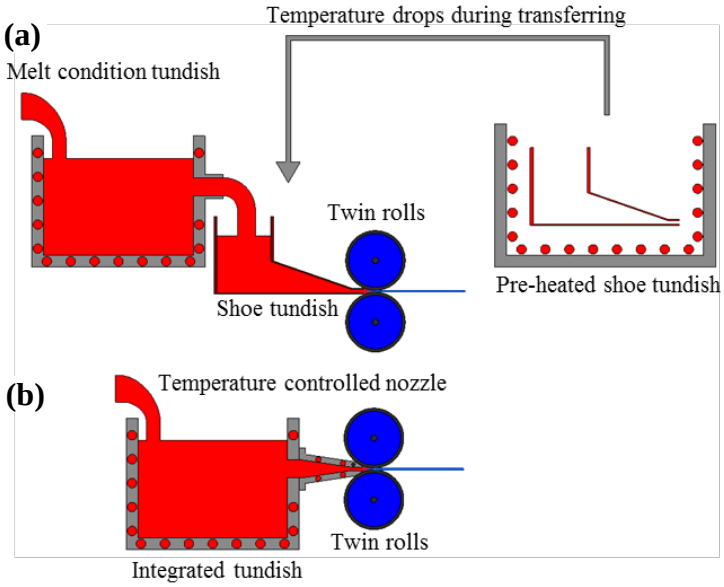

Figure 6.7 Schematic illustration of melt feeding system development modification from steel tundish and shoe tundish combination (a) to integrated tundish with thermally controlled nozzle (b).

The nozzle contained four Φ 6.5 mm × 100 mm cartridge elements on both sides of nozzle and a Φ 1.5 mm chromel-alumel type K thermal couple was placed at the centre of nozzle tip to monitor and adjust cartridge heater temperature. These heaters are able to heat the nozzle to maximum temperature of 750°C without radiation heat from rest of steel tundish as shown in **Figure 6.8**(a) and are capable of delivering the AZ31 melt from nozzle tip without melt freezing (**Fig. 6.8**(b)).

The integrated tundish was then deployed for strip casting process demonstration and the experimental setup is shown in **Figure 6.9**(a) with an 11.8 m long strip produced using this setup (**Fig. 6.9**(b)). The integrated tundish including the tundish body and nozzle was heated to 660°C for more than 2 h and protected with N_2+SF_6 gas mixture. The melt was poured at 660°C manually with a stable flow rate. The twin rolls were rotating at the speed of 5 m/min. As a result, an 11.8 m long strip was cast continuously with this new prototype incorporating an integrated tundish with a thermally controlled nozzle. The nozzle temperature is no longer a limiting factor for process duration as it can be in a constant temperature set by the four cartridge heaters. The length of strip casting process was only determined by the capacity of tilt furnace. This 11.8 m long strip consumed almost the entire melt load in the demonstration with a good strip width control 100 mm ± 5 mm.

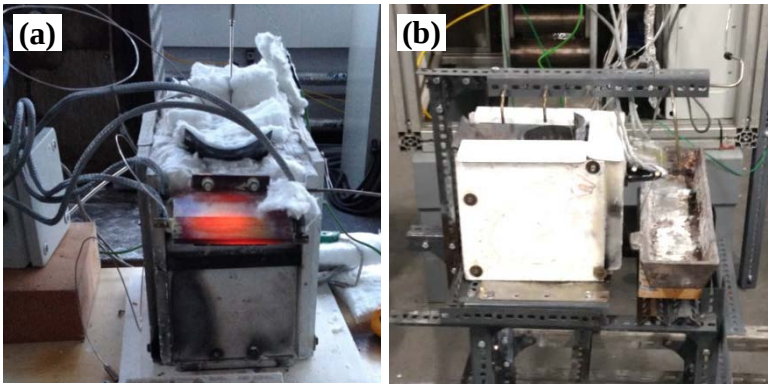

Figure 6.8 The prototype of integrated tundish equipped with thermally controlled nozzle, (a) dry test of nozzle temperature, and (b) nozzle temperature test with melt feeding.

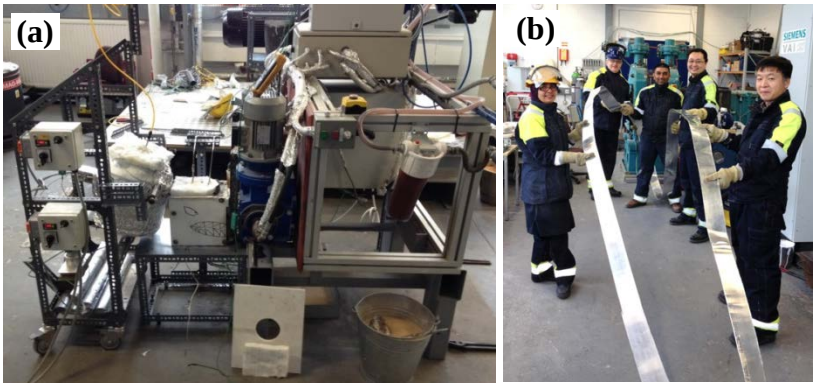

Figure 6.9 Experimental set-up of TRC process with integrated tundish equipped with thermally controlled nozzle (a) and AZ31 strip produced by these facilities (b).

The microstructure and thickness of MC-TRC strip were checked at 1 m intervals to determine the consistency of the strip quality consistency and process stability as a

continuous liquid metal fabrication method. **Figure 6.10** shows the results of microstructure and thickness variation of AZ31 alloy strip produced by MC-TRC process at 1 m intervals. Similar thickness variation as in previous experiment observed in the initial part from start to 3 m of the strip as the melt level build up and roll surfaces warmed. After that the steady state was reached for a total length of 7 m from 3 m to 10 m with a strip thickness of 1.7 mm ±0.1 mm. During this period, the thermal balance was achieved between nozzle tip temperature and roll surface temperature with a constant melt flow. It is assumed that with sufficient melt supply, this steady state period of TRC process will continue to the end of the tilt furnace capacity. The end part started from 10 m to the end of strip. With the melt level decreasing, microstructure with equiaxed grains was observed as the deformation reduced and solidification became critical.

Combined with the experimental setup of integrated tundish and strip quality result of this 11.8 m long strip, a reasonably stable, continuous and easy to access experimental setup composed of three sub-systems including integrated tundish equipped with thermally controlled nozzle was obtained and tested for the research on rotor-stator mixer incorporated MC-TRC process.

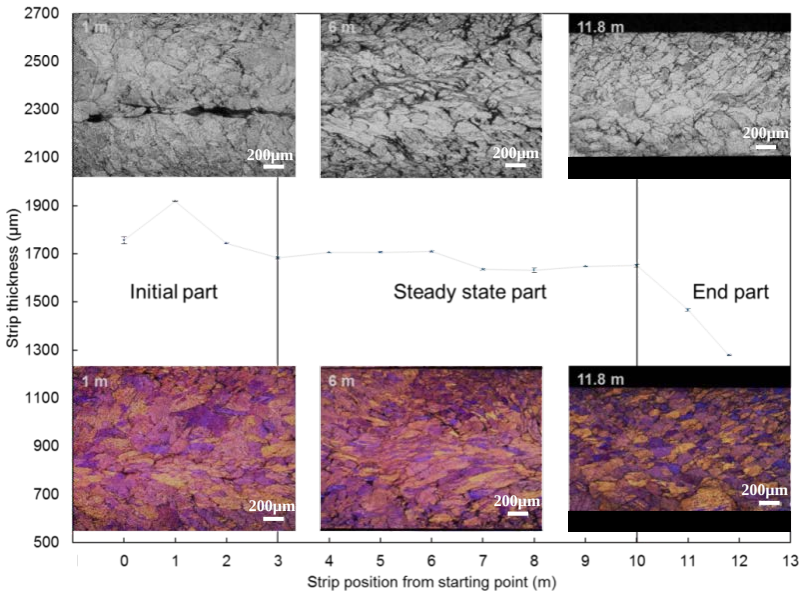

Figure 6.10 The thickness distribution and microstructure evolution of AZ31 strip fabricated with integrated tundish equipped with thermally controlled nozzle through the length of strip.

Figure 6.10 shows the microstructural evolution of a conventional AZ31 strip produced by TRC process. On the bottom of the polarised optical microstructures revealing the morphology and size of α-Mg grains. Larger α-Mg grains are observed due to the initial

high pouring temperature leading to coarse grains growing against the direction of thermal gradient. At the same time, the solute distribution is affected by such grain growth. Centre line segregation is observed due to the solute with lower melting point concentrated at the centre of strip through inter-grain channel and macro-segregation is observed. In the steady state period, the α-Mg grain size reduced and had a directional morphology (bottom middle). The solute segregation changed into discontinuous pattern compared to the initial stage (top middle) but was still severe. Once it developed into end stage of strip casting, the α-Mg grain size is further reduced and the strip thickness also reduced due to the melt supply reduction. With lower melt flow through twin roll surface, with other parameters constant, the thermal gradient increased which lead to a finer grain (bottom right) with reduced grain growth rate. This equiaxed grain growth benefits the distribution of solute more locally (top right) and reduced the centreline segregation in the TRC strip.

Development of feeding system Phase 4

An integrated tundish with heated nozzle was designed in parallel for the provision of twin-screw treated melt to the steel tundish with high shear chamber. The melt is from high shear treated AZ31 ingot. So the high shear chamber was not necessary and the function of tundish were building up melt level and delivering melt flow during MC-TRC process.

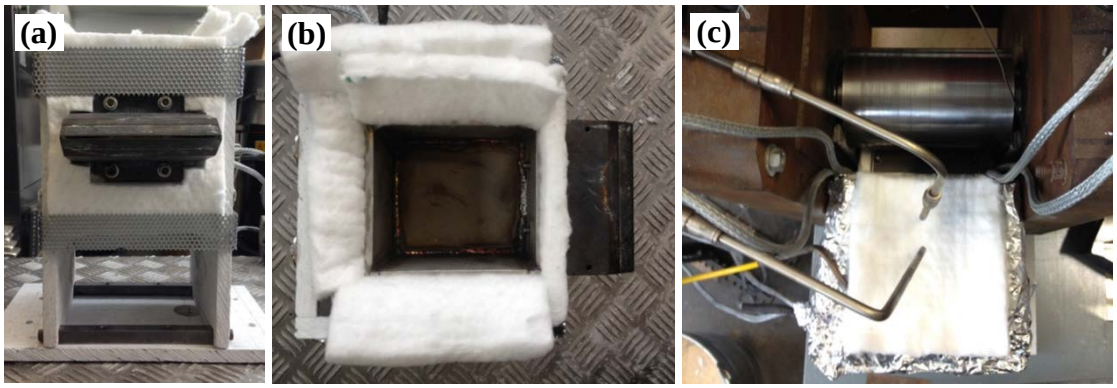

Figure 6.11 The prototype of integrated tundish with thermally controlled nozzle for MC-TRC process by pre-high sheared ingot, (a) and (b) the structure of tundish, and (c) tundish connected with TRC equipment.

The tundish for MC-TRC process with twin-screw device treated ingot was made of stainless steel. It dissipated heat to the surrounding environment and thus led to the difficulties in maintaining the required melt temperature inside the tundish. To overcome

the heat loss in the pre-heating step and melt transfer process, a detachable furnace setup was developed and assembled to the steel tundish as shown in **Figure 6.11**.

The heating elements were bent to the specific shape encircle of the outer frame of the tundish for maximum heat transfer in order to compensate for the heat loss and maintain the tundish temperature at the service condition. Ceramic insulation boards were used to make the shell of heating elements that wrapped around the tundish to prevent the heat loss to the surrounding. The insulation wool was placed in the gaps between the heating elements and the ceramic insulation board to prevent away heat loss. **Figure 6.11**(c) shows the integrated tundish connected to twin roll caster. The cables are connected to the heating elements in the tundish body and nozzle for power supply. The steel hoses deliver N_2+SF_6 protective gas mixture to the open area of the tundish. The integrated tundish was heated to 660°C for more than 2 h and protected with N_2+SF_6 gas mixture. The melt was poured at 660°C manually at a stable flow rate. The twin rolls rotated at the speed of 5 m/min.

6.1.2. Optimization of Twin Roll Cooling System

The reduced roll diameter of low pressure twin roll caster for thin gauge strip casting was beneficial to decrease the deformation applied to the strip by a low rotation torque and large clearance of roll position control to minimise the influence on the separating force. Moreover, the melt flow rate was limited to a given volume in contact with roll surface, thus leading to a less deformed microstructure of casting strip. However, this causes a significant sensitivity to thermal parameters of the twin roll caster which influences tip freezing tendency. In the above section, the importance of temperature of the nozzle for melt delivery was discussed and modification of nozzle design to prevent the melt freezing in the tip was achieved.

As a continuous process, twin roll casting, it is expected that melt flow goes through the nozzle tip, contacts with twin roll surface and been grabbed from the exit side of twin roll caster as a solid strip without any break until the melt runs low. On the other hand, if the melt flow out the nozzle tip but solidifies completely before it pass the twin roll kissing point as a chunk of wedge metal, the casting will have to stop as the flow path to the twin roll kissing point become blocked. This blockage is related to the initial roll surface thermal condition. Stainless steel, as the material used for the twin rolls, has a good

thermal conductivity (Philip 1982) which transfers the heat of melt into cooling water system in a short time depending on the temperature of roll surface. The temperature of roll surface is influenced by the water circulation system in the initial stages of casting with cooling water temperature and cooling water flow rate. During the strip casting process, the twin roll cooling system also takes the excessive heat away from roll surface to reduce the roll surface temperature and maintain the thermal gradient of TRC process.

Figure 6.12 shows the melt freezing tendency at the entrance of twin roll with different initial roll surface condition by varying cooling water temperature and flow rate set on the chiller. The cooling water temperature was varied from 7°C to 26°C and a clear difference was observed above and below 21°C at a flow rate of 8 L/min. The melt solidified initially when contacting with roll surface as the high thermal gradient of twin roll increased the solidification rate and led to a reduced solidification time. The alloy melt solidified completely before it could flow past the kissing point and pushed out as a solid strip. In contrast, the TRC process performed successfully during the initial stage and continuously produced AZ31 strip until the melt load finished. This indicates that higher roll surface temperature reduced the thermal gradient at the solidification point and the melt can pass kissing point in partially liquid state that is soft enough to be gripped and pulled through by the rotation torque of twin rolls.

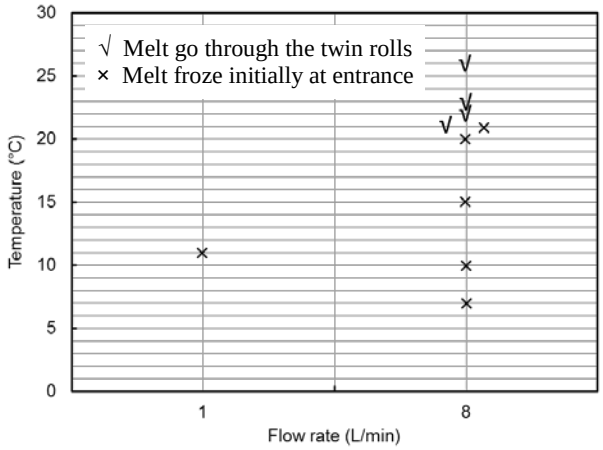

Figure 6.12 The melt freezing tendency in the twin roll entrance with the cooling water temperature and flow rate setting on the chiller.

The cooling water flow rates were also tested with 1 L/min and 8 L/min (maximum limitation for the cooling system in the laboratory). It is generally believed that the flow rate of cooling water will influence the thermal condition of roll surface during the

continuous strip casting process rather than the initial processing state. The flow rate of cooling water contributes to the thermal balancing period as roll surface temperature change due to melt contacting. Once the steady state of TRC process obtained, the thermal condition of roll surface will be determined by the flow rate of cooling water instead of cooling water temperature at the initial stage.

Figure 6.13 shows the temperature variation of inlet and outlet water from circulation cooling system at the initial state of strip casting process at a pause in pouring with the parameter setting of 26°C and 8 L/min of inlet water. There are 4 melt pours conducted in Figure 6.13 and in between 3 melt feeding pauses observed during this TRC experiment. With the melt through the twin roll surface, the heat of melt transferred into the cooling water resulting in an increase in the outlet water temperature on the temperature curve was with a positive slope. The temperature of outlet water dropped when the melt pouring paused with a negative slope value on the temperature curve (arrows pointed from bottom to top). As this curve demonstrated the interaction between melt heat and the cooling water temperature with limited strip length, a thermal balance period was expected during the continuous strip casting process between roll surface temperature and cooling water temperature in the circulation system with sufficient length of TRC strip as continuous processing method.

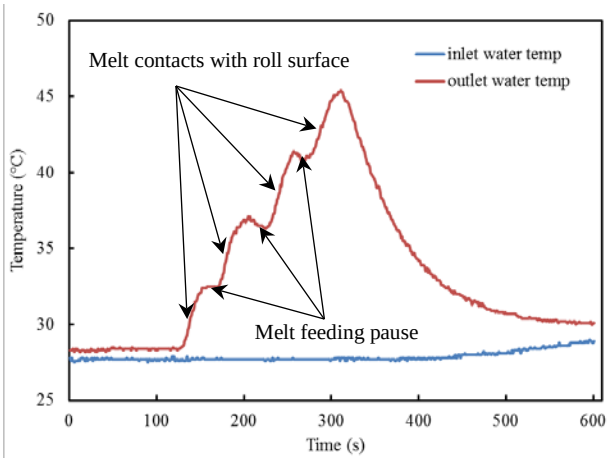

Figure 6.13 The water temperature of inlet end and outlet end of twin roll with TRC process applied with cooling water setting of 26°C and 8 L/min on the chiller.

Table 6.1 shows the thermal properties of twin roll caster at different inlet water temperatures with 655°C melt pouring temperature. The heating rate in the table was

obtained with cooling water compensation which provides the heating effect of Mg melt. The values of these thermal properties were acquired from the temperature curves recorded with an *in-situ* data logger as the strip casting processed. From this result, it shows that the similar thermal properties were found at the same flow rate of cooling water although the temperatures were different.

The temperature of cooling water influences the initial state of melt flowing through twin rolls and the solid strip. The 21°C and above are the desired cooling water temperature to start the TRC process with in-house water circulation system. The flow rate of cooling water dominates the thermal properties of twin roll caster when the TRC process passes the initial state and strips are continuously cast. Higher flow rate of cooling water is desired to minimise the temperature rise on roll surface and maintain high temperature gradient for solidification.

Table 6.1 The thermal properties of twin roll caster at different inlet water temperatures with 655°C melt pouring temperature.

	Inlet water temp (°C)	Flow rate (L/min)	Pouring temp (°C)	Heating rate (°C/s)	Cooling rate (°C/s)
1	21	8	655	0.37	0.20
2	26	8	655	0.39	0.19

6.2. Parameter Optimization for Twin Roll Casting Process

The objective of this part of the research is to investigate the effect of processing parameters on the microstructure evolution and defect control of thin gauge Mg strip fabricated by twin roll casting process.

6.2.1. Pouring Temperature

Temperature of the melt at the nozzle of the tundish is a crucial factor in the conventional TRC process. It effects solidification of the melt and further influences the morphology and size of the solidified microstructure.

Figure 6.14 shows the microstructure of longitudinal section of AZ31 strip produced by the TRC process with different pouring temperatures with 50°C superheat, 20°C superheat and approximately 4°C below liquidus.

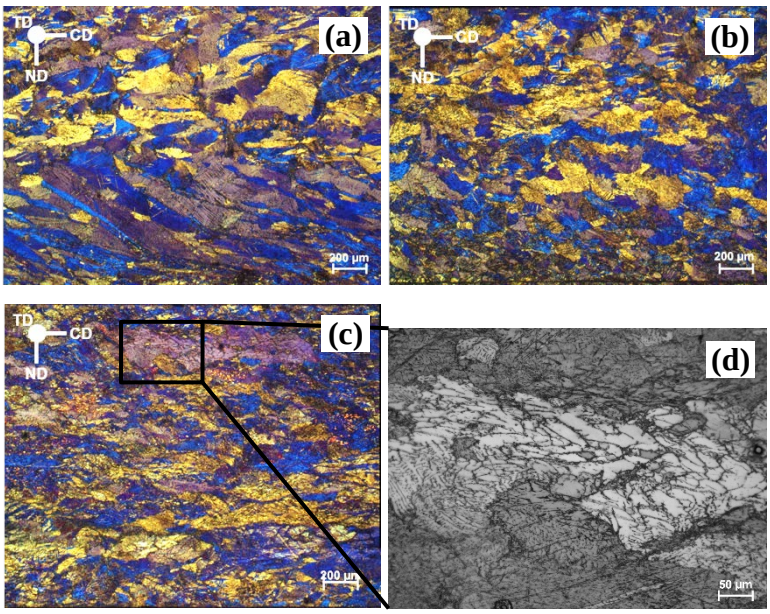

Figure 6.14 Microstructure of longitudinal section of AZ31 TRC strips with different pouring temperature by shoe tundish involved melt feeding system, (a) 680°C (1.647 mm thickness), (b) 650°C (1.650 mm thickness) and (c) 625°C (1.751 mm thickness) and its detailed morphology of rosettes structure by solidification in semi-solid state (d).

Large columnar grains of α-Mg are observed in **Figure 6.14**(a) with extra fine equiaxed grains on the edge of the chilled zone. With decreased melt temperature, the as-cast microstructure of AZ31 strip produced at 650°C had more equiaxed coarse grains along the thickness of TRC strip. The large rosette structure of α-Mg grain forms in the AZ31 strip (detailed in **Fig. 6.14**(d)) with a pouring temperature of 625°C. The α-Mg phase has elongated grains in the casting direction which is an indication of the deformation presented during TRC process. The thickness of steady state strip increase with the decreasing pouring temperature. The AZ31 alloy strip cast in the semi-solid state has a thickness of 1.751 mm which is higher than 1.650 mm at 650°C and 1.647 mm at 680°C. The lower melt temperature leads to an increased separation force in strip due to the early solidification result in higher strength in the TRC process, and is consistent with the deformed α-Mg grains in **Figure 6.14**(c).

Figure 6.15 shows the morphology of centre line segregation in the AZ31 TRC strip with different pouring temperatures. This solute rich zone in **Figure 6.15**(a) was in the middle of strip thickness along the casting direction. The large area of solute segregation forms during the solidification of columnar α-Mg grains. The low melting point liquid flows through the inter-grain areas and squeezed into the centre of the strip due to the compressive force of twin rolls. In the microstructure of strip poured at 650°C, the size of

centre line segregation reduced as the α-Mg grains tend to solidified in a equiaxed morphology. The microstructure contained a portion of solute elements that solidified locally and the size of the solute rich zone reduced. The typical morphology of $Mg_{17}Al_{12}$ in **Figure 6.15**(c) is indicated by white arrows. They are distributed along the grain boundary area with darker contrast. The formation of $Mg_{17}Al_{12}$ is related to the solidification of melt which completed before reaching the kissing point of twin rolls. Without the squeezing effect of twin roll on the melt solidification, the solute rich zone forms locally around the α-Mg grains.

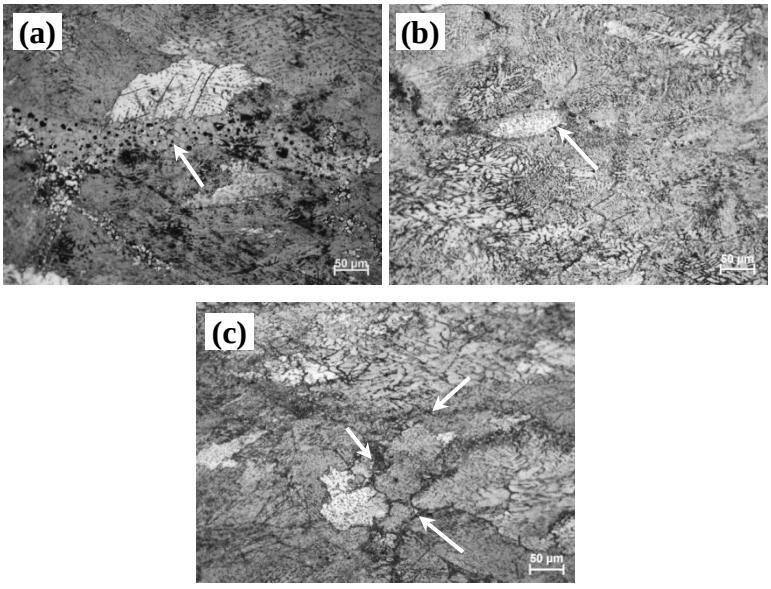

Figure 6.15 Microstructure of solute element rich phase in AZ31 TRC strip formed with different pouring temperature, (a) 680°C, (b) 650°C and (c) 625°C.

In addition to the microstructural differences, a high pouring temperature (680°C and above) provides some processing difficulties such as severe oxidation tendency on the strip surface (decrease the surface quality), the increased fire hazard (safety) and roll surface sticking (facility service life). On the other hand, a very low pouring temperature (below the AZ31 alloy liquidus) results in the early solidification of Mg melt and formation of rosettes structure which deteriorates the mechanical properties of strip, and in the worse situation, the solidified Mg could block the tundish tip, prevent the melt delivery and lead to experimental failure.

With the microstructural investigation and experimental consideration, a moderate pouring temperature of 650±10°C (~10-30°C superheat) was selected for further TRC/MC-TRC experiments on AZ31 alloy.

6.2.2. Roll Gap

The MC-TRC process with low pressure twin roll caster was designed for thin gauge Mg strip production with reduced basal texture for further applications in the electronics and automobile industries. The thin gauge MC-TRC strip is expected to undergo limited thermal mechanical processes for final shaped parts as the thickness reduction is already obtained during the strip casting process. The roll gap is the dominant parameter that controls the strip thickness amongst the major strip casting parameters.

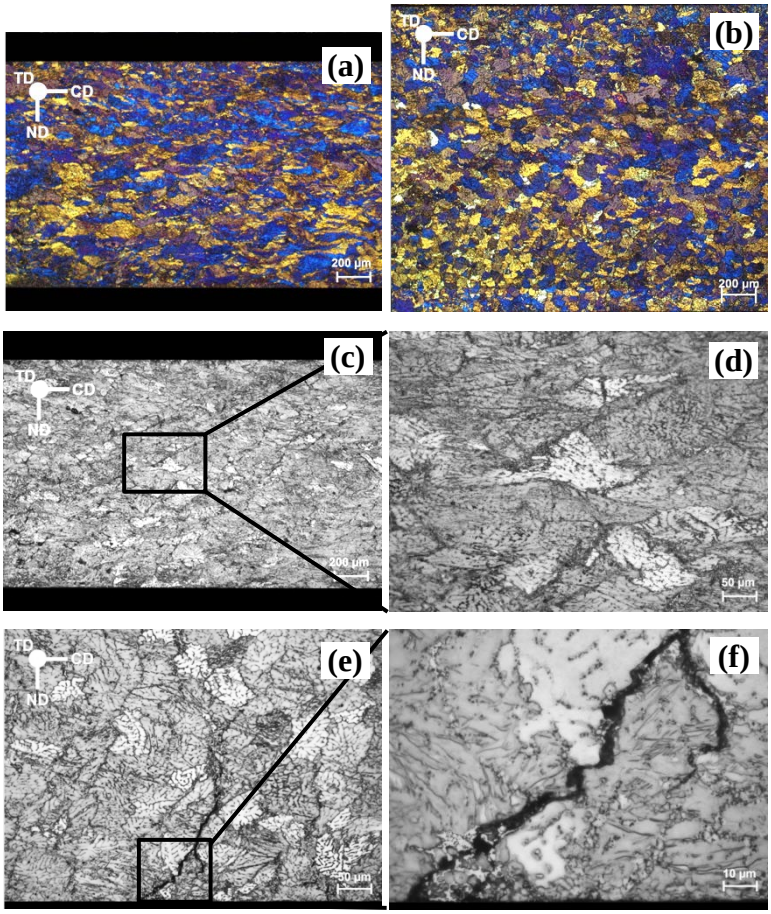

Figure 6.16 Microstructure of AZ31 MC-TRC strip using twin-screw high shear with different roll gap distance pouring at 650°C by integrated tundish with thermally controlled nozzle, (a), (c) and (d) 1.0 mm gap distance (1.367 mm thickness) and its detailed morphology, (b), (e) and (f) 1.2 mm gap distance (1.793 mm thickness) and surface crack.

Figure 6.16 shows the microstructure of AZ31 alloy strip produced through MC-TRC process with twin-screw treated ingot. 1.0 mm is the minimum roll gap of the in-house horizontal twin roll caster and 1.2 mm gap was used for comparison. In the microstructure of MC-TRC strip with 1.0 mm gap (**Fig. 6.16**(a)), thin strip with thickness of 1.367 mm was obtained with deformed α-Mg grains elongated along the casting direction. On the other hand, a fully equiaxed solidification structure was observed in the 1.793 mm

thickness strip produced with 1.2 mm gap, with the fine equiaxed grains distributed homogeneously through the thickness of strip. The investigation of solute segregation, show that the solute rich phases distributed locally around the elongated α-Mg grains (**Fig. 6.16**(c) & (d)) in the strip produced with 1.0 mm gap. The microstructure of strip produced with 1.2 mm gap show similar distribution of solute rich compounds inside strip. However, cracks were found at the top and bottom surface of strip in **Figure 6.16**(e). The crack path spread through the solute rich phases from surface into the strip as indicated by the high magnification micrograph (**Fig. 6.16**(f)).

The difference in microstructures of strip produced with different gaps is explained as the reduced deformation caused by the larger gap in the strip casting. **Figure 6.17** shows the schematic illustration of strip casting with different gap opening. When there is larger gap opening (**Fig. 6.17**(b)), the tip of tundish comes closer to the twin roll kissing point compared with the smaller gap (**Fig. 6.17**(a)) and led to a reduced setback. This geometrical change resulted in the variation in strip solidification on the twin roll surface. The solidification front of strip was closer to the kissing point of twin roll casting due to the setback reduction in the large gap. As a consequence, the deformation region of the solid strip reduced the large gap opening. These changes in the TRC process led to a solidification structure with limited deformation in the strip. With the small gap opening, higher deformation was applied to the strip that solidified early before it passed through a kissing point.

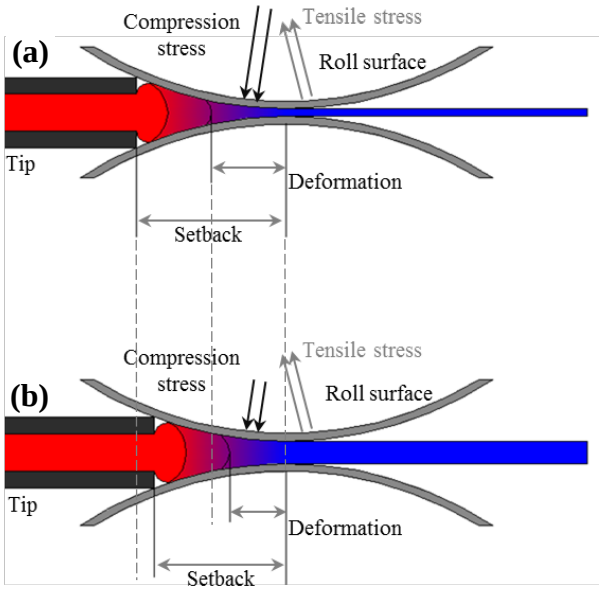

Figure 6.17 Schematic illustrating the influence of roll gap to strip microstructure with MC-TRC, (a) small gap, and (b) large gap.

From the stress analysis, it shows that the strips experienced of tensile and compression stress before and after the kissing point, respectively. The compression stress applied on the strip surface by the rolling force of the twin rolls. The higher compression stress seen with the small gap opening was attributed to the larger deformation region in the process route. The tensile stress on the strip was due to the roll surface sticking when it passes the kissing point of twin rolls and pulled out. With a small roll gap, the compression stress applied on the strip surface overcome the tensile stress and result in a closed strip surface with no cracks. In contrast, the tensile stress applied on the strip after the strip passes through the kissing point of twin rolls caused the appearance of surface cracks with limited deformation with the large roll gap opening.

Highly deformed structure is not desired in the Mg alloy strips due to the limited formability of magnesium. Surface cracks on the cast strip are fatal for the downstream thermal mechanical processes as these micro-cracks will act as crack initiation sites and cause defects on the final shaped products.

6.3. Melt Conditioned Twin Roll Casting Process with Rotor-stator Mixer and Twin-screw Device

The objective of this part of the research is to investigate the effect of high shear using the inline rotor-stator mixer and pre-treated ingot through twin-screw device on the microstructure evolution and defect control of the thin gauge Mg strip fabricated by melt conditioned twin roll casting process.

6.3.1. Melt Conditioned Twin Roll Casting Process with Rotor-stator Mixer Inline High Shear

Figure 6.18 shows the microstructure of as-cast AZ31 strips with TRC and rotor-stator mixer involved MC-TRC process. The schematic illustration of this MC-TRC process is shown in **Chapter 3**. A coarse columnar structure is observed in AZ31 strip with the TRC process (**Fig. 6.18**(a)). In contrast, fine and uniformly distributed α-Mg grains are observed in the MC-TRC processed sample (**Fig. 6.18**(b)). At higher magnifications, optical microstructure of TRC strip reveals coarse and thick centre line segregation with

different grey contrast (**Fig. 6.18**(c)). In comparison, the solute elements segregation was significantly reduced in the MC-TRC sample in **Figure 6.18**(d).

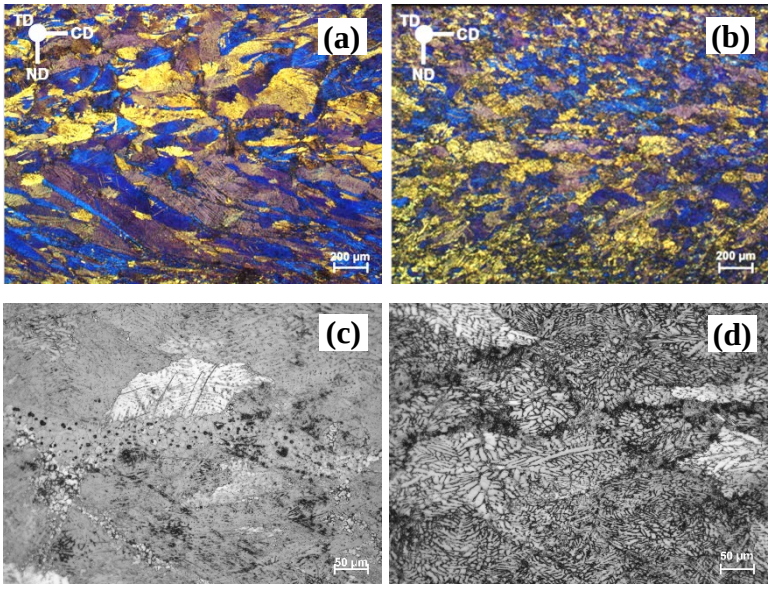

Figure 6.18 Microstructure of longitudinal section of AZ31 strips fabricated by (a) and (c) conventional TRC process, and (b) and (d) MC-TRC process by shoe tundish involved melt feeding system at 680°C.

The microstructure of MC-TRC sample has uniform equiaxed α-Mg grains that are significantly refined through the longitudinal section. The formation of the improved microstructure is attributed to the dispersion of fine MgO particles, which are the preferential sites for α-Mg nucleation during the solidification (Jiang 2013). The oxide films forms in the melt were aggregates of sub-micron sized MgO particles (Fan et al. 2009). During the melt conditioning process in the high shear chamber of steel tundish, these oxide films disintegrate into particles and disperse homogeneously in the melt through the high shear generated by the rotor-stator mixer. As the MgO/α-Mg interface is semi-coherent with a small crystallographic misfit, the uniformly distributed fine MgO particle acts as the heterogeneous nucleation sites during the solidification (Fan et al. 2009). Moreover, the dispersion of these films into discrete individual particles increased the heterogeneous nuclei density leading to improved nucleation efficiency (Quested, Greer 2004). Hence, the refined uniform microstructure of α-Mg was obtained in the strip by MC-TRC process.

The significantly reduced centre line segregation in the sample of MC-TRC strip can be attribute to heterogeneous nucleation that take place simultaneously through the longitudinal section as the melt touches the twin roll surface. The equiaxed solidification

supressed the solute squeezing to the centre of the strip and kept the solute rich phase locally around the α-Mg dendrites. On the other hand, solidification during the conventional TRC process was in the form of columnar α-Mg dendrite from roll surface (low temperature end) to the centre of the strip (high temperature end) against a thermal gradient. During such solidification of α-Mg phase pushed the solute to the centre of the strip through the inter-columnar region as a channel and thus lead to severe centre line segregation in the TRC strip in **Figure 6.18**(c).

6.3.2. Melt Conditioned Twin Roll Casting Process with High Sheared Ingot by Twin-screw Device

The research on the reliability of twin-screw treated ingot conducted by repeating the melt and cast same ingot to see if the grain refinement potency of high shear would disappear. **Figure 6.19** shows the microstructure of AZ31 alloy in different condition. An obvious grain refinement was achieved with twin-screw device comparing **Figure 6.19**(a) and (b). After that the high shear treated ingot was melted and recast, with the microstructures show in **Figure 6.19**(c). When compared with the freshly treated ingot (**Figure 6.19**(c)), the grain refinement of the remelted AZ31 alloy was retained and resulted in a reduced α-Mg grain size compared with conventional TRC AZ31 alloy.

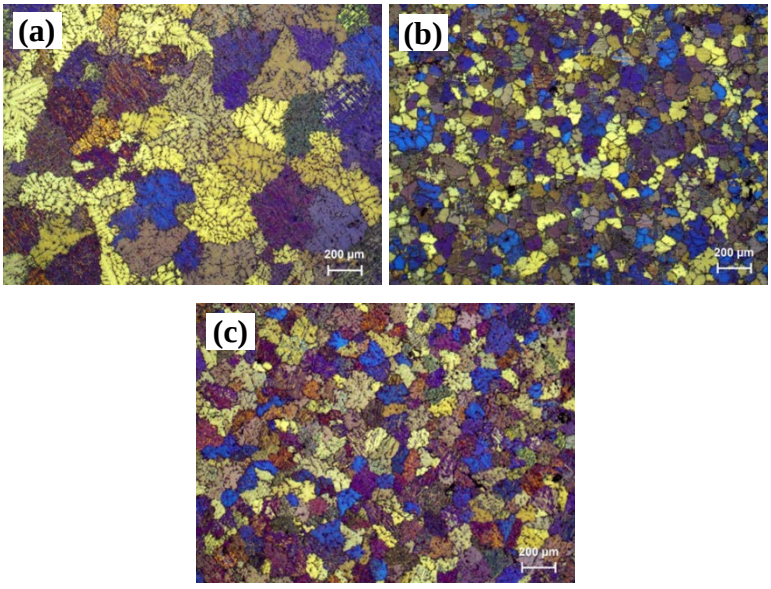

Figure 6.19 Grain size of AZ31 alloy melt-conditioned by twin screw high shear device, (a) before high shear treatment, (b) after high shear treatment, and (c) remelted from high shear treated AZ31 ingot.

The retention of grain refinement due to high shear treatment provided a variation of MC-TRC process through high shear treated alloy ingot instead of rotor-stator inline treatment.

This is the solution for the situation when the melt conditioning facilities are not accessible or the strip production line was not flexible to implement the melt conditioning facilities.

Figure 6.20 shows the polarized-light optical microstructures of AZ31 alloy taken from transvers section of the 1.7 mm thickness of TRC and MC-TRC strips. Fine equiaxed dendrites of α-Mg grains with an average grain size of 137.98±35.52 μm were observed in **Figure 6.20**(b) with a uniform distribution of grain size for the MC-TRC strips. In contrast, the coarse dendritic α-Mg grain and fluctuation of grain size were observed in the TRC only microstructure (**Fig. 6.20**(a)). The area near the strip surface show chilled fine equiaxed α-Mg grains, and the large α-Mg grains were found near the centre of TRC strip which show a decreased thermal gradient during solidification. The average grain size of the TRC strip is 249.11±106.11 μm.

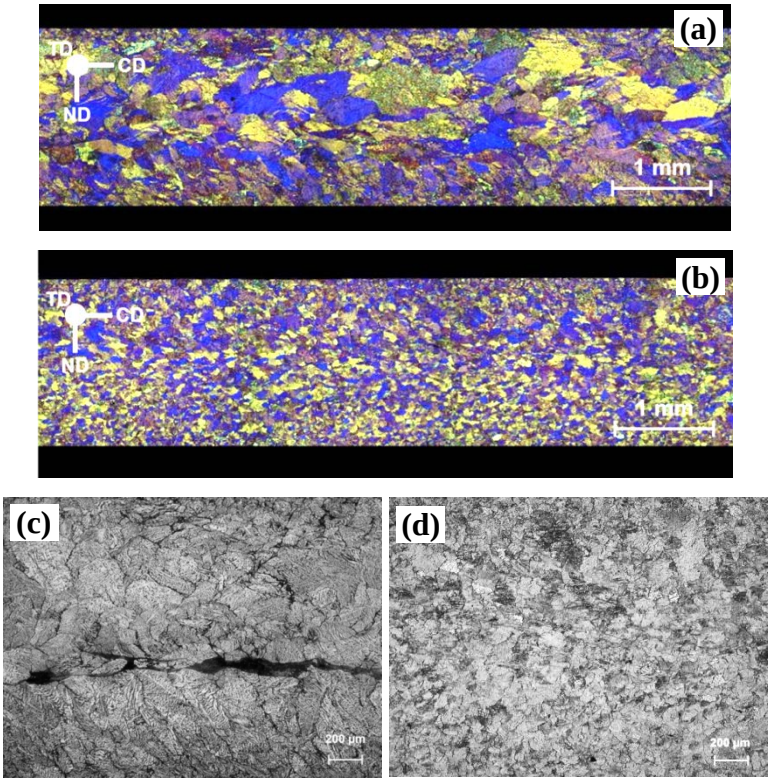

Figure 6.20 Microstructure of longitudinal section of AZ31 strips fabricated by (a) and (c) conventional TRC process, and (b) and (d) MC-TRC process by integrated tundish with thermally controlled nozzle with high shear treated AZ31 ingot at 650°C.

Figure 6.20(c) and (d) show the optical images of AZ31 alloy taken from longitudinal section of the TRC and MC-TRC strips. The optical microstructure, due to the different corrosion behaviour of different phases in AZ31 alloy to the etching solution, a significant

difference in contrast can be seen. The darker contrast in **Figure 6.20**(a) was found at the potential centre line segregation where the solute elements like Al, Mn and Zn are concentrated. Compared with TRC sample, the MC-TRC strip shows a more uniform and locally distributed micro-segregation. It suggests that with enhanced nucleation achieved during the strip solidification, the undercooling for the MC-TRC AZ31 alloy solidification is reduced and α-Mg grains nucleated at the roll surface and the centre of strip, the rejected solute atoms from solidification front is present at the inter-grain region rather than flow through large channels that form between coarse α-Mg grains along the solidification direction. Thus, the solutes are distributed locally surrounding the α-Mg grains and the centre line segregation of MC-TRC strip is reduced or suppressed.

6.3.3. Solidification Behaviour of Melt Conditioned Twin Roll Casting Process

Figure 6.21 illustrates the solidification mechanism during TRC and MC-TRC process. **Figure 6.21**(a) illustrates the columnar growth of α-Mg during the conventional TRC process, and **Figure 6.21**(b) presents the solidification of equiaxed α-Mg grain and eliminated centre line segregation.

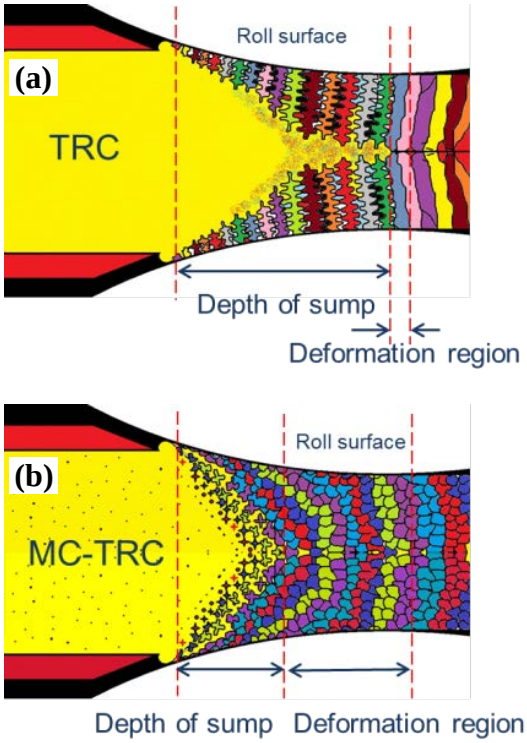

Figure 6.21 Schematic illustrating the solidification mechanism for (a) TRC and (b) MC-TRC process (Das, Barekar et al. 2015).

As discussed earlier, in the case of TRC columnar grains start forming near the roll surface towards the centre of the strip. These columnar grains reject the solutes towards the centre of the strip, which drops the liquidus temperature of the melt at the centre. This results in an increase in the sump depth as shown in **Figure 6.21**(a). Thus, the deformation region is significantly reduced during TRC process. On the other hand, in the case of MC-TRC process (**Fig. 6.21**(b)) heterogeneous nucleation through dispersion of oxide particles dominates the solidification.

It was established earlier that MgO particles are potent nuclei for α-Mg (Fan, Wang et al. 2009) with low crystal lattice misfit of 5.46% along the most closely packed directions $\langle 01\bar{1}\rangle_{\mathrm{MgO}}$ and $\langle 1\bar{2}10\rangle_{\mathrm{Mg}}$(**Fig. 6.22**). With the sufficiently potent nuclei of oxide particles involved in the solidification, the heterogonous nucleation of α-Mg phase is enhanced. This results in the advance of an equiaxed solidification front from the roll surface to the centre of the strip instead of columnar grain growth. The solute rejection towards the centre of the strip becomes insignificant and the sump depth is shorter in the case of MC-TRC compared with the TRC process (**Fig. 6.21**(b)). Thus, the deformation region extends as the sump depth decreases.

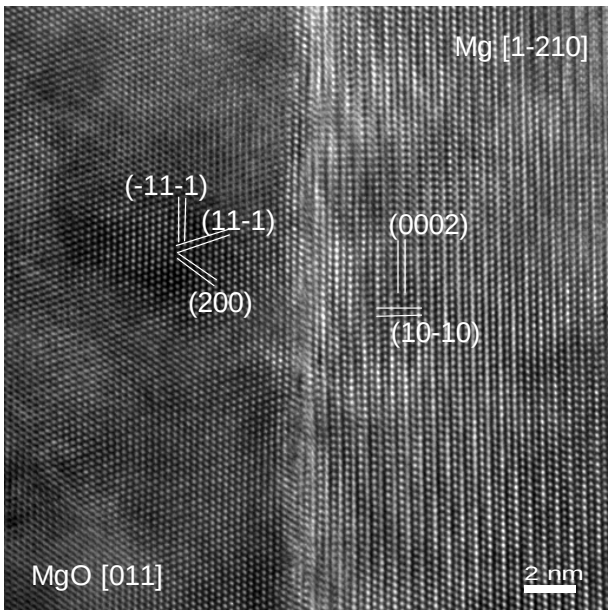

Figure 6.22 High-resolution TEM image of the interface between MgO and α-Mg, where a-Mg is viewed along [1$\bar{2}$10] direction and MgO is along [011] direction (Fan, Wang et al. 2009).

Chapter 7 Conclusions

1. The high shear treatment of SiC particle reinforced A356 alloy with varying SiC additions is proven to improve the uniformity of reinforcing particle distribution in as-cast A356/SiC_p composite samples by rotor-stator mixer compared with mechanically stirred composite samples. Higher treatment temperature provides more homogeneous reinforcement distribution and dispersion. The high shear rate and high shear stress provided by rotor-stator mixer breaks up particle agglomeration and lead to the particle dispersion.

2. The gas entrapment caused porosity of mechanically stirred A356/SiC_p composite slurries is reduced by the high shear treatment through the rotor-stator mixer. The high shear treated composite samples show a smaller deviation from theoretically determined density compared with mechanically stirred samples with SiC additions from 5wt% to 17wt% SiC_p. Such improvement in A356/SiC_p composites lead to an enhanced Brinell hardness and elastic modulus of high shear treated composites.

3. Based on the advantages of high shear treatment on the particle reinforcement distribution of MMCs, a two stage process for processing composite slurry involving conventional mechanical stirring followed by the rotor-stator mixer has been developed for producing Mg alloy based MMCs, and has been successfully used in the production of AZ31/5SiC_p composite strips using twin roll casting.

4. The composite TRC strip has a fine microstructure in the matrix with a uniform distribution of SiC particles, and enhanced modulus, yield strength and ductility, compared with that produced without high shear treatment. SiC particles act as heterogeneous nucleation sites for α-Mg, contributing to the observed grain refinement. The high cooling rate in the twin roll casting process partly contributed to the grain refinement of the matrix and uniform distribution of reinforcing particles globally.

5. With the refinement of α-Mg matrix observed in the AZ31/5SiC_p composite, two sets of crystallographic ORs between α-SiC (6H) and α-Mg were determined by comparing of Euler angles from EBSD indexed results. With the EBSD analysis in AZ31/5vol%SiC_p sample, these two sets of hcp-hcp ORs with limited inter-atomic

spacing misfit and the interplanar spacing mismatch has been experimentally identified. The crystallographic ORs confirm the double effects of silicon carbide on the AZ31/SiCp composite system and further provide a new crystallographic explanation for heterogeneous nucleation of α-Mg grain on α-SiC (6H) particles. These two reproducible crystallographic ORs are $[10\ \bar{1}\ 0]_{SiC}//[\ \bar{2}\ 113]_{Mg}$, $(0006)_{SiC}//(10\bar{1}1)_{Mg}$, $(1\bar{2}1\bar{6})_{SiC}//(\bar{2}20\bar{2})_{Mg}$ and $[01\bar{1}0]_{SiC}//[1\bar{1}00]_{Mg}$, $(0006)_{SiC}//(0002)_{Mg}$, $(\bar{2}110)_{SiC}//(11\bar{2}0)_{Mg}$.

6. Two processing methods with melt conditioning treatment have been developed for producing thin gauge Mg alloys using TRC. These processing methods are twin roll casting with inline melt conditioning treatment with a rotor-stator mixer and twin roll casting with melt conditioned ingot with a twin-screw device.

7. The strip produced by melt conditioned twin roll casting process shows refined dendrites with equiaxed α-Mg grains. Such significant grain refinement leads to elimination of solute segregation and further reduces the centre line segregation. With the melt conditioning process prior to the twin roll casting, heterogonous nucleation of α-Mg phase is enhanced by the dispersion of MgO particles which provides sufficient potent nuclei for refining of α-Mg matrix during the solidification, and MgO nucleating site and α-Mg matrix have reduced crystal lattice misfit of 5.46% along the most closely packed directions $\langle 01\bar{1}\rangle_{MgO}$ and $\langle 1\bar{2}10\rangle_{Mg}$.

Chapter 8 Suggestions for Future Work

In this thesis, the effect of high shear treatment on particle dispersion in MMCs and trace inoculant in Al and Mg alloys is discussed in order to evaluate the advantage of this newly developed process. The dispersion of SiC particles were examined in as-cast microstructures of A356/SiC_p and AZ31/5SiC_p composites prepared by mould casting and twin roll casting, respectively. The results shows that improved distribution of reinforcement was observed in both composites with increased mechanical properties. The two processes combining melt conditioning and twin roll casting for thin gauge Mg alloy strip was developed with the melt feeding system incorporating thermally controlled nozzle. The melt conditioned TRC strips show refined α-Mg grain size and reduced centre line segregation due to the enhanced heterogeneous nucleation of α-Mg matrix due to the dispersed potent nuclei of MgO. Furthermore, the double effects of SiC particle in Mg alloy as reinforcement and heterogeneous nuclei is revealed by determination of two reproducible crystallographic orientations between α-Mg and α-SiC (6H). From this study, engineering opportunities are seen for some metallurgical problems such as cost effective MMCs and direct-formable Mg TRC strip. However, to confirm the potential advantages to such applications, more in-depth understanding and industrial testing and downstream processing is needed.

Mechanical property and performance evaluation of final composite casting: The primary ingot properties are commonly related to the final casting product as the mechanical properties of final product could deviate after intermediating process due to the fairly long and complex processing route of casting. Based on this consideration, the casting parameter optimization for the composite slurry should be performed to obtain enhanced properties with well distributed reinforcement in the slurry.

Measurement methods of elastic modulus for composite materials: In this research, two major methods for elastic modulus measurement have been used for composites. However, the comparison of mechanical testing method and ultrasonic method hasn't been studied to reveal the accuracy, reliability and flexibility for different metal matrix composites

High resolution TEM observation of SiC/Mg interface: The crystallographic orientation relationship of SiC/Mg has been identified with the EBSD technique. High

resolution TEM observation could confirm the crystallographic orientation relationship of SiC/Mg interface coupled with systematic selected area diffraction analysis from the interface regions

The nucleation phenomenon in particle reinforced metal matrix composite: The discovery that α-SiC (6H) as the nucleation site of α-Mg grain by crystallographic analysis shows a research direction of solidification reveals that particle reinforced metal matrix composite rarely consider. The effect of grain refinement by reinforcement on the reinforcement distribution and mechanical properties could be utilised for particle/whisker/fibre reinforced metal matrix composites for further improvement.

The effect of melt conditioning on the downstream processes: The TRC strip of Mg alloy and Mg matrix composite with melt conditioning treatment has been produced. The effect of high shear treatment on both strips on the downstream processes is unclear. In this regard, further research on the heat treatment and deformation process should be conducted to provide full information of impact of melt conditioning on the strip/sheet products.

Reference

AGNEW, S.R., 2004. Wrought magnesium: A 21st century outlook. *JOM,* **56**(5), pp. 20-21.

AGNEW, S.R. and NIE, J.F., 2010. Preface to the viewpoint set on: The current state of magnesium alloy science and technology. *Scripta Materialia,* **63**(7), pp. 671-673.

ATIEMO-OBENG, V.A. and CALABRESE, R.V., 2004. Rotor–stator mixing devices. *Handbook of industrial mixing: Science and practice,* , pp. 479-505.

ATIEMO-OBENG, V.A., PENNEY, W.R. and ARMENANTE, P., 2004. Solid–liquid mixing. *Handbook of industrial mixing: Science and practice,* , pp. 543-584.

AYERS, G. and FLETCHER, L., 1998. Review of the thermal conductivity of graphite-reinforced metal matrix composites. *Journal of Thermophysics and Heat Transfer,* **12**(1), pp. 10-16.

BABU, N.H., FAN, Z. and ESKIN, D.G., 2013. Application of External Fields to Technology of Metal-Matrix Composite Materials. *TMS2013 Supplemental Proceedings,* , pp. 1037-1044.

BAKSHI, S., LAHIRI, D. and AGARWAL, A., 2010. Carbon nanotube reinforced metal matrix composites-a review. *International Materials Reviews,* **55**(1), pp. 41-64.

BANERJI, A. and REIF, W., 1986. Development of Al-Ti-C grain refiners containing TiC. *Metallurgical Transactions A,* **17**(12), pp. 2127-2137.

BARAILLER, F., HENICHE, M. and TANGUY, P.A., 2006. CFD analysis of a rotor-stator mixer with viscous fluids. *Chemical engineering science,* **61**(9), pp. 2888-2894.

BAREKAR, N. and DHINDAW, B., 2014. Twin-roll casting of aluminum alloys–An overview. *Materials and Manufacturing Processes,* **29**(6), pp. 651-661.

BAREKAR, N., TZAMTZIS, S., BABU, N.H., FAN, Z. and DHINDAW, B., 2009. Processing of ultrafine-size particulate metal matrix composites by advanced shear technology. *Metallurgical and Materials Transactions A,* **40**(3), pp. 691-701.

BAYANDORIAN, I., HUANG, Y., FAN, Z., PAWAR, S., ZHOU, X. and THOMPSON, G., 2012. The impact of melt-conditioned twin-roll casting on the downstream processing of an AZ31 magnesium alloy. *Metallurgical and Materials Transactions A,* **43**(3), pp. 1035-1047.

BAYANDORIAN, I., HUANG, Y., SCAMANS, G.M. and FAN, Z.Y., 2011. Magnesium alloy strip produced by a melt-conditioned twin roll casting process, *Materials Science Forum* 2011, Trans Tech Publ, pp. 129-132.

BAYANDORIAN, I., 2010. *Magnesium alloy strip produced by a melt-conditioned twin roll casting process*, Brunel University London.

BERG, B.S., HANSEN, V., ZAGIERSKI, P.T., NEDREBERG, M.L., OLSEN, A. and GJØNNES, J., 1995. Advanced Materials and Technologies Gauge reduction in Twin-Roll Casting of an AA5052 aluminium alloy: The effects on microstructure. *Journal of Materials Processing Technology,* **53**(1), pp. 65-74.

BIRKS, A.S., GREEN, R.E. and MACINTIRE, P., 1991. *ASNT Nondestructive Testing Handbook: Ultrasonic Testing.* American Society for Nondestructive Testing, American Society for Metals.

BIROL, Y., 2007. Production of Al–Ti–B master alloys from Ti sponge and KBF4. *Journal of Alloys and Compounds,* **440**(1–2), pp. 108-112.

BORGONOVO, C. and APELIAN, D., 2011. Manufacture of Aluminum Nanocomposites: A Critical Review, *Materials Science Forum* 2011, Trans Tech Publ, pp. 1-22.

BRADBURY, P., 1994. *A mathematical model for the twin roll casting process*, University of Oxford.

BUNGE, H.-J., 1982. *Texture analysis in materials science*, Butterworths, London

CAI, Y., TAPLIN, D., TAN, M.J. and ZHOU, W., 1999. Nucleation phenomenon in SiC particulate reinforced magnesium composite. *Scripta Materialia,* **41**(9), pp. 967-971.

CAPITANI, G.C., DI PIERRO, S. and TEMPESTA, G., 2007. The 6H-SiC structure model: Further refinement from SCXRD data from a terrestrial moissanite. *American Mineralogist,* **92**(2-3), pp. 403-407.

CAULFIELD, T. and TIEN, J., 1989. High temperature reaction zone growth in tungsten fiber reinforced superalloy composites: Part I. Application of the moving boundary equations. *Metallurgical Transactions A,* **20**(2), pp. 255-266.

CHAWLA, N. and CHAWLA, K., 2006. Metal-matrix composites in ground transportation. *JOM,* **58**(11), pp. 67-70.

CHENG, Z. and REDNER, S., 1990. Kinetics of fragmentation. *Journal of Physics A: Mathematical and General,* **23**(7), pp. 1233.

CHOU, T., KELLY, A. and OKURA, A., 1985. Fibre-reinforced metal-matrix composites. *Composites,* **16**(3), pp. 187-206.

CLYNE, T. and WITHERS, P., 1995. *An introduction to metal matrix composites.* Cambridge University Press.

COLE, G. and SHERMAN, A., 1995. Light weight materials for automotive applications. *Materials Characterization,* **35**(1), pp. 3-9.

CULPIN, M., 1957. The viscosity of liquid magnesium and liquid calcium. *Proceedings of the Physical Society.Section B,* **70**(11), pp. 1079.

DAHLE, A., NOGITA, K., MCDONALD, S., DINNIS, C. and LU, L., 2005. Eutectic modification and microstructure development in Al–Si Alloys. *Materials Science and Engineering: A,* **413**, pp. 243-248.

DAS, K., BANDYOPADHYAY, T. and DAS, S., 2002. A review on the various synthesis routes of TiC reinforced ferrous based composites. *Journal of Materials Science,* **37**(18), pp. 3881-3892.

DAS, S., BAREKAR, N.S., EL FAKIR, O., WANG, L., PRASADA RAO, A.K., PATEL, J.B., KOTADIA, H.R., BHAGURKAR, A., DEAR, J.P. and FAN, Z., 2015. Effect of melt conditioning on heat treatment and mechanical properties of AZ31 alloy strips produced by twin roll casting. *Materials Science and Engineering: A,* **620**, pp. 223-232.

DIERINGA, H., 2011. Properties of magnesium alloys reinforced with nanoparticles and carbon nanotubes: a review. *Journal of Materials Science,* **46**(2), pp. 289-306.

DOUGLAS, J.F., GASIOREK, J.M., SWAFFIELD, J.A. and JACK, L.B., 2011. *Fluid Mechanics sixth edition.* Essex: Pearson Education Limited.

EASTON, M.A., SCHIFFL, A., YAO, J. and KAUFMANN, H., 2006. Grain refinement of Mg–Al (–Mn) alloys by SiC additions. *Scripta Materialia,* **55**(4), pp. 379-382.

EASTON, M. and STJOHN, D., 1999. Grain refinement of aluminum alloys: Part I. The nucleant and solute paradigms—a review of the literature. *Metallurgical and Materials Transactions A,* **30**(6), pp. 1613-1623.

EDWARDS, M.F. and BAKER, M.R., 1992. Chapter 7 - A review of liquid mixing equipment. In: N. HARNBY, , M.F. EDWARDS, , and A.W. NIENOW, eds, *Mixing in the Process Industries (Second Edition).* Oxford: Butterworth-Heinemann, pp. 118-136.

FAN, Z., WANG, Y., XIA, M. and ARUMUGANATHAR, S., 2009. Enhanced heterogeneous nucleation in AZ91D alloy by intensive melt shearing. *Acta Materialia*, **57**(16), pp. 4891-4901.

FAN, Z., XIA, M., ZHANG, H., LIU, G., PATEL, J., BIAN, Z., BAYANDORIAN, I., WANG, Y., LI, H. and SCAMANS, G., 2009. Melt conditioning by advanced shear technology (MCAST) for refining solidification microstructures. *International Journal of Cast Metals Research*, **22**(1-4), pp. 103-107.

FAN, Z.Y., ZUO, Y.B. and JIANG, B., 2011. A new technology for treating liquid metals with intensive melt shearing, *Materials Science Forum* 2011, Trans Tech Publ, pp. 141-144.

FAN, Z., 2013. An epitaxial model for heterogeneous nucleation on potent substrates. *Metallurgical and Materials Transactions A,* **44**(3), pp. 1409-1418.

FAN, Z., WANG, Y., ZHANG, Y., QIN, T., ZHOU, X.R., THOMPSON, G.E., PENNYCOOK, T. and HASHIMOTO, T., 2015. Grain refining mechanism in the Al/Al–Ti–B system. *Acta Materialia,* **84**, pp. 292-304.

FARBENINDUSTRIE, I.G., 1931. British Patent GB359,425.

FERRY, M., 2006. *Direct strip casting of metals and alloys.* Woodhead Publishing.

FLEMINGS, M.C., 1991. Behavior of metal alloys in the semisolid state. *Metallurgical Transactions A,* **22**(5), pp. 957-981.

FOWLER, K.A., ELFBAUM, G.M., and NELLIGAN, T.J., http://www.olympus-ims.com/en/resources/white-papers/theory-and-application-of-precious-ultrasonic-thickness-gaging/

GARG, G., ZSCHETZSCHE, J., SIMMCHEN, E., SCHAPER, M., FUESSEL, U. and PANDEY, S., 2007. Arc brazing of magnesium alloy AZ31 with steel (DX 53 Z), K. KAINER, ed. In: *Proceedings of the 7th International Conference on Magnesium* 2007, Wiley-VCH, Weinheim, pp. 901-908.

GONI, J., MITXELENA, I. and COLETO, J., 2000. Development of low cost metal matrix composites for commercial applications. *Materials science and technology*, **16**(7-8), pp. 743-746.

GREER, A.L., BUNN, A.M., TRONCHE, A., EVANS, P.V. and BRISTOW, D.J., 2000. Modelling of inoculation of metallic melts: application to grain refinement of aluminium by Al–Ti–B. *Acta Materialia,* **48**(11), pp. 2823-2835.

GÜNTHER, R., HARTIG, C. and BORMANN, R., 2006. Grain refinement of AZ31 by (SiC)P: Theoretical calculation and experiment. *Acta Materialia,* **54**(20), pp. 5591-5597.

GUPTA, M., MOHAMED, F., LAVERNIA, E. and SRIVATSAN, T.S., 1993. Microstructural evolution and mechanical properties of SiC/Al2O3 particulate-reinforced spray-deposited metal-matrix composites. *Journal of Materials Science,* **28**(8), pp. 2245-2259.

GUTH, E. and SIMHA, R., 1936. Untersuchungen über die viskosität von suspensionen und lösungen. 3. über die viskosität von kugelsuspensionen. *Colloid & Polymer Science,* **74**(3), pp. 266-275.

HAGA, T. and SUZUKI, S., 2003. A twin-roll caster to cast clad strip. *Journal of Materials Processing Technology,* **138**(1), pp. 366-371.

HAGA, T. and TAKAHASHI, K., 2004. Casting of composite strip using a twin roll caster. *Journal of Materials Processing Technology,* **157**, pp. 701-705.

HAGA, T., TAKAHASHI, K., WATARI, H. and KUMAI, S., 2007. Casting of wire-inserted composite aluminum alloy strip using a twin roll caster. *Journal of Materials Processing Technology,* **192**, pp. 108-113.

HALPIN, J.C., 1984. *Primer on composite materials: Analysis.* Lancaster, PA: Technomic Publ, pp. 130.

HAN, Y., LI, K., WANG, J., SHU, D. and SUN, B., 2005. Influence of high-intensity ultrasound on grain refining performance of Al–5Ti–1B master alloy on aluminium. *Materials Science and Engineering: A,* **405**(1–2), pp. 306-312.

HANSEN, S., KHAKHAR, D. and OTTINO, J., 1998. Dispersion of solids in nonhomogeneous viscous flows. *Chemical engineering science,* **53**(10), pp. 1803-1817.

HASHIM, J., LOONEY, L. and HASHMI, M., 1999. Metal matrix composites: production by the stir casting method. *Journal of Materials Processing Technology,* **92**, pp. 1-7.

HASHIM, J., LOONEY, L. and HASHMI, M.S.J., 2002a. Particle distribution in cast metal matrix composites—Part I. *Journal of Materials Processing Technology,* **123**(2), pp. 251-257.

HASHIM, J., LOONEY, L. and HASHMI, M.S.J., 2002b. Particle distribution in cast metal matrix composites—Part II. *Journal of Materials Processing Technology,* **123**(2), pp. 258-263.

HENDRICKS, C., 1994. Strip casting technology--a revolution in the steel industry? *Metall.Plant Technol.Int.(Germany),* **18**(3), pp. 42-44.

HIDNERT, P. and PEFFER, E. L., 1950. *Density of solid and liquids*. National Bureau of Standards Circular 487.

HOOKER, J. and DOORBAR, P., 2000. Metal matrix composites for aeroengines. *Materials science and technology,* **16**(7-8), pp. 725-731.

HUANG, Y., KAINER, K.U. and HORT, N., 2011. Mechanism of grain refinement of Mg–Al alloys by SiC inoculation. *Scripta Materialia,* **64**(8), pp. 793-796.

HURRICKS, P.L., 1973. Some metallurgical factors controlling the adhesive and abrasive wear resistance of steels. A review. *Wear,* **26**(3), pp. 285-304.

IBRAHIM, I., MOHAMED, F. and LAVERNIA, E., 1991. Particulate reinforced metal matrix composites—a review. *Journal of Materials Science,* **26**(5), pp. 1137-1156.

ISRAELACHVILI, J. and TABOR, D., 1973. Van der Waals forces: theory and experiment. *Progress in Surface and Membrane Science,* **7**(1), pp. 1-55.

JIANG, B., 2013. *Solidification behaviour of magnesium alloys*, Brunel University London.

JONES, R., POLLOCK, H.M., GELDART, D. and VERLINDEN, A., 2003. Inter-particle forces in cohesive powders studied by AFM: effects of relative humidity, particle size and wall adhesion. *Powder Technology,* **132**(2–3), pp. 196-210.

JURETZKO, F.R., STEFANESCU, D.M., DHINDAW, B.K., SEN, S. and CURRERI, P.A., 1998. Particle engulfment and pushing by solidifying interfaces: Part 1. Ground experiments. *Metallurgical and Materials Transactions A,* **29**(6), pp. 1691-1696.

KARNEZIS, P., DURRANT, G., CANTOR, B. and PALMIERE, E., 1995. Mechanical properties and microstructure of twin roll cast Al–7Si/SiCp MMCs. *Materials science and technology,* **11**(8), pp. 741-752.

KENDALL, K., 1988. AGGLOMERATE STRENGTH. *Powder Metallurgy,* **31**(1), pp. 28-31.

KOK, M., 2005. Production and mechanical properties of Al 2 O 3 particle-reinforced 2024 aluminium alloy composites. *Journal of Materials Processing Technology,* **161**(3), pp. 381-387.

KUHN, H., 2012. *Powder metallurgy processing: the techniques and analyses.* Elsevier.

KUMAR, G.V., RAO, C. and SELVARAJ, N., 2011. Mechanical and tribological behavior of particulate reinforced aluminum metal matrix composites–a review. *Journal of Minerals and Materials Characterization and Engineering*, **10**(01), pp. 59.

LASER, T., NÜRNBERG, M.R., JANZ, A., HARTIG, C., LETZIG, D., SCHMID-FETZER, R. and BORMANN, R., 2006. The influence of manganese on the microstructure and mechanical properties of AZ31 gravity die cast alloys. *Acta Materialia*, **54**(11), pp. 3033-3041.

LEE, J. and LEE, D.N., 2008. Texture control and grain refinement of AA1050 Al alloy sheets by asymmetric rolling. *International Journal of Mechanical Sciences*, **50**(5), pp. 869-887.

LELITO, J., ZAK, P.L., SHIRZADI, A.A., GREER, A.L., KRAJEWSKI, W.K., SUCHY, J.S., HABERL, K. and SCHUMACHER, P., 2012. Effect of SiC reinforcement particles on the grain density in a magnesium-based metal–matrix composite: Modelling and experiment. *Acta Materialia*, **60**(6–7), pp. 2950-2958.

LENEL, F.V., 1980. *Powder metallurgy: principles and applications.* Metal Powder Industry.

LI, J. and HUANG, Y., 2014. Microstructure and mechanical properties of an Mg-3Zn-o. 5Zr-5HA nanocomposite processed by ECAE, *IOP Conference Series: Materials Science and Engineering* 2014, IOP Publishing, pp. 012112.

LIANG, D. and COWLEY, C., 2004. The twin-roll strip casting of magnesium. *JOM*, **56**(5), pp. 26-28.

LIU, S., LIU, L. and KANG, L., 2008. Refinement role of electromagnetic stirring and strontium in AZ91 magnesium alloy. *Journal of Alloys and Compounds*, **450**(1), pp. 546-550.

LLOYD, D., 1994. Particle reinforced aluminium and magnesium matrix composites. *International Materials Reviews*, **39**(1), pp. 1-23.

LLOYD, D., 1989. The solidification microstructure of particulate reinforced aluminium/SiC composites. *Composites Science and Technology*, **35**(2), pp. 159-179.

LLOYD, D. and DEWING, E., 1988. Stability of SiC in molten aluminium, *Proc. Int. Symp. Advanced Structural Materials* 1988, pp. 71-77.

LLOYD, D. and JIN, I., 1988. A method of assessing the reactivity between SiC and molten AI. *Metallurgical and Materials Transactions A*, **19**(12), pp. 3107-3109.

LOGSDON, W. and LIAW, P.K., 1986. Tensile, fracture toughness and fatigue crack growth rate properties of silicon carbide whisker and particulate reinforced aluminum metal matrix composites. *Engineering Fracture Mechanics*, **24**(5), pp. 737-751.

MANAS-ZLOCZOWER, I., 2012. *Mixing and compounding of polymers: theory and practice.* Carl Hanser Verlag GmbH Co KG.

MATHUR, P., APELIAN, D. and LAWLEY, A., 1989. Analysis of the spray deposition process. *Acta Metallurgica*, **37**(2), pp. 429-443.

MAXWELL, I. and HELLAWELL, A., 1975. A simple model for grain refinement during solidification. *Acta Metallurgica,* **23**(2), pp. 229-237.

MCCARTNEY, D., 1989. Grain refining of aluminium and its alloys using inoculants. *International Materials Reviews,* **34**(1), pp. 247-260.

MEHRABIAN, R., RIEK, R. and FLEMINGS, M., 1974. Preparation and casting of metal-particulate non-metal composites. *Metallurgical Transactions,* **5**(8), pp. 1899-1905.

MEN, H., JIANG, B. and FAN, Z., 2010a. Mechanisms of grain refinement by intensive shearing of AZ91 alloy melt. *Acta Materialia,* **58**(19), pp. 6526-6534.

MERCHANT, H., KATTAMIS, T. and MORRIS, J., 1989. H. MERCHANT, D. TAYLOR and E. CHIA, eds. In: *Continuous Casting of Non Ferrous Metals and Alloys* 1989, TMS, Warrendale, PA, pp. 1-66.

MIRACLE, D., 2005. Metal matrix composites–from science to technological significance. *Composites Science and Technology,* **65**(15), pp. 2526-2540.

MOHANTY, P. and GRUZLESKI, J., 1994. Grain refinement of aluminium by TiC. *Scripta metallurgica et materialia,* **31**(2), pp. 179-184.

MORTENSEN, A., 1991. Interfacial phenomena in the solidification processing of metal matrix composites. *Materials Science and Engineering: A,* **135**, pp. 1-11.

MORTENSEN, A., MASOUNAVE, J. and HAMEL, F., 1990. Fabrication of particulates reinforced metal composites. *Mosounave and FG Hammel, eds., AST INTRENATIONAL, Materials Park, OH,* , pp. 217-233.

MURTY, B., KORI, S. and CHAKRABORTY, M., 2013. Grain refinement of aluminium and its alloys by heterogeneous nucleation and alloying. *International Materials Reviews,* .

NAIR, S., TIEN, J. and BATES, R., 1985. SiC-reinforced aluminium metal matrix composites. *International Metals Reviews,* **30**(1), pp. 275-290.

NARDONE, V. and PREWO, K., 1986. On the strength of discontinuous silicon carbide reinforced aluminum composites. *Scripta Metallurgica,* **20**(1), pp. 43-48.

NELSON, C.E., 1948. Grain size behavior in magnesium casting alloys. *Trans AFS,* **56**, pp. 1e23.

NIENOW, A.W., EDWARDS, M. and HARNBY, N., 1997. *Mixing in the process industries.* Butterworth-Heinemann.

NORMAN, A.F., PRANGNELL, P.B. and MCEWEN, R.S., 1998. The solidification behaviour of dilute aluminium–scandium alloys. *Acta Materialia,* **46**(16), pp. 5715-5732.

OH, S., CORNIE, J. and RUSSELL, K., 1989. Wetting of ceramic particulates with liquid aluminum alloys: Part II. Study of wettability. *Metallurgical transactions A,* **20**(3), pp. 533-541.

OLYMPUS, http://www.olympus-ims.com/en/applications/elastic-modulus-measurement/.

ORSATO, R.J. and WELLS, P., 2007. U-turn: the rise and demise of the automobile industry. *Journal of Cleaner Production,* **15**(11), pp. 994-1006.

PARK, S.S., PARK, W., KIM, C., YOU, B. and KIM, N.J., 2009. The twin-roll casting of magnesium alloys. *JOM,* **61**(8), pp. 14-18.

PATEL, J., ZUO, Y., FAN, Z., KRANE, M., JARDY, A., WILLIAMSON, R. and BEAMAN, J., 2013. Liquid metal engineering by application of intensive melt shearing, *Proceedings of the 2013 International Symposium on Liquid Metal Processing and Casting, TMS 2013* 2013, pp. 291-299.

PHILIP, D., 1982. *Engineering properties of steels.* Ohio, USA: ASM International.

POLMEAR, I. and JOHN, D.S., 2005. *Light alloys: from traditional alloys to nanocrystals.* Butterworth-Heinemann.

QIU, D., ZHANG, M. and KELLY, P.M., 2009. Crystallography of heterogeneous nucleation of Mg grains on Al 2 Y nucleation particles in an Mg–10wt.% Y alloy. *Scripta Materialia,* **61**(3), pp. 312-315.

QUESTED, T. and GREER, A., 2004. The effect of the size distribution of inoculant particles on as-cast grain size in aluminium alloys. *Acta materialia,* **52**(13), pp. 3859-3868.

RAHIMIAN, M., EHSANI, N., PARVIN, N. and REZA BAHARVANDI, H., 2009. The effect of particle size, sintering temperature and sintering time on the properties

of Al–Al 2 O 3 composites, made by powder metallurgy. *Journal of Materials Processing Technology,* **209**(14), pp. 5387-5393.

RAWAL, S.P., 2001. Metal-matrix composites for space applications. *JOM,* **53**(4), pp. 14-17.

REDNER, S., 1990. Fragmentation. *Statistical models for the fracture of disordered media,* , pp. 321-348.

ROHATGI, P., ASTHANA, R. and DAS, S., 1986. Solidification, structures, and properties of cast metal-ceramic particle composites. *International metals reviews,* **31**(1), pp. 115-139.

RUMPF, H., 1962. The strength of granules and agglomerates. In: W.A. KNEPPER, ed, *Agglomeration.* New York, U. S. A.: Wiley, pp. 379-418.

RUMPF, H., 2012. *Particle technology.* Springer Science & Business Media.

RUMPF, H., 1974. Die wissenschaft des agglomerierens. *Chemie Ingenieur Technik,* **46**(1), pp. 1-11.

RWEI, S., MANAS-ZLOCZOWER, I. and FEKE, D., 1990. Observation of carbon black agglomerate dispersion in simple shear flows. *Polymer Engineering & Science,* **30**(12), pp. 701-706.

SCHNEIDER, W., KEARNS, M., MCGARRY, M. and WHITEHEAD, A., 1998. A COMPARISON OF THE BEHAVIOUR OF AlTiC GRAIN REFINERS. *LIGHT METALS-WARRENDALE-,* , pp. 953-962.

SCHUBERT, H., 1979. Grundlagen des agglomerierens. *Chemie Ingenieur Technik,* **51**(4), pp. 266-277.

SHOROWORDI, K.M., LAOUI, T., HASEEB, A.S.M.A., CELIS, J.P. and FROYEN, L., 2003. Microstructure and interface characteristics of B4C, SiC and Al2O3 reinforced Al matrix composites: a comparative study. *Journal of Materials Processing Technology,* **142**(3), pp. 738-743.

SREEKUMAR, V., BABU, N.H., ESKIN, D. and FAN, Z., 2015. Structure–property analysis of *in-situ* Al–MgAl 2 O 4 metal matrix composites synthesized using ultrasonic cavitation. *Materials Science and Engineering: A,* **628**, pp. 30-40.

STJOHN, D.H., QIAN, M., EASTON, M.A., CAO, P. and HILDEBRAND, Z., 2005. Grain refinement of magnesium alloys. *Metallurgical and Materials Transactions A,* **36**(7), pp. 1669-1679.

STJOHN, D., CAO, P., QIAN, M. and EASTON, M., 2013. A brief history of the development of grain refinement technology for cast magnesium alloys. *Magnesium Technology*, , pp. 1-8.

STJOHN, D., EASTON, M., QIAN, M. and TAYLOR, J., 2013. Grain refinement of magnesium alloys: a review of recent research, theoretical developments, and their application. *Metallurgical and materials transactions A*, **44**(7), pp. 2935-2949.

STONE, H.A., 1994. Dynamics of drop deformation and breakup in viscous fluids. *Annual Review of Fluid Mechanics*, **26**(1), pp. 65-102.

SUKUMARAN, K., PILLAI, S., PILLAI, R., KELUKUTTY, V., PAI, B., SATYANARAYANA, K. and RAVIKUMAR, K., 1995. The effects of magnesium additions on the structure and properties of Al-7 Si-10 SiCp composites. *Journal of Materials Science*, **30**(6), pp. 1469-1472.

SURAPPA, M., 2003. Aluminium matrix composites: Challenges and opportunities. *Sadhana*, **28**(1-2), pp. 319-334.

TAMURA, Y., HAITANI, T., YANO, E., MOTEGI, T., KONO, N. and SATO, E., 2002. Grain refinement of high-purity Mg-Al alloy ingots and influences of minor amounts of iron and manganese on cast grain size. *Materials Transactions*, **43**(11), pp. 2784-2788.

TAMURA, Y., MOTEGI, T., KONO, N. and SATO, E., 2000. Effect of minor elements on grain size of Mg-9% Al alloy, *Materials science forum* 2000, Trans Tech Publ, pp. 199-204.

TANG, H., WROBEL, L. and FAN, Z., 2003. Fluid flow aspects of twin-screw extruder process: numerical simulations of TSE rheomixing. *Modelling and Simulation in Materials Science and Engineering*, **11**(5), pp. 771.

TANG, Y., LIU, H., ZHAO, H., LIU, L. and WU, Y., 2008. Friction and wear properties of copper matrix composites reinforced with short carbon fibers. *Materials & Design*, **29**(1), pp. 257-261.

TANG, H., WROBEL, L.C. and FAN, Z., 2004. Numerical evaluation of immiscible metallic Zn–Pb binary alloys in shear-induced turbulent flow. *Materials Science and Engineering: A*, **365**(1–2), pp. 325-329.

THOMAS, P., 2003. Continuous casting of aluminium alloys. *Solidification and Casting*, , pp. 26-47.

TOMAS, J., 2007. Adhesion of ultrafine particles—a micromechanical approach. *Chemical Engineering Science*, **62**(7), pp. 1997-2010.

TOMAS, J. and SCHUBERT, H., 1982. Modelling of the strength and the flow properties of moist soluble bulk materials. *Aufbereit Tech*, **23**(9), pp. 507-515.

TORRALBA, J., DA COSTA, C. and VELASCO, F., 2003. P/M aluminum matrix composites: an overview. *Journal of Materials Processing Technology*, **133**(1), pp. 203-206.

TRONCHE, A., VANDYOUSSEFI, M. and GREER, A., 2002. Instability of TiC particles in aluminium melts inoculated with an Al-Ti-C grain refiner. *Materials science and technology*, **18**(10), pp. 1072-1078.

TZAMTZIS, S., BAREKAR, N., BABU, N.H., PATEL, J., DHINDAW, B. and FAN, Z., 2009. Processing of advanced Al/SiC particulate metal matrix composites under intensive shearing–A novel Rheo-process. *Composites Part A: Applied Science and Manufacturing*, **40**(2), pp. 144-151.

UNDERWOOD, E., 1970. *Quantitative stereology*. Addison-wesley publishing company.

UTOMO, A., BAKER, M. and PACEK, A., 2009. The effect of stator geometry on the flow pattern and energy dissipation rate in a rotor–stator mixer. *Chemical Engineering Research and Design*, **87**(4), pp. 533-542.

VON BATCHELDER, F. and RAEUCHLE, R., 1957. Lattice constants and Brillouin Zone overlap in dilute magnesium alloys. *Physical Review*, **105**(1), pp. 59.

WANG, A. and RACK, H.J., 1991. Transition wear behavior of SiC-particulate-and SiC-whisker-reinforced 7091 Al metal matrix composites. *Materials Science and Engineering: A*, **147**(2), pp. 211-224.

WANG, D. and OVERFELT, R.A., 2002. Oscillating cup viscosity measurements of aluminium alloys: A201, A319 and A356. *International Journal of Thermophysics*, 23(4), pp. 1063-1076.

WANG, F., QIU, D., LIU, Z., TAYLOR, J.A., EASTON, M.A. and ZHANG, M., 2013. The grain refinement mechanism of cast aluminium by zirconium. *Acta Materialia*, **61**(15), pp. 5636-5645.

WANG, J., LI, Z., FAN, G., PAN, H., CHEN, Z. and ZHANG, D., 2012. Reinforcement with graphene nanosheets in aluminum matrix composites. *Scripta Materialia*, **66**(8), pp. 594-597.

WANG, Z., CHEN, T. and LLOYD, D., 1993. Stress distribution in particulate-reinforced metal-matrix composites subjected to external load. *Metallurgical Transactions A*, **24**(1), pp. 197-207.

WESTENGEN, H. and NES, K., 1984. Twin Roll Casting of Aluminium: The Occurrence of Structure Inhomogeneities and Defects in As Cast Strip. *Essential Readings in Light Metals: Cast Shop for Aluminum Production, Volume 3*, , pp. 972-980.

WHITE, J. and WILLIS, T., 1989. The production of metal matrix composites by spray deposition. *Materials & Design*, **10**(3), pp. 121-127.

WRIGHT, S. and NOWELL, M., 2006. EBSD image quality mapping. *Micorscopy and Microanalysis*, 12, pp. 72-84.

ZHANG, J., XU, S. and LI, W., 2012. High shear mixers: A review of typical applications and studies on power draw, flow pattern, energy dissipation and transfer properties. *Chemical Engineering and Processing: Process Intensification*, **57**, pp. 25-41.

ZHANG, M. and KELLY, P., 2005. Edge-to-edge matching and its applications: Part i. application to the simple hcp/bcc system. *Acta Materialia*, **53**(4), pp. 1073-1084.

ZHANG, M.-., KELLY, P.M., EASTON, M.A. and TAYLOR, J.A., 2005. Crystallographic study of grain refinement in aluminum alloys using the edge-to-edge matching model. *Acta Materialia*, **53**(5), pp. 1427-1438.

ZHAO, H., LI, P. and HE, L., 2012. Microstructure and mechanical properties of an asymmetric twin-roll cast AZ31 magnesium alloy strip. *Journal of Materials Processing Technology*, **212**(8), pp. 1670-1675.

ZHOU, W. and XU, Z., 1997. Casting of SiC reinforced metal matrix composites. *Journal of Materials Processing Technology*, **63**(1), pp. 358-363.